System Engineering

Final Dissertation

A Bio-Inspired Air Micro-Vehicle actuated by Shape Memory Alloy Artificial Muscles

Domenico Bevilacqua

Supervisors:

Prof. Ing. Stefan Seelecke

2020 - 2024

Tag des Kolloquiums: 05.12.2025

Dekan: Prof. Dr.-Ing. Dirk Bähre

Berichterstatter: Prof. Dr.-Ing. Stefan Seelecke
Prof. Dr.-Ing. Matthias Nienhaus

Vorsitz: Prof. Dr.-Ing. Georg Frey

Akad. Mitglied: Dr.-Ing. David Böttger

de' remi facemmo ali al folle volo

Acknowledgments

First and foremost, I would like to express my deepest gratitude to my professor, Stefan Seelecke, for his valuable support and guidance as my supervisor throughout this journey.

I would also like to thank all the researchers and professors working in the iMSL (Intelligent Material Systems Lab) group in Saarbrücken, who, in various ways, have all contributed to both my technical and scientific awareness, as well as to the growth of this project itself.

In particular, I am especially grateful to Professor Gianluca Rizzello, thanks to whom I had my very first contact with the iMSL group and Professor Seelecke during my master's thesis. I would also like to thank Paul Motzki for his useful advice and insightful feedbacks throughout the development of my work. I would also like to extend my sincere thanks to Susanne-Marie Kirsch and Felix Welsch, under whose guidance I first started working on this project as a master's student and from whom I later inherited it as my PhD main project.

A special mention goes to PhD Carmen Perri for her invaluable technical and personal support throughout these years.

I also want to thank Federica, who supported me during the final phase of this journey and stands by my side as I begin a new one.

Finally, I wish to express my heartfelt gratitude to my family, to whom—just as in the past and always in the future—every one of my achievements belongs and is dedicated.

Abstract

The evolution of aerial micro-vehicles has seen a significant surge in innovation due to their potential applications in surveillance, environmental monitoring, and search-and-rescue missions. Among these advancements, bio-inspired designs have emerged as a promising pathway to develop efficient and versatile flying platforms. By mimicking the biomechanics of flapping flight observed in birds and insects, researchers aim to overcome the limitations of traditional fixed-wing and rotary-wing drones. This thesis presents the development of a bio-inspired air micro-vehicle powered by Shape Memory Alloy (SMA) artificial muscles, offering a unique combination of lightweight design, mechanical simplicity, and efficient flight dynamics.

The core innovation of this research lies in the integration of SMA actuators, which possess exceptional properties such as a high power-to-weight ratio, silent operation, and the ability to generate substantial forces within a compact form factor. Unlike traditional actuation mechanisms that rely on motors and gearboxes, SMAs provide a more bio-inspired and mechanically efficient approach to wing flapping. This novel actuation strategy not only simplifies the mechanical structure of the micro-vehicle but also reduces its overall weight, a critical factor for aerial applications.

The design process involved a comprehensive exploration of both biological inspiration and engineering optimization. Drawing from the natural mechanics of flapping wings, the system incorporates resonant compliant joints that amplify the efficiency of the wing motion by operating near the system's natural frequency. This resonance-driven approach minimizes energy consumption while maximizing the wing's angular displacement, which is crucial for generating sufficient aerodynamic lift and thrust.

Advanced manufacturing techniques were employed to bring the conceptual design to life. SMA bundles were meticulously fabricated using a resistive welding process to ensure their mechanical robustness and electrical connectivity. The rigid frame and aerodynamic components of the micro-vehicle were constructed using lightweight materials such as high-temperature resin and carbon fiber, balancing structural integrity with minimal mass. Additionally, the wing membrane was designed for flexibility and aerodynamic efficiency, inspired by existing hobbyist practices and tailored to meet the unique requirements of the prototype.

The functionality of the bio-inspired micro-vehicle was extensively validated through a series of experimental setups. High-speed camera systems were used to analyze the kinematics of the flapping wings, capturing their angular motion and identifying key performance metrics. A wind tunnel experiment was designed to measure the lift and thrust forces generated by the wings under various operational conditions. These tests provided critical insights into the relationship between actuation parameters—such as frequency and input power—and the resulting aerodynamic performance.

Furthermore, the micro-vehicle incorporates an embedded control system powered by an ESP32 microcontroller. This system was programmed to generate precise timing signals for SMA actuation, enabling both autonomous and manual operation. Bluetooth connectivity allows for remote control and real-time adjustments, providing flexibility for a variety of experimental and practical scenarios.

The research presented in this thesis represents a significant contribution to the field of bio-inspired robotics and aerial micro-vehicles. By leveraging the unique capabilities of SMAs and adopting a holistic design and validation approach, this work demonstrates the feasibility of lightweight, efficient, and mechanically simple flapping-wing micro-vehicles. The outcomes of this study not only validate the potential of SMA-driven systems but also lay the groundwork for future advancements in bio-inspired flight technologies, with applications extending to fields that demand agile and efficient aerial platforms in constrained environments.

Abstract - German Version

Die Entwicklung von Luft-Mikrofahrzeugen hat in den letzten Jahren aufgrund ihrer potenziellen Anwendungen in der Überwachung, der Umweltbeobachtung sowie bei Such- und Rettungseinsätzen einen erheblichen Innovationsschub erfahren. Unter diesen Fortschritten haben sich bio-inspirierte Designs als vielversprechender Ansatz zur Entwicklung effizienter und vielseitiger Flugplattformen etabliert. Durch die Nachahmung der Biomechanik des Schlagflugs, wie er bei Vögeln und Insekten beobachtet wird, zielen Forschende darauf ab, die Einschränkungen herkömmlicher Starrflügel- und Drehflügeldrohnen zu überwinden. Diese Arbeit präsentiert die Entwicklung eines bio-inspirierten Luft-Mikrofahrzeugs, das durch künstliche Muskeln aus Formgedächtnislegierungen (Shape Memory Alloys, SMA) angetrieben wird und eine einzigartige Kombination aus geringem Gewicht, mechanischer Einfachheit und effizienter Flugdynamik bietet.

Die zentrale Innovation dieser Forschung liegt in der Integration von SMA-Aktuatoren, die außergewöhnliche Eigenschaften wie ein hohes Leistungs-Gewichts-Verhältnis, geräuschlosen Betrieb sowie die Fähigkeit zur Erzeugung erheblicher Kräfte in kompakter Bauform aufweisen. Im Gegensatz zu traditionellen Aktuierungsmechanismen, die auf Motoren und Getrieben basieren, ermöglichen SMAs einen stärker bio-inspirierten und mechanisch effizienteren Ansatz für den Schlagflug. Diese neuartige Aktuierungsstrategie vereinfacht nicht nur die mechanische Struktur des Mikrofahrzeugs, sondern reduziert auch dessen Gesamtgewicht – ein entscheidender Faktor für luftgestützte Anwendungen.

Der Entwurfsprozess umfasste eine umfassende Auseinandersetzung mit biologischer Inspiration und ingenieurtechnischer Optimierung. Ausgehend von den natürlichen Mechanismen schlagender Flügel integriert das System resonante, nachgiebige Gelenke, die die Effizienz der Flügelbewegung durch den Betrieb nahe der Eigenfrequenz des Systems erhöhen. Dieser resonanzgetriebene Ansatz minimiert den Energieverbrauch bei gleichzeitiger Maximierung der Winkelamplitude der Flügelbewegung, was für die Erzeugung ausreichender aerodynamischer Auftriebs- und Schubkräfte entscheidend ist.

Zur Umsetzung des konzeptionellen Entwurfs wurden fortschrittliche Fertigungstechniken eingesetzt. Die SMA-Bündel wurden mittels eines Widerstandsschweißverfahrens präzise gefertigt, um mechanische Robustheit und zuverlässige elektrische Kontaktierung sicherzustellen. Der starre Rahmen sowie die aerodynamischen Komponenten des Mikrofahrzeugs wurden aus leichten Materialien wie Hochtemperaturharz und Carbonfaser hergestellt, um strukturelle Integrität bei minimaler Masse zu gewährleisten. Darüber hinaus wurde die Flügelmembran hinsichtlich Flexibilität und aerodynamischer Effizienz ausgelegt, inspiriert von bestehenden Praktiken im

Hobbybereich und angepasst an die spezifischen Anforderungen des Prototyps.
Die Funktionalität des bio-inspirierten Mikrofahrzeugs wurde umfassend durch eine Reihe experimenteller Versuchsaufbauten validiert. Hochgeschwindigkeitskamerasysteme dienten zur Analyse der Kinematik der schlagenden Flügel, wobei deren Winkelbewegung erfasst und wesentliche Leistungskennzahlen bestimmt wurden. Zusätzlich wurde ein Windkanalversuch konzipiert, um die von den Flügeln unter verschiedenen Betriebsbedingungen erzeugten Auftriebs- und Schubkräfte zu messen. Diese Untersuchungen lieferten entscheidende Erkenntnisse über den Zusammenhang zwischen Aktuierungsparametern – wie Frequenz und Eingangsleistung – und der resultierenden aerodynamischen Leistung.
Des Weiteren ist das Mikrofahrzeug mit einem eingebetteten Steuerungssystem ausgestattet, das auf einem ESP32-Mikrocontroller basiert. Dieses System wurde so programmiert, dass es präzise Taktsignale für die SMA-Aktuierung erzeugt und sowohl autonomen als auch manuellen Betrieb ermöglicht. Die Bluetooth-Konnektivität erlaubt eine Fernsteuerung sowie Echtzeitanpassungen und bietet damit hohe Flexibilität für unterschiedliche experimentelle und praktische Einsatzszenarien.

Die in dieser Arbeit vorgestellte Forschung stellt einen bedeutenden Beitrag zum Bereich der bio-inspirierten Robotik und der Luft-Mikrofahrzeuge dar. Durch die Nutzung der einzigartigen Eigenschaften von SMAs und einen ganzheitlichen Ansatz in Entwurf und Validierung wird die Machbarkeit leichter, effizienter und mechanisch einfacher Schlagflügel-Mikrofahrzeuge demonstriert. Die Ergebnisse dieser Studie bestätigen nicht nur das Potenzial SMA-getriebener Systeme, sondern schaffen auch die Grundlage für zukünftige Weiterentwicklungen bio-inspirierter Flugtechnologien mit Anwendungen in Bereichen, die agile und effiziente Luftplattformen in beengten Umgebungen erfordern.

Contents

Introduction

Micro Aerial Vehicles (MAVs) have emerged as a transformative technology, with applications spanning surveillance, environmental monitoring, and disaster response. The need for compact, efficient, and versatile flying platforms has driven extensive research into MAV design and operation. Conventional MAV designs primarily fall into two categories: fixed-wing and rotary-wing systems. Each of these configurations presents unique advantages and limitations. Fixed-wing MAVs excel in long-range missions, providing excellent energy efficiency and stability. However, their requirement for continuous forward motion limits their maneuverability, particularly in confined or cluttered environments. Conversely, rotary-wing MAVs, such as quadcopters, exhibit exceptional vertical takeoff and landing (VTOL) capabilities and superior maneuverability. Yet, their energy efficiency and flight endurance are often compromised, especially at micro-scales where motor and battery performance are constrained. While these conventional designs have achieved significant technological maturity, they remain insufficient for certain applications that demand agility, adaptability, and high efficiency in complex flight scenarios. To overcome these challenges, researchers have increasingly turned to bio-inspired designs that mimic the flapping-wing mechanisms observed in birds and insects. Flapping-wing MAVs aim to replicate the inherent efficiency and versatility of natural flyers, including hovering capabilities, agile maneuverability, and effective energy utilization during flapping. effective [17, 20, 24]

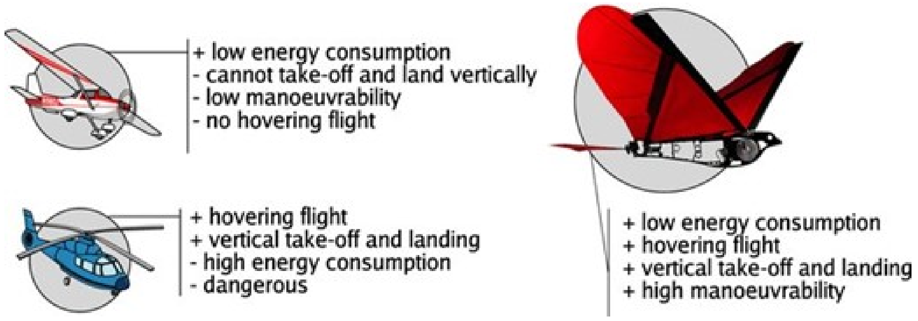

Figure 1: Air vehicles classification based on wing type and consequent flight features

State of the Art

Bio-Inspired Flapping Drones

The field of bio-inspired robotics has made significant strides in replicating the remarkable flight capabilities observed in nature. Among these, the study of flapping-wing drones, or "ornithopters", has emerged as a promising avenue for creating aerial systems with high efficiency, agility, and adaptability. These drones aim to bridge the gap between conventional fixed-wing and rotary-wing aerial vehicles by harnessing principles of natural flight seen in birds, bats, and insects. The versatility and maneuverability achieved by these natural flyers serve as the ultimate benchmark for bio-inspired aerial systems. One of the most compelling advantages of flapping-wing drones lies in their potential to operate in complex environments where traditional aerial systems may struggle. Fixed-wing drones require forward velocity to maintain lift, limiting their utility in confined or obstacle-rich spaces. Rotary-wing systems, such as quadcopters, offer better maneuverability but often lack energy efficiency, particularly in sustained flight. Flapping-wing drones, on the other hand, promise a unique combination of efficient lift generation, hover capability, and the ability to navigate complex environments with greater adaptability. Moreover, the dynamic, flapping motion of their wings enables smoother interactions with gusts and turbulence, reducing the mechanical stress experienced by the vehicle[18, 13].

Despite these advantages, the development of bio-inspired flapping drones presents significant engineering challenges. Key design considerations include weight minimization, energy efficiency, and the ability to replicate complex wing motions within the constraints of available actuation technologies. Over the years, several innovative examples of bio-inspired flapping drones have been developed, showcasing different approaches to addressing these challenges. This subsection focuses on three state-of-the-art examples: the DelFly, the Bionic Flying Fox, and the BatBot, each representing a unique perspective on how to achieve bio-inspired flapping flight.

The **DelFly** [5, 4] (Figure 2), developed at Delft University of Technology, is one of the most successful examples of insect-inspired flapping drones. The latest iteration, the DelFly Nimble, measures 33 cm in wingspan and weighs just 29 grams, including its onboard battery and camera system. It is capable of flying for approximately

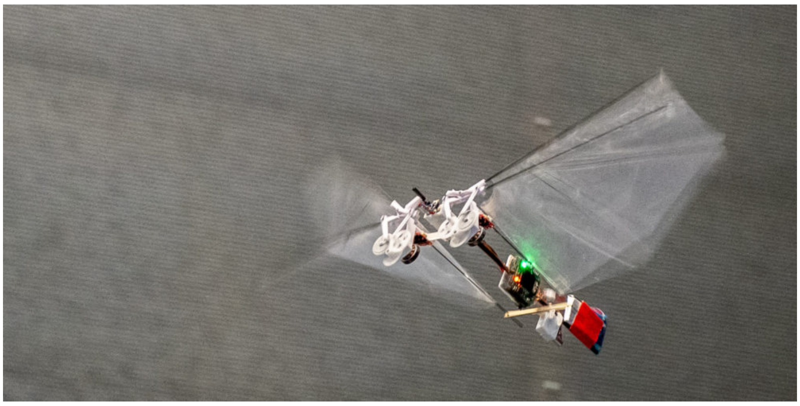

Figure 2: The DelFly Nimble, developed at Delft University of Technology.

5 minutes on a single charge while performing highly agile maneuvers such as hovering, forward flight, flips, and sharp turns. The DelFly achieves these capabilities using a pair of flapping wings powered by servo motors that generate both lift and thrust without the need for additional control surfaces. The lightweight structure of the DelFly is key to its performance, allowing it to mimic the agility of insects. However, the use of servo motors and gears imposes mechanical complexity and adds weight, which could limit scalability and energy efficiency. These limitations highlight the potential for using Shape Memory Alloy (SMA) actuators, which could replace bulky mechanical components with lightweight and compact actuation systems, potentially extending flight endurance and simplifying the mechanical design. In contrast to the DelFly's insect-inspired design, the **Bionic Flying Fox** [1], developed by Festo, takes inspiration from much larger natural flyers, specifically fruit bats. With a wingspan of 2.28 meters (Figure 3) and a weight of 580 grams, the Bionic Flying Fox is a large-scale bio-inspired system designed for efficient flapping and gliding flight. Its wings are constructed with a lightweight frame covered by an elastic membrane, allowing for flexible and adaptive flight dynamics. The drone is capable of semi-autonomous operation, with onboard sensors and software to coordinate its flight path. However, its reliance on motorized mechanisms to actuate the flapping motion limits its energy efficiency and increases mechanical complexity. The size and weight of the actuation system also restrict its scalability to smaller platforms. The use of SMA actuators in place of traditional motors and gears could address these limitations by providing a lightweight and compact solution, enabling the development of similarly efficient systems on a smaller scale.

Figure 3: The Bionic Flying Fox, developed by Festo.

The **BatBot** [19], developed at Caltech, represents a unique approach to bio-inspired flight, replicating the complex wing dynamics of bats. The BatBot (Figure 4) has a wingspan of 34 cm and weighs only 93 grams, including its onboard electronics. Its wings are composed of a lightweight frame covered with a stretchable silicone membrane that mimics the elasticity of real bat wings. Unlike simpler flapping drones, the BatBot incorporates multiple degrees of freedom, enabling independent control of different sections of the wing. This allows the BatBot to replicate the highly articulated wing movements observed in bats, including adaptive pitch and spanwise twisting. The BatBot demonstrates exceptional maneuverability and efficiency, with the ability to perform complex aerial maneuvers and adapt to varying aerodynamic conditions.

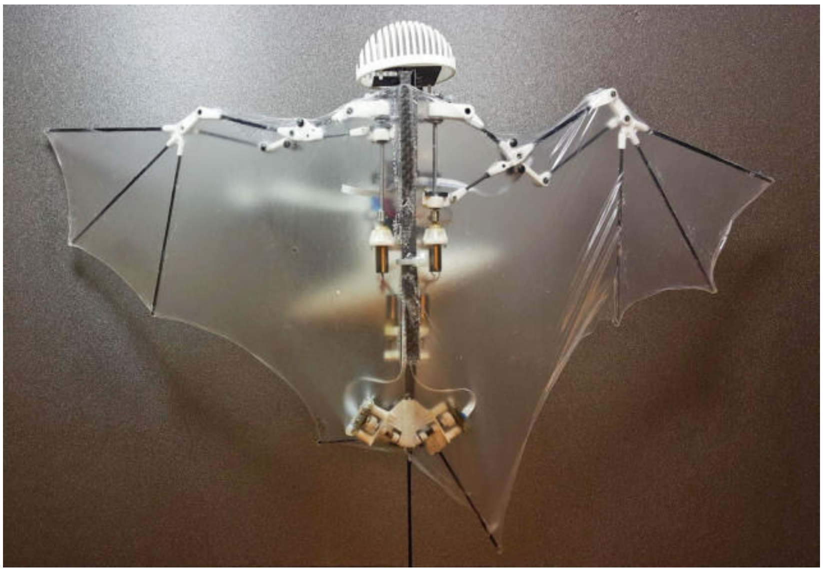

Figure 4: The BatBot, developed at Caltech.

These examples illustrate the progress made in the field of bio-inspired flapping drones, each showcasing innovative approaches to replicating natural flight. While the DelFly demonstrates the potential of small-scale, insect-inspired systems, the Bionic Flying Fox highlights the feasibility of large-scale bio-mimetic designs, and the BatBot pushes the boundaries of flexibility and articulation in wing dynamics. However, the use of servo motors to control the multiple joints increases weight and mechanical complexity, which SMA actuators could mitigate. SMAs could replace the servos in key areas, such as the wing joints, reducing weight and simplifying the design while maintaining the flexibility required for bat-like flight. The integration of SMA actuators offers a promising avenue to address these challenges, paving the way for the next generation of lightweight, efficient, and scalable bio-inspired drones.

SMA Micro-wires as Artificial Muscle

Shape Memory Alloys have emerged as a promising technology in the field of bio-inspired robotics due to their unique ability to undergo a reversible phase transformation when subjected to thermal stimuli. This property enables SMAs to function as compact and lightweight actuators, mimicking the contractile behavior of natural muscles. Among the different forms of SMA actuators, micro-wires have garnered significant interest because of their high power-to-weight ratio, scalability, and ease of integration into small-scale systems. These attributes make SMA micro-wires an ideal candidate for applications in the bio-inspired robotics field, where soft and bendable actuators and joints are design goals[6, 30].

One notable example is the work of Filomena Simone, who developed a **Bionic Hand** [27] (Figure 5) actuated entirely by SMA wires. This system demonstrated the potential of SMA micro-wires to replicate complex and precise movements in a compact form factor. By carefully designing the arrangement of SMA wires and optimizing the control strategy, the bionic hand was capable of performing intricate tasks with a high degree of accuracy. This study highlighted the feasibility of using SMA wires as artificial muscles for applications requiring biomimetic movement, while also addressing challenges such as thermal management and response time.

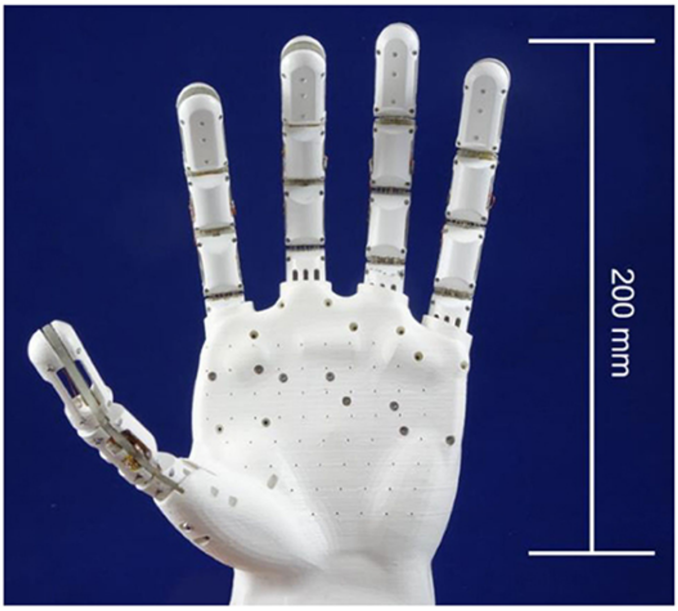

Figure 5: A bionic hand actuated by SMA wires, developed by Filomena Simone.

The **SMA Continuum Robot** [9](Figure 6), developed by Yannik Goergen and collaborators, represents a significant advancement in the application of SMA wires for soft robotics. This system utilizes SMA wires arranged in a continuum configuration to achieve flexible and adaptive movement. The SMA Continuum Robot mimics the behavior of biological structures, such as the arms of cephalopods or the tongues of vertebrates, allowing for smooth and continuous deformations. By employing an array of SMA wires in an antagonistic configuration, the robot achieves precise control over its bending and elongation motions. This antagonistic approach helps mitigate some of the inherent limitations of SMA actuation, such as slow cooling times, by ensuring continuous operation through opposing wire pairs. The research also demonstrates innovative thermal management strategies, such as active cooling mechanisms, to increase the actuation frequency of the SMA wires. These advancements position the SMA Continuum Robot as a benchmark for exploring the potential of SMA actuators in complex, multi-degree-of-freedom systems.
Another significant application of SMA wires can be seen in the **BaTboT**, developed by Julian David Colorado Montaño. This system incorporated SMA micro-wires to actuate the elbow joints of the bat-inspired wings, enabling smooth and natural wing movements. The BaTboT represents a pioneering effort to explore SMA-based actuation in flapping systems, demonstrating the ability of SMA wires to replicate bio-mimetic motion. However, the actuation frequency of the SMA wires was limited to below 2 Hz, primarily due to the thermal hysteresis of the material. This constraint highlights a key challenge associated with SMA wires: their reliance on

Figure 6: The SMA Continuum Robot, showcasing bio-inspired motion using SMA wires.

thermal cycling for actuation, which restricts their dynamic performance in high-speed applications. Despite these limitations, the BaTboT showcases the potential of SMA wires for lightweight and compact designs in bio-inspired robotics. Figure 7 shows the BaTboT, emphasizing its use of SMA wires for joint actuation.

A particularly influential project in the development of SMA-actuated flapping drones is the **BATMAV**, conceived by Bunget and Seelecke in 2009. The BATMAV (Bat-inspired Micro Aerial Vehicle) was one of the first attempts to integrate SMA wires as artificial muscles in a bio-inspired flapping-wing drone. The system used SMA wires to drive the wing flapping motion, directly mimicking the muscle-driven flight of bats. Despite its innovative design, the BATMAV faced significant technological limitations. At the time, the manufacturing techniques available for

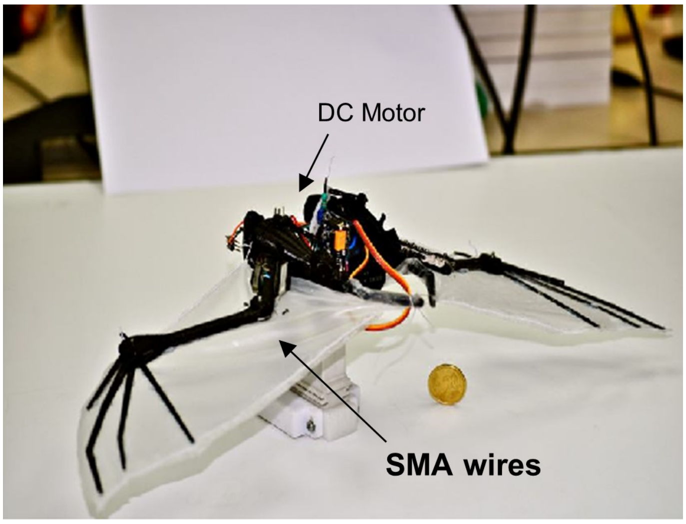

Figure 7: The BaTboT, a bat-inspired robot developed by Julian Colorado.

lightweight structures were relatively rudimentary, and the embedded control systems were bulky and inefficient. These constraints limited the system's scalability and actuation frequency, preventing the BATMAV from achieving its full potential. Furthermore, the BATMAV lacked an agonist-antagonist configuration, meaning the SMA wires worked unidirectionally, relying on passive forces (e.g., elastic structures) to return the wings to their starting position. This limited the precision and frequency of wing actuation.
In recent years, Professor Seelecke revisited the BATMAV project, leveraging advancements in manufacturing and embedded systems to overcome the challenges faced in the original design. Modern 3D printing technologies now enable the rapid prototyping of lightweight, complex structures with higher precision, while the development of ultra-lightweight microcontrollers, such as the ESP32 XIAO used in the final prototype of this research, provides efficient and compact control solutions. These advancements allow SMA wires to be utilized more effectively in flapping-wing drones, achieving higher actuation frequencies and greater energy efficiency. Figure 8 illustrates the original BATMAV prototype.

Despite its early limitations, the BATMAV laid the foundation for this research, serving as a critical reference point for the development of SMA-actuated flapping drones. This thesis builds upon the legacy of the BATMAV by introducing an agonist-antagonist configuration for SMA wires, a novel approach that improves actuation precision, increases operating frequency, and reduces thermal hysteresis. By combining these innovations with modern prototyping and embedded control technologies, this research aims to achieve a lightweight and efficient flapping drone capable of operating at frequencies comparable to natural flyers.

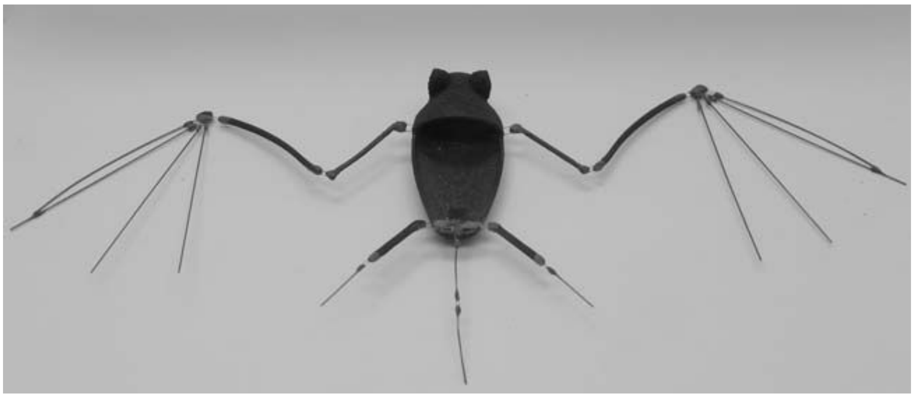

Figure 8: The BATMAV prototype, developed by Bunget and Seelecke.

Motivation and Goals

The motivation behind this work stems from the potential of Shape Memory Alloy (SMA) micro-wires to revolutionize the design of flapping-wing drones. Unlike traditional actuators such as servos and motors, SMA wires offer a unique combination of advantages that make them particularly suitable for bio-inspired applications. Their high power-to-weight ratio enables the creation of lightweight systems capable of generating significant forces relative to their mass. This is critical for aerial systems where every gram of added weight directly impacts flight performance. Additionally, SMA wires operate silently and require minimal mechanical components, simplifying the overall design and reducing the risk of mechanical failure. These attributes make SMA-based actuation a compelling solution for compact and efficient flapping-wing drones.

The primary goal of this research is to design, develop, and test a bio-inspired flapping-wing drone that leverages SMA micro-wires as its sole actuation mechanism. The drone must be capable of generating sufficient aerodynamic forces, including lift and thrust, to achieve self-propulsion. In this context, "self-propulsion" refers to forward motion induced exclusively by the flapping of its wings, without the assistance of auxiliary propulsion systems. Furthermore, the system must be a fully embedded platform, incorporating all essential components such as onboard electronics, a battery, and a control logic unit, making it a standalone and functional prototype. This research also aims to overcome the limitations of SMA-based actuation, such as low actuation frequency and thermal hysteresis, through innovative design strategies such as agonist-antagonist configurations and resonance-based mechanisms.

To summarize, the objectives of this work are as follows:

- Develop a flapping-wing drone actuated exclusively by SMA micro-wires.
- Design a lightweight and efficient structure capable of sustaining aerodynamic forces sufficient for forward motion.
- Create a fully embedded system, including electronics, a power source, and control logic, ensuring autonomous operation.
- Explore innovative solutions to address the limitations of SMA wires, such as limited actuation frequency and thermal hysteresis, to achieve operational frequencies comparable to natural flyers.

Thesis Outline

The content of this thesis is organized as follows:

- **Chapter 1: Ornithopter Theory**
  This chapter provides a theoretical foundation for understanding the principles of flapping-wing flight. It introduces key concepts such as lift, thrust, and resonance, along with their application to bio-inspired aerial systems. A review of existing ornithopter designs is also included to contextualize this research.
- **Chapter 2: Shape Memory Alloys**
  This chapter delves into the properties of SMA materials, focusing on their thermomechanical behavior and suitability for actuation. The unique advantages of SMA micro-wires, such as their high power-to-weight ratio, are discussed alongside their limitations, including thermal hysteresis and response time.

- **Chapter 3: SMA-Driven Flapping Wing Mechanism**
  This chapter details the design and implementation of the SMA-actuated flapping mechanism. It covers the structural design, selection of SMA wires, and the introduction of the agonist-antagonist configuration to enhance actuation precision and frequency.

- **Chapter 4: Embedded Prototype Development**
  This chapter describes the integration of the SMA flapping mechanism into a fully embedded system. Topics include the selection and programming of lightweight microcontrollers, the design of the electronic control circuit, and the integration of the power source. Emphasis is placed on achieving a compact and lightweight design.

- **Chapter 5: Experimental Results**
  This chapter presents the results of experiments conducted to evaluate the aerodynamic performance of the prototype. Key metrics such as lift, thrust, and forward velocity are analyzed under different operating conditions. The results are compared with theoretical predictions to validate the design.

- **Chapter 6: Conclusions and Future Work**
  The final chapter summarizes the main findings of the research, highlighting the achievements and limitations of the prototype. It also outlines potential directions for future work, including further optimization of the SMA mechanism and exploration of new applications for bio-inspired aerial systems.

Chapter 1

Ornithopter Theory

Flapping-wing devices, known as *ornithopters*, represent one of the most fascinating approaches to achieving flight by mimicking the natural mechanisms of birds, bats, and insects. Unlike traditional fixed-wing or rotary systems, ornithopters generate both lift and thrust through oscillatory wing movements, leading to unique aerodynamic and mechanical characteristics.

Ornithopters are designed to harness the advantages of flapping wings, offering several benefits compared to conventional aircraft. Unlike propellers, flapping wings can minimize aerodynamic drag during the upstroke while maximizing lift during the downstroke. This dynamic adjustment allows for improved efficiency and maneuverability, making flapping-wing designs particularly suited for applications requiring high agility and precision. Additionally, the aerodynamic mechanisms exploited by flapping wings, such as delayed stall and the clap-and-fling effect, enable greater lift generation even at small scales.

Another key advantage of flapping-wing devices is their reduced noise output. Unlike rotary airfoils, which produce significant aerodynamic noise, flapping wings operate in a quieter and more energy-efficient manner, a feature highly desirable for stealth operations such as wildlife monitoring or reconnaissance. From a bio-inspired perspective, ornithopters replicate nature's solutions to flight, drawing inspiration from the incredible efficiency and adaptability of birds, bats, and insects.

1.1 Principles of Flapping Wing Flight

The theory of flapping-wing flight combines elements of aerodynamics, biomechanics, and structural dynamics. Unlike fixed-wing flight, where steady-state aerodynamics govern lift production, ornithopter wings operate cyclically through upstroke and downstroke phases. During the downstroke, the wing generates both lift and thrust, while the upstroke is optimized to reduce drag by feathering or retracting the wing. This cycle ensures a continuous force output for forward flight.

The aerodynamic efficiency of flapping wings is enhanced by mechanisms like delayed stall, which allows the wing to maintain lift production at higher angles of attack without flow separation. Additionally, the clap-and-fling mechanism, observed in insects, further boosts thrust generation by creating high-pressure regions when the wings clap together and fling apart. These unsteady aerodynamic effects distinguish flapping-wing flight from conventional systems and allow for greater maneuverability. Flexible wing structures play a critical role in improving flight performance. Unlike rigid wings, flexible wings can passively adjust their shape under aerodynamic loads, reducing energy losses and enhancing lift-to-thrust conversion. This adaptability mirrors the behavior of biological wings, which deform naturally to optimize flight efficiency.[2].

1.2 Design and Construction

The design of an ornithopter involves balancing weight, strength, and aerodynamic efficiency. Successful ornithopter construction relies on selecting appropriate materials and designing mechanisms that ensure smooth and efficient wing flapping motion[12].

For structural components, lightweight and durable materials are essential to minimize the overall weight of the device. Carbon fiber is frequently used for wing spars and body structures due to its exceptional strength-to-weight ratio, while thin polymer films, such as polyethylene, are ideal for wing membranes. These materials combine flexibility and durability, enabling the wings to withstand cyclic aerodynamic loads without failure[14].

The mechanical design of the wings is equally crucial. Wings can be configured as monoplanes, biplanes, or tandem systems depending on the desired performance characteristics. Monoplane wings, which mimic bird-like flight, offer simplicity and efficiency for forward flight. Biplane configurations, inspired by insect wings, allow for slower and more controlled flapping motion, making them suitable for hovering. Tandem wings, often modeled after dragonflies, provide improved stability and thrust.

Incorporating compliant joints into the wing structure further enhances the bio-inspired nature of the design. Compliant joints, which replace traditional rotary hinges, reduce energy losses due to friction and improve mechanical resonance. This approach not only simplifies the mechanical design but also allows the wings to operate more efficiently at their natural frequency.

Traditional ornithopters rely on motors, gears, and linkages to convert rotary motion into wing flapping. These systems, while functional, add significant weight and complexity to the design. In contrast, modern advancements have introduced artificial muscles, such as Shape Memory Alloy (SMA) actuators, as lightweight and compact alternatives. SMA wires contract when heated through Joule heating, producing mechanical motion without the need for bulky mechanical components.

The use of SMA actuators would be able to eliminate the need for mechanical gearboxes, simplifying the overall design. By directly inducing contraction and extension in the wing-driving system, SMA-driven ornithopters achieve smooth and efficient flapping motion. Thermal activation of SMA wires, coupled with careful cooling strategies, allows for higher actuation frequencies, improving the performance of the flapping mechanism. Compact lithium-polymer (LiPo) batteries typically provide the necessary energy density for power supply. Step-up voltage converters ensure that the actuators receive the required activation voltage while minimizing the system's weight. This combination of lightweight power sources and SMA actuators

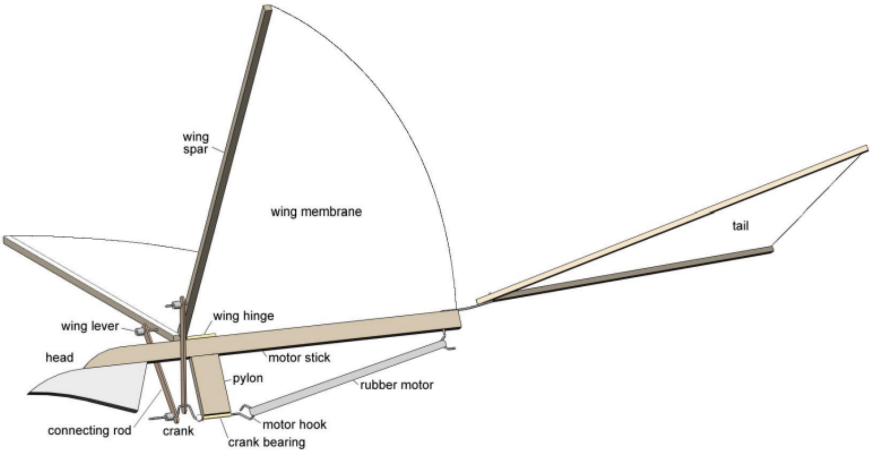

Figure 1.1: Classic design structure of an ornithopter powered by rubber-band

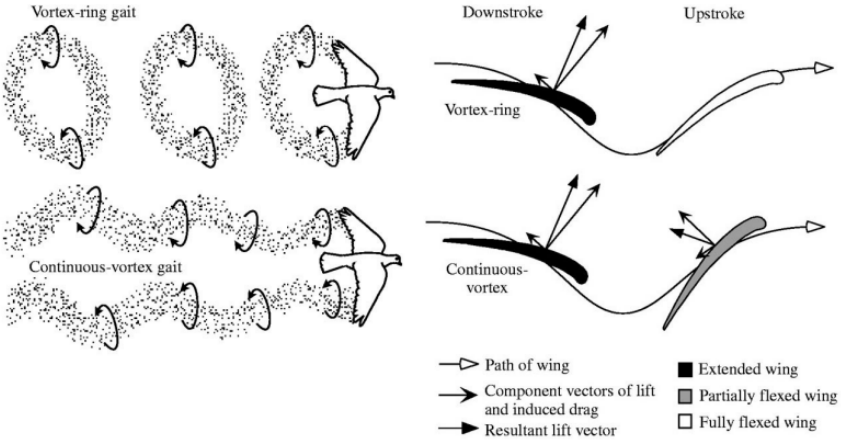

Figure 1.2: Graphic representation of main components of flapping-wing aerodynamics

enables the development of highly efficient, bio-inspired ornithopters.

1.3 Aerodynamics

The aerodynamic behavior of flapping wings is governed by unsteady flow phenomena that arise during cyclic wing motion. Unlike fixed wings, which operate under steady aerodynamic conditions, flapping wings generate lift and thrust through dynamic effects such as delayed stall, wake capture, and vortex shedding [25, 7, 11].
During the downstroke, the wing generates a large amount of lift and thrust by exploiting high angles of attack and delaying flow separation. The upstroke, on the other hand, minimizes drag through wing feathering or retraction. This asymmetry between the upstroke and downstroke phases allows for continuous forward thrust generation.
Unsteady aerodynamic effects, such as the clap-and-fling mechanism, enhance thrust

production by creating high-pressure regions as the wings close together and fling apart. Additionally, flexible wing structures improve aerodynamic efficiency by adjusting their shape under varying load conditions. This passive deformation reduces energy losses and optimizes lift-to-thrust conversion, mirroring the behavior of biological wings.

1.4 Applications of Ornithopters

Ornithopters have a wide range of applications across research, industry, and education. Their bio-inspired design and unique flight capabilities make them ideal for tasks where traditional aircraft are less effective[8]. For example, ornithopters are widely used in wildlife monitoring and environmental surveillance due to their quiet operation and natural appearance, which minimizes disturbance to animals.

In the field of robotics and aerodynamics, ornithopters serve as platforms for studying bio-inspired flight mechanisms, providing valuable insights into the aerodynamics of birds and insects. Their lightweight design and maneuverability also make them suitable for reconnaissance missions and unmanned aerial vehicle (UAV) applications, where stealth and agility are critical.

Furthermore, ornithopters are commonly used as educational tools to teach concepts of aerodynamics, mechanics, and robotics. Simple designs constructed from lightweight materials provide students and hobbyists with hands-on experience in building and testing flapping-wing devices.

Ornithopters represent a remarkable convergence of biology and engineering, leveraging flapping-wing dynamics to achieve efficient and maneuverable flight. Advances in materials, actuators, and aerodynamic understanding have paved the way for innovative ornithopter designs capable of overcoming the limitations of traditional aircraft. By incorporating bio-inspired features such as compliant joints and SMA actuators, modern ornithopters offer a lightweight and efficient solution for a wide range of applications, marking a significant step toward replicating the flight performance of natural organisms[10, 28].

Chapter 2

Shape Memory Alloys

Shape Memory Alloys (SMAs) are a class of smart materials that can "remember" their original shape after being deformed, provided they are heated beyond a certain threshold temperature. This is made possible through a phase transition between two crystal structures: martensite and austenite. When heated, SMAs recover their shape before deformation, a property known as the Shape Memory Effect. In addition, SMAs also exhibit pseudoelasticity, where they can undergo large recoverable strains under stress at higher temperatures without permanent deformation. These properties make SMAs ideal for various applications, from actuators in robotics to medical devices. One of the most significant advantages of SMAs is their ability to generate high forces relative to their volume, as well as their simple and lightweight nature. Given these properties, SMAs are particularly attractive for use in bio-inspired systems that mimic the functionality of biological muscles, especially when we consider applications where weight is critical like in drones.
This chapter explores the fundamental concepts underlying the operation of SMAs, detailing their internal structure, phase transformations, and actuation principles.

2.1 Material Structure

The thermomechanical properties of Shape Memory Alloys arise from their unique microstructure and the phase transformation they undergo between martensite and austenite. The understanding of the crystallographic nature of SMAs is useful for designing systems that exploit these properties effectively. SMAs are typically composed of metal alloys, with the most common being the nickel-titanium alloy (NiTi), although other materials such as copper-aluminum-nickel (Cu-Al-Ni) and iron-based alloys can also be used [3, 29]. The distinctive characteristic of SMAs lies in their ability to change their crystal structure when subjected to changes in temperature or stress, enabling the material to "remember" a specific shape.

Austenite Phase

The austenite phase is the high-temperature phase of SMAs, typically stable at temperatures above the *Austenite Finish Temperature (Af)*. In this phase, the crystal structure is typically cubic, most often in the *face-centered cubic (FCC)* configuration, although some SMAs adopt other structures, such as the *body-centered cubic (BCC)* structure. Austenite is relatively rigid and does not exhibit the large elastic strains that are characteristic of martensite. As such, it can support higher stresses without undergoing significant deformation.

$$\text{Austenite} \quad \xrightarrow{T>Af} \quad \text{Rigid, stable phase}$$

Martensite Phase

The martensite phase is the low-temperature phase, stable below the *Martensite Start Temperature (Ms)*. Martensite adopts a *monoclinic* or *orthorhombic* crystal structure, depending on the alloy. This phase is significantly more deformable than austenite and can undergo large strains (up to 8% or more) when subjected to stress, which can be recovered when the temperature is raised, resulting in the return to the austenite phase.

$$\text{Martensite} \quad \xrightarrow{T<Ms} \quad \text{Soft, deformable phase}$$

Transformation Mechanism

The transformation between martensite and austenite occurs at specific temperatures, characterized by the *Martensite Start Temperature (Ms)*, *Martensite Finish Temperature (Mf)*, *Austenite Start Temperature (As)*, and *Austenite Finish Temperature (Af)*. These temperatures define the boundaries of the phase transition and determine the temperature range over which the phase change can occur.

The transformation is also governed by the stress applied to the material. At temperatures above Af, the SMA remains in the austenitic phase. Upon cooling below Ms, the material undergoes a transformation to the martensitic phase. The reverse transformation occurs when the material is heated above Af, leading to the recovery of the original shape.

$$T > Af \quad \text{Austenite phase (rigid)}$$
$$Ms < T < Af \quad \text{Mixed phase (austenite + martensite)}$$
$$T < Ms \quad \text{Martensite phase (deformable)}$$

Thermal Hysteresis

During the phase transition between martensite and austenite, SMAs exhibit thermal hysteresis, meaning the temperatures at which the material transforms when heating differ from those during cooling. This results in a lag between the heating and cooling cycles, which must be accounted for in the design of SMA actuators[16]. The latent heat associated with the phase transition can be expressed as:

$$Q_{\text{lat}} = m \cdot \Delta H$$

where: - m is the mass of the SMA, - ΔH is the latent heat per unit mass associated with the phase transition.

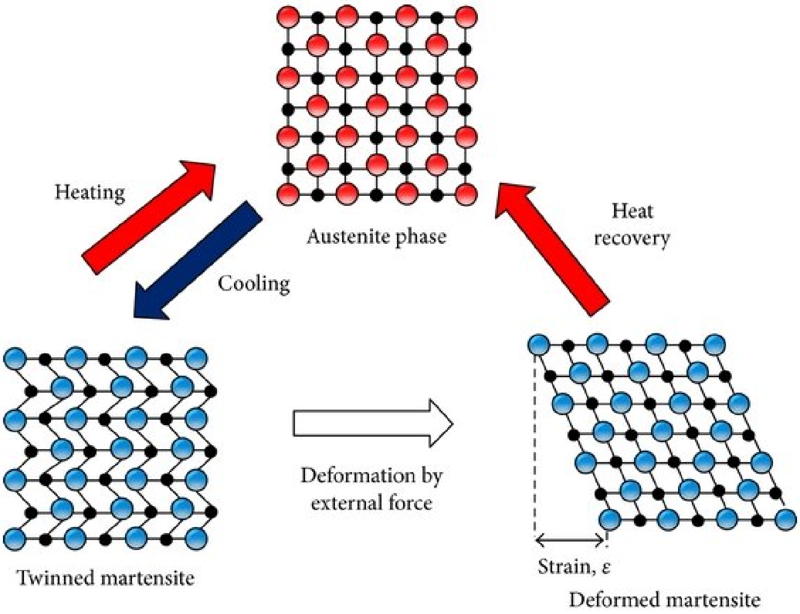

Figure 2.1: The SMA internal phase change cycle depending on temperature

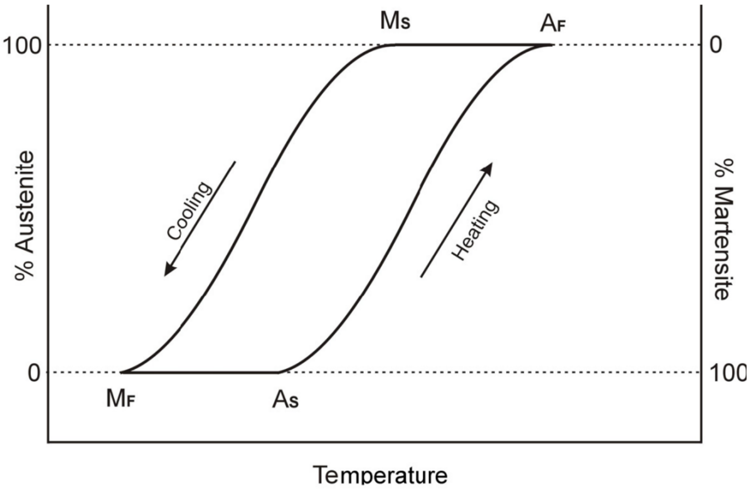

Figure 2.2: Hysteresis characteristic of SMAs

2.2 SMA Actuation

Shape Memory Alloys (SMAs) exhibit unique actuation properties, primarily driven by their phase transformation between martensite and austenite. The actuation of SMAs relies on the material's ability to undergo large, reversible strains in response to temperature changes. This section explores the fundamental principles of SMA actuation, including the mechanical forces involved and different actuation systems.

2.2.1 Principles of SMA Actuation

The core principle of SMA actuation is the phase transition between martensite and austenite. When an SMA is heated, the material undergoes a transformation from the low-temperature, flexible martensitic phase to the high-temperature, rigid austenitic phase. This transformation generates a mechanical force and results in a change in shape, which is used to perform work.

Shape Memory Effect

At ambient temperature (approximately 290 K), in the absence of any external load, the material's crystal structure adopts a twinned martensitic configuration. When external stress is applied, the martensitic variants are compelled to align uniformly, resulting in a detwinned martensite configuration. Upon removal of the applied stress, the material retains this configuration and does not revert to its initial twinned martensite form. To recover its original shape, the material must be heated to a temperature above the A_f (austenite finish) temperature, allowing the phase transformation to proceed completely. In the austenitic phase, the variants exhibit a distinct lattice structure, but the macro-scale shape of the material remains the same as that of the twinned martensite configuration. This phenomenon is referred to as the one-way shape memory effect (OWSME), as the material "remembers" only one shape—the austenitic phase. After undergoing mechanical deformation, the material must undergo a temperature-induced phase transformation to revert to its pre-deformed (or "memorized") shape.

Two-Way Shape Memory Effect

The one-way shape memory effect refers to the material's ability to "remember" the shape associated with the austenitic phase. Unlike the OWSME, the Two-Way Shape Memory Effect (TWSME) is not an intrinsic property of the material. Rather, it emerges following specific thermomechanical treatments, commonly referred to as training procedures.

The two-way shape memory effect enables the material to "remember" both a desired martensitic shape and austenitic shape. This behavior is induced by varying the alloy's temperature, which drives a phase transformation without the need for external stress or load. At room temperature, the SMA exhibits a predefined shape, which is attained after a proper training process. As the temperature is increased above the A_s (austenite start) temperature, the material undergoes a phase transformation, beginning its shape change. The transformation completes once the temperature reaches the A_f temperature, at which point the material achieves the desired "clip shape". During the cooling phase, when the material reaches the M_s (martensite start) temperature, the variants gradually transition to a detwinned martensitic configuration. This transformation is fully realized when the material reaches the M_f (martensite finish) temperature, at which point the material returns to its initial configuration.

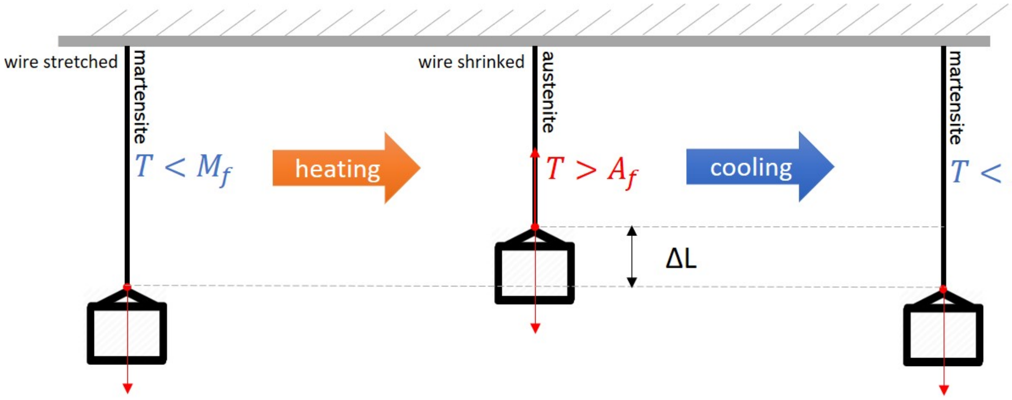

Figure 2.3: An example of the two-way shape memory effect of a SMA wire with constant load.

Pseudoelasticity

Another important characteristic of SMAs is pseudoelasticity, which occurs when the material is above its Austenite Finish Temperature A_f and undergoes a stress-induced transformation between the austenite and martensite phases. In this regime, the material exhibits large recoverable strains without permanent deformation.
Pseudoelasticity is different from traditional elasticity in that the material undergoes phase transformation rather than elastic deformation. The stress-strain behavior in this regime is nonlinear and exhibits hysteresis, with the material returning to its original state when the stress is removed. The pseudoelastic stress-strain curve typically shows two distinct regions: the loading phase, where the material transforms from austenite to martensite, and the unloading phase, where the material recovers its original shape as the martensite transforms back to austenite.
The hysteresis in the stress-strain loop is a key feature of pseudoelasticity, and it is important to account for it in actuator designs that use SMAs, as it can impact the overall efficiency of the system.

Actuation Strain and Force Generation

The actuation strain generated by an SMA is directly related to the transformation between martensite and austenite. The strain generated can be expressed as the change in length ΔL relative to the initial length L_0 of the SMA element:

$$\Delta L = \epsilon_{\text{actuation}} \cdot L_0$$

where $\epsilon_{\text{actuation}}$ is the strain induced in the SMA during the phase transformation. For SMAs, the strain can be substantial, reaching up to 8% in some alloys, particularly when the transformation involves a complete transition from martensite to austenite.
The force generated by the SMA actuator is the result of the stress induced during the phase transition. The force can be modeled as:

$$F = \sigma \cdot A$$

where: - F is the force generated, - σ is the stress generated in the SMA, - A is the cross-sectional area of the SMA element.

2.2.2 SMA-Wire Actuation Systems

The actuation of SMAs can be implemented in different mechanical configurations, often combined with additional mechanical components such as springs or other SMA elements[22, 23]. The following sections discuss two common types of actuation systems: the spring-load system and the SMA-load system.

SMA wire with Spring-Load System

One of the most commonly adopted configurations for shape memory alloy (SMA) actuators involves the use of a preloaded biasing spring. This setup provides a simple yet effective means of achieving bidirectional motion without the need for a second active SMA wire, as in the agonist-antagonist configuration. The fundamental principle of this actuation scheme relies on the interplay between the contraction of the SMA wire upon activation and the restoring force of the spring upon deactivation.
In this configuration, the SMA wire and the linear spring are arranged in an agonistic relationship, meaning that when the SMA wire is heated and undergoes phase transformation into its austenitic state, it contracts, thereby stretching the biasing spring and moving the actuation point (Figure2.4). Upon cooling, the SMA returns to its detwinned martensitic phase, during which the elastic force stored in the spring restores the system to its initial position. This cyclic contraction and extension enable repeatable motion, which can be exploited in a variety of robotic applications.
From a mechanical perspective, the system can be modeled by combining the constitutive equations of the SMA material with the dynamics of the biasing spring. The equation governing the system can be expressed as:

$$m\ddot{l} + k(l - l_k) + f = 0, \tag{2.1}$$

where:

- m represents the mass of the load,
- k is the stiffness of the biasing spring,
- l denotes the displacement of the system,

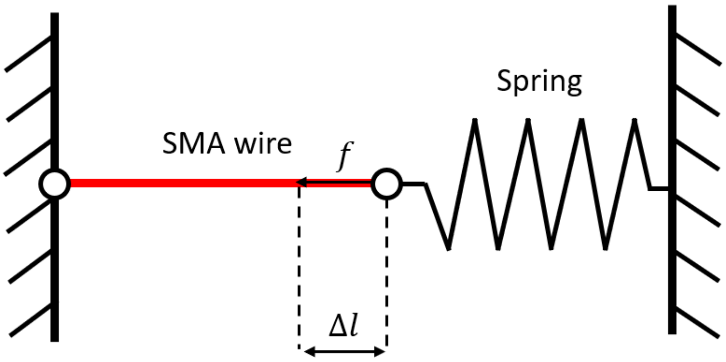

Figure 2.4: Schematic representation of a SMA wire-spring system

- l_k is the initial pre-deflection of the spring,
- f is the force generated by the SMA wire.

The dynamics of the system can be better understood by analyzing its stress-strain response during actuation. Initially, when the SMA wire is in its martensitic phase, the system is in equilibrium with the biasing spring, which is preloaded. In this condition, the equilibrium point is defined by the intersection of the SMA hysteresis curve and the linear characteristic of the spring. Since the SMA wire is in detwinned martensitic configuration, it is in a relatively elongated state.

Upon activation via Joule heating, the SMA temperature rises, leading to a shift in the stress-strain behavior. Graphically, this is represented by an upward displacement of the hysteresis curve in the stress-strain diagram. Since the spring is a purely elastic component, its characteristic remains unchanged, and the new equilibrium position is dictated by the evolving SMA properties. If the heating continues, the equilibrium point migrates along the lower branch of the SMA hysteresis curve, signifying progressive contraction of the wire.

When the SMA wire reaches a sufficiently high temperature, surpassing the austenite finish temperature A_f, it fully transforms into the austenitic phase. At this point, the system attains a new equilibrium, where the SMA wire is in its shortest possible state and the biasing spring is maximally elongated. This marks the peak displacement achievable by the system. During the cooling phase, the transformation stress in the SMA wire decreases, causing its hysteresis curve to shift downward. Consequently, the equilibrium point moves back along the upper branch of the hysteresis loop, following the progressive elongation of the SMA wire as it returns to the martensitic state.

This cyclical behavior is key to the effective operation of SMA-spring actuators. The stroke achieved by the system is determined by the difference between the equilibrium position at the onset of actuation and the final position upon full transformation, which can be expressed as:

$$\Delta l = l_{mart} - l_{aust}, \tag{2.2}$$

where l_{mart} and l_{aust} are the lengths of the SMA wire in the martensitic and austenitic phases, respectively. The choice of spring stiffness k plays a crucial role in determining the overall system performance: a higher stiffness results in faster recovery but may reduce the total achievable stroke, while a lower stiffness enables greater displacement at the cost of slower resetting time.

The SMA-spring configuration offers several advantages, including simplicity in design, reduced control complexity compared to agonist-antagonist setups, and lower energy consumption. However, it also presents certain limitations. The system is inherently limited by the cooling rate of the SMA wire, which affects the achievable actuation frequency. Additionally, the force output is constrained by the interplay between the SMA wire's transformation stress and the elastic force of the biasing spring. Proper selection of SMA wire parameters and spring stiffness is thus critical for optimizing actuation performance.

The application of this actuation scheme in bio-inspired flapping drones presents an interesting trade-off. While the system allows for lightweight and mechanically simple designs, the limitation in frequency response due to thermal constraints may impact its feasibility for sustained aerodynamic thrust generation. Further research into active cooling techniques and optimized SMA compositions could enhance the viability of this approach for high-frequency actuation in robotic applications.

SMA wire with SMA-Load System

The implementation of a dual SMA wire actuation system in an agonist-antagonist configuration presents a significant advancement in the field of bio-inspired robotics. Unlike conventional SMA actuation schemes, where a single wire or a biased return mechanism is used, this approach leverages the interplay between two SMA wires to achieve bidirectional motion with improved controllability. This topology allows each wire to act as a load for the other, thereby creating a self-contained system where external elastic restoring forces are not required.

In this configuration, the two SMA wires are positioned in opposition, such that when one wire is activated and contracts (transitioning to its austenitic phase), the other is simultaneously stretched, entering its detwinned martensitic phase. Motion is achieved by alternating the activation of the two wires: when one wire is heated via electrical current, increasing its temperature and inducing phase transformation, the other cools down and returns to its martensitic state. This alternating cycle of contraction and elongation allows for continuous actuation, generating movement at a frequency dictated by the thermal response time of the SMA material.

From a mechanical perspective, the working principle can be visualized through the stress-strain behavior of the two SMA wires. Each wire exhibits a characteristic hysteresis loop, where its mechanical properties vary depending on the current phase transformation state. The interaction of these two hysteresis loops determines the system's equilibrium points, which shift dynamically as the thermal activation of the SMA wires progresses. Initially, when one wire is in its fully austenitic phase, the opposing wire remains in detwinned martensitic form, establishing a unique equilibrium point. As the second wire is progressively activated, its stress-strain curve shifts upward, while the first wire undergoes unloading, moving downward in its own stress-strain space.

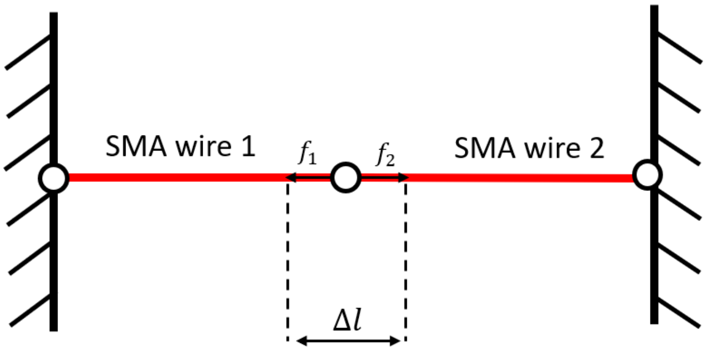

Figure 2.5: Schematic representation of a SMA wire-spring system

This behavior results in a gradual transition of the equilibrium point, governing the motion of the system. A key feature of this actuation strategy is the existence of multiple equilibrium points under certain thermal conditions. Without additional information about the history of the actuation cycle, it may not be possible to determine the correct equilibrium position at a given instant. However, by tracking the temperature evolution of each wire, it becomes possible to predict the correct trajectory of motion. As heating and cooling continue, the intersection of the two hysteresis loops migrates through the stress-strain diagram, ultimately leading to a fully transformed state in which one wire is completely in austenitic phase while the other is fully martensitic. The net displacement achieved by the system corresponds to the difference between the initial and final equilibrium points, defining the maximum achievable stroke of the actuation system.

This actuation approach offers several advantages over traditional SMA-based systems. By utilizing two opposing SMA wires, the system is capable of producing smooth, continuous motion without relying on external restoring forces, such as bias springs or mechanical constraints. Additionally, the alternating activation scheme allows for more efficient use of thermal energy, as the cooling of one wire is naturally aided by the simultaneous contraction of the opposing wire. This dual-wire setup also improves the overall response time by reducing the dependence on passive cooling mechanisms, a common limitation in single-wire SMA actuators.

The implementation of this actuation topology in flapping-wing drones represents a crucial step towards achieving biomimetic flight with SMA-based artificial muscles. By harnessing the high power-to-weight ratio of SMA micro-wires in an agonist-antagonist arrangement, it becomes possible to generate the necessary aerodynamic forces for sustained flight while maintaining a lightweight and compact system architecture. Future optimizations in material composition, thermal management, and control algorithms will further enhance the performance of SMA-based robotic systems, pushing the boundaries of bio-inspired aerial locomotion.

2.2.3 Challenges in SMA Actuation

While SMA actuators offer significant advantages in terms of force generation and displacement, there are several challenges associated with their use. These include:

- **Thermal Management:** SMAs are temperature-sensitive materials, and precise temperature control is crucial for reliable actuation. The heating and cooling cycles must be carefully controlled to ensure that the material transitions between the martensitic and austenitic phases at the desired temperatures.
- **Hysteresis Losses:** The hysteresis loop observed in the stress-strain behavior of SMAs can result in energy losses during actuation. These losses can affect the efficiency of the actuator, especially in systems that require repeated actuation cycles.
- **Fatigue and Durability:** Repeated phase transformations can lead to fatigue in the material, reducing the actuator's performance over time. The longevity of SMA actuators depends on factors such as temperature cycles, strain amplitude, and the material's composition[26].

Addressing these challenges is essential for the successful application of SMAs in bio-inspired systems, such as actuators for artificial wings in drones, which will be discussed in subsequent chapters.

2.3 SMA Modelling

The modeling of Shape Memory Alloys (SMAs) is crucial for understanding their mechanical and thermal behavior, as well as for designing efficient actuators and predicting their response under various operating conditions. SMA models are developed to predict how the materials will respond to mechanical forces, temperature variations, and load cycles. There are both single-crystal and polycrystalline models that address the microscopic and macroscopic behavior of SMAs.

2.3.1 Single-Crystal Modeling

Single-crystal modeling focuses on the behavior of an individual crystal of an SMA, which exhibits anisotropic behavior due to its crystallographic properties. When an SMA crystal undergoes a phase change, its lattice structure deforms, and there are movements along the twin boundaries. The phase transition from martensite to austenite, or vice versa, is the basis of the primary characteristics of SMAs: shape recovery and pseudoelasticity[21].

Gibbs Free Energy and Phase Transition

The theoretical foundation of single-crystal modeling is the minimization of the Gibbs free energy G, which accounts for both mechanical and thermal energies associated with the two phases, martensite and austenite. The Gibbs free energy function for an SMA crystal can be expressed as:

$$G = G_{\text{austenite}} + G_{\text{martensite}}$$

The Gibbs free energy for each phase depends on the temperature, composition, and strain state. For an SMA in transition, the phase with the lower Gibbs free energy predominates. Phase transformation begins when the difference in Gibbs free energy between the two phases reaches a critical value, triggering the phase change.

Single-Crystal Deformation Model

The deformation of an SMA crystal during phase transition is described by a phase transformation model that considers the effect of applied mechanical stress on the phase distribution between martensite and austenite. The total strain ϵ_{total} in an SMA crystal can be represented as the sum of elastic strain and strain due to phase transformation:

$$\epsilon_{\text{total}} = \epsilon_{\text{elastic}} + \epsilon_{\text{transformation}}$$

where: - $\epsilon_{\text{elastic}}$ is the reversible elastic strain, - $\epsilon_{\text{transformation}}$ is the plastic strain associated with the phase transition.

The elastic strain $\epsilon_{\text{elastic}}$ can be expressed in terms of the applied stress σ and the Young's modulus E:

$$\epsilon_{\text{elastic}} = \frac{\sigma}{E}$$

On the other hand, the strain due to phase transformation is a function of the phase fraction ξ and the phase difference between martensite and austenite. This can be modeled using a set of nonlinear equations that describe the microscopic behavior of the material.

Creep and Fatigue Modeling

In addition to elastic and plastic deformation, SMAs may experience viscoelastic creep and fatigue due to repeated loading cycles. For creep, the strain rate $\dot{\epsilon}$ can be described by an exponential relationship with the applied stress σ:

$$\dot{\epsilon} = A \cdot \sigma^n \cdot \exp\left(\frac{-Q}{RT}\right)$$

where: - A is a material-dependent parameter that varies with temperature, - n is the stress sensitivity exponent, - Q is the activation energy for viscous deformation, - R is the gas constant, - T is the absolute temperature. Fatigue in SMAs is related to the degradation of the material due to repeated heating and cooling cycles, which can lead to a reduction in shape recovery and the loss of the shape memory effect. Fatigue models for SMAs are often based on empirical laws that describe the accumulation of damage during phase transformation cycles, typically expressed as:

$$N_f = C \cdot (\Delta\sigma)^{-m}$$

where: - N_f is the number of fatigue cycles, - C is a constant that depends on the material, - $\Delta\sigma$ is the stress range, - m is the exponent that describes the fatigue behavior.

2.3.2 Polycrystalline Modeling

Polycrystalline modeling describes the behavior of an SMA material composed of multiple crystals, each with a different orientation. This approach is more complex than single-crystal modeling as it must account for the interactions between crystals and inhomogeneities in the behavior of martensite and austenite phases[15].

Mean-Field Model

A common approach to modeling polycrystalline SMA behavior is the mean-field model, which provides an average description of the behavior of individual crystals. In this model, a statistical distribution of phase fraction ξ is considered, which describes the proportion of crystals in the material that are in each phase (martensite or austenite). The average phase fraction is used to obtain a macroscopic response. The macroscopic response of the material can be expressed as:

$$\epsilon_{\text{macro}} = \langle \epsilon_{\text{elastic}} \rangle + \langle \epsilon_{\text{transformation}} \rangle$$

In this case, the $\langle \cdot \rangle$ operator denotes a statistical average over the individual crystals. This approach reduces the computational complexity compared to simulations at the single-crystal level, but it still captures the effects of crystal interactions and phase transformations.

Finite Element Modeling (FEM)

Finite element modeling (FEM) is another powerful approach for studying the behavior of polycrystalline SMAs, allowing detailed simulations of crystal interactions and the effects of inhomogeneities. With FEM, the material is divided into small elements, each of which is treated as a single crystal with anisotropic behavior.

Numerical simulation through FEM can be used to study the evolution of martensite and austenite phases in a polycrystalline material under loading conditions, predicting the overall material response, including phase propagation, energy dissipation, and nonlinear behavior.

An example of formulating a polycrystalline SMA problem in FEM is solving for the thermomechanical equilibrium for each element, which involves temperature and internal forces:

$$F_{\text{internal}} = \int_{\Omega} \sigma_{\text{SMA}} \, dV$$

where: - F_{internal} is the internal force generated by the phase transitions in each element, - Ω is the material domain, - σ_{SMA} is the stress generated by the phase change.

Shape Memory Alloys provide an innovative and versatile solution for actuation in bio-inspired systems. Their unique thermomechanical properties, such as the Shape Memory Effect and pseudoelasticity, enable them to perform mechanical work with minimal weight and energy consumption. By understanding the internal structure and transformation mechanisms of SMAs, we can design highly efficient actuators for a range of applications, from medical devices to robotics.

In the context of bio-inspired drones, SMAs offer the potential for muscle-like actuation, mimicking the natural movement of biological systems. Their ability to work in agonist-antagonist configurations makes them particularly well-suited for driving wing motion in bio-inspired flight systems, as will be discussed in subsequent chapters. The challenges associated with controlling the temperature and mechanical properties of SMAs will be addressed through advanced modeling and system design, ensuring that SMAs can be successfully integrated into bio-inspired flight systems.

Chapter 3

SMA-driven Flapping Wing

This chapter focuses on the development and analysis of a flapping wing system actuated by Shape Memory Alloys (SMA), a core component in the realization of bio-inspired micro-aerial vehicles. Thanks to their unique properties, SMAs provide a lightweight, compact, and efficient solution for actuating the flapping motion, which is fundamental to achieving flight inspired by natural flyers such as insects and birds.

The chapter is divided into three main sections, each addressing a critical aspect of the SMA-driven flapping wing. The first section (3.1 Antagonistic SMA Wing Actuation) delves into the design of an actuation mechanism employing SMA elements in an antagonistic configuration, allowing for controlled and efficient wing movement. This includes the modeling of wing kinematics and the evaluation of the system through simulations.

The second section (3.2 Resonant Compliant Joint) explores the design and implementation of compliant joints that enhance the resonance properties of the wing system. This approach minimizes energy consumption and optimizes the mechanical performance, ensuring smooth and stable flapping dynamics. Modeling and simulation results are presented to validate the effectiveness of the design.

The final section (3.3 Wing Membrane) addresses the design and integration of the wing membrane, a critical component for aerodynamic performance. The section includes an analysis of the membrane's material properties, structural design, and simulation results to demonstrate its role in enhancing lift and thrust during flight.

3.1 Antagonistic SMA Wing Actuation

3.1.1 Design

The agonist-antagonist actuation technique was the first actuation idea implemented on the wings, with the SMA micro-wires used as artificial muscles to articulate joints. This approach, in addition to enhancing performance, brings the design closer to its biological counterpart not only aesthetically but also functionally: the agonist-antagonist muscle configuration is found in nearly all joints of mammals, including humans, due to its ability to provide greater freedom of movement.

While the shoulder muscles of animals feature multiple agonist-antagonist pairs, which add freedom of movement but also high complexity, we aimed to create a simpler system with SMA wires, incorporating just a single agonist-antagonist pair arranged symmetrically around a central joint. The operation of the system is straightforward: by activating either the agonist or the antagonist SMA muscle (alternately), the actuators pull the arm connected to the joint, causing it to rotate in one direction or the other, depending on which SMA is activated (see Figure 3.1).

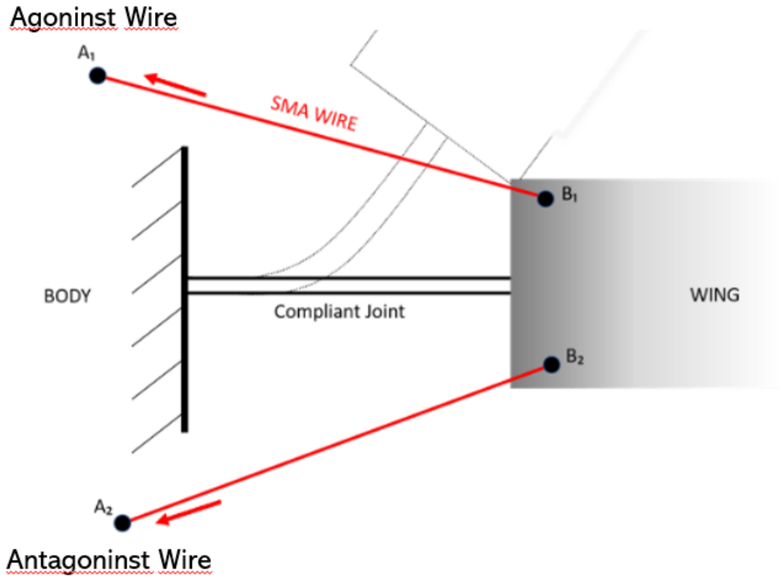

Figure 3.1: Illustration of the shoulder joint actuated by SMA antagonist and agonist wires

From this basic concept, practical considerations arise, such as the required contraction length and force of the SMA wire to actuate the joint, as well as the maximum frequency needed to achieve acceptable motion. The design parameters directly influencing these factors are primarily the wire diameter, the location of the SMA wire's "actuation" point (the end attached to the moving arm), and the location of the "starting" point (the end attached to the body of the robot, which we will consider as the fixed end). Of course, the type of joint selected also influences the performance in terms of force and movement. However, for an analytical study focused solely on the SMA wires and their arrangement, we consider a virtual joint with negligible friction and purely rotational movement around its axis. The results and observations made under these conditions remain valid even when the model complexity is increased later on. Furthermore, the following geometric study will focus on just one SMA wire (assumed to be the "agonist" upper wire), as identical results can be obtained symmetrically by considering the opposite wire.

3.1.2 Modeling - Wing Kinematics

We begin by modeling the simplified system of the joint-arm actuated by a single SMA wire in one direction. The coordinates of the wire's attachment points, fixed to the body and the moving arm, are denoted in Figure 3.2 as x_1, y_1 and x_2, y_2, respectively. The joint motion is restricted to a single plane, with the joint being assumed to have a single degree of freedom (purely rotary motion) that allow the the wing to rotate with an angle θ from the horizontal axis. The coordinates of the attachment point x_2, y_2 fixed to the wing are considered with respect to a rotating reference frame that moves with the arm, simplifying the design implementation.

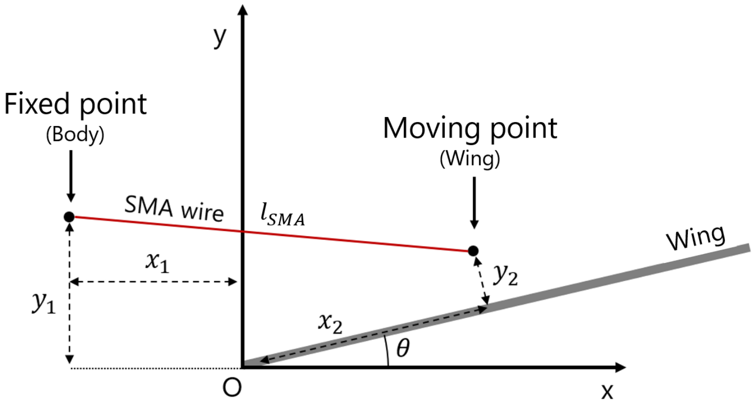

Figure 3.2: Geometric parametrization of the wing

Using a simple geometric equation, we can derive the length of the SMA wire based on these four coordinate values:

$$l_{\text{SMA}} = \sqrt{A\cos\theta + B\sin\theta + C} \tag{3.1}$$

where:

$$A = 2x_1x_2 - 2y_1y_2,$$
$$B = -2y_1x_2 - 2y_2x_1,$$
$$C = (l_0 - d_l)^2 - x_2^2 - x_1^2 - y_1^2 - y_2^2.$$

With the wire length and the angle of the wing relative to the horizontal axis (x-axis in Figure 3.2), we can begin a parametric analysis to calculate the maximum angle reached by the wing. We fix the variation in wire length and all geometric parameters except for the one we wish to analyze.

3.1.3 Simulation Results

Using the derived relationships and considering the variations in each parameter, we present the following simulation results, which demonstrate the influence of each parameter on the maximum angle of wing movement.

x_1	x_2	y_1	y_2	Δl_{sma}
$*$	4 mm	2 mm	1.5 mm	3 mm

Table 3.1: Geometric parameter table with x_1 as variable parameter.

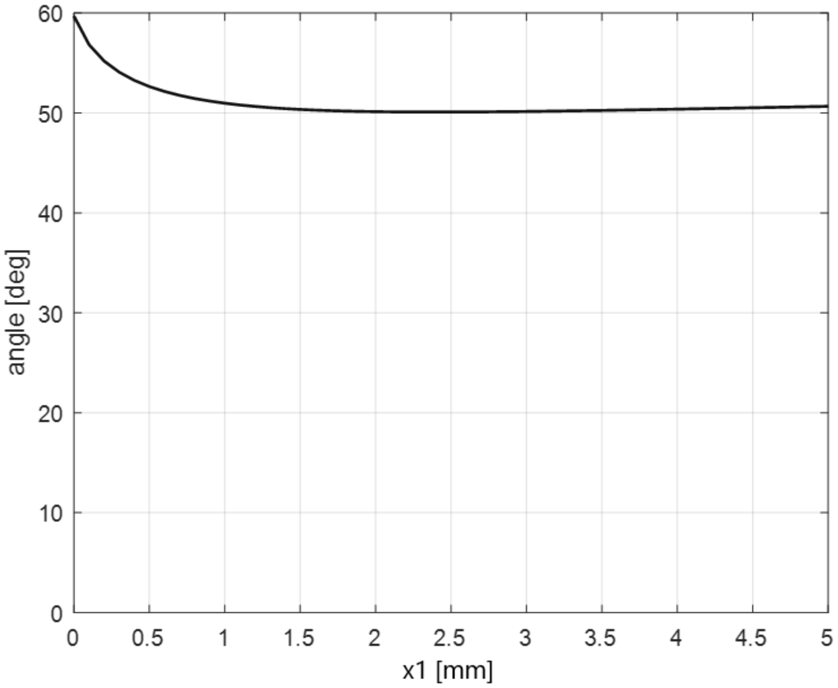

Figure 3.3: Trend of the wing angle with respect to the variation of x_1.

x_1	x_2	y_1	y_2	Δl_{sma}
1.5 mm	4 mm	$*$	1.5 mm	3 mm

Table 3.2: Geometric parameter table with y_1 as variable parameter.

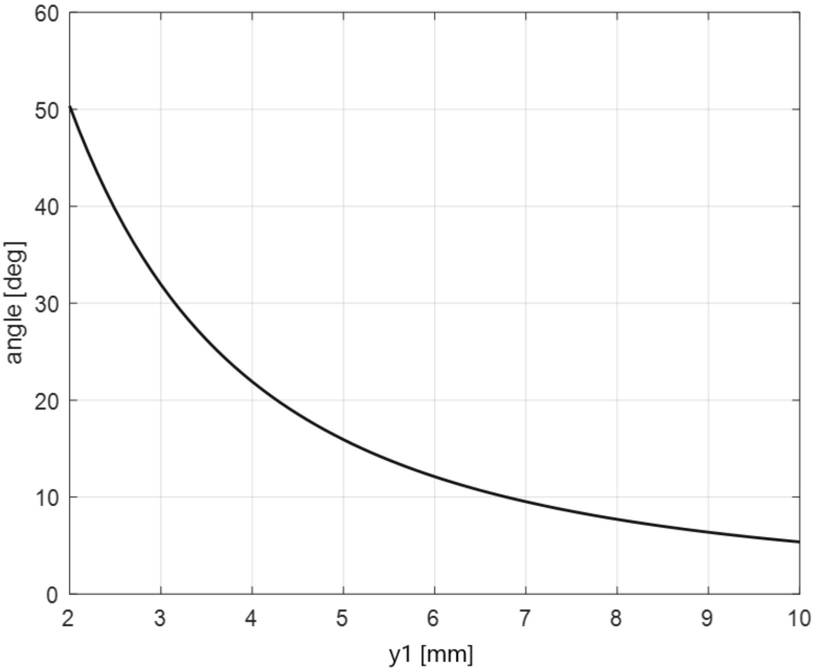

Figure 3.4: Trend of the wing angle with respect to the variation of y_1.

x_1	x_2	y_1	y_2	Δl_{sma}
1.5 mm	$*$	2 mm	1.5 mm	3 mm

Table 3.3: Geometric parameter table with x_2 as variable parameter.

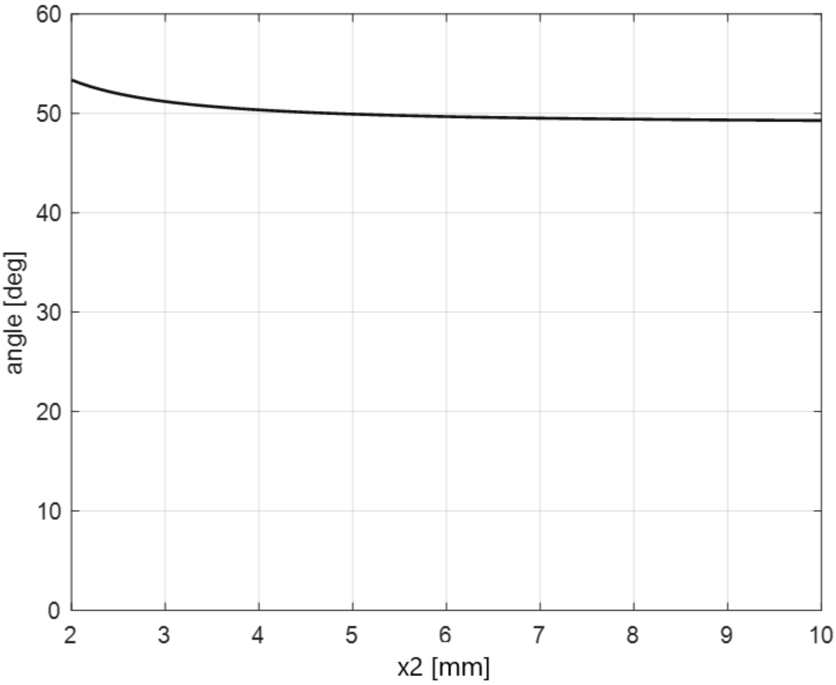

Figure 3.5: Trend of the wing angle with respect to the variation of x_2.

x_1	x_2	y_1	y_2	Δl_{sma}
1.5 mm	4 mm	2 mm	$*$	3 mm

Table 3.4: Geometric parameter table with y_2 as variable parameter.

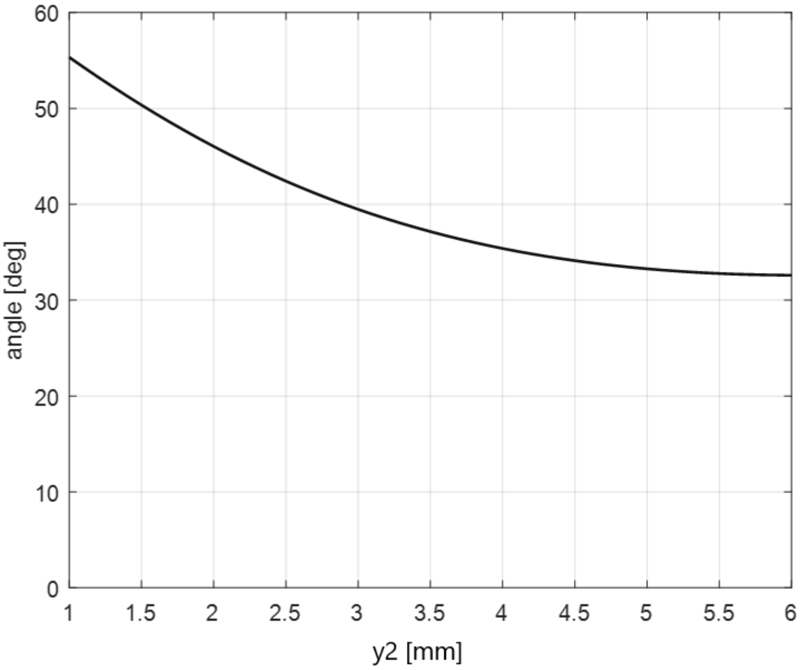

Figure 3.6: Trend of the wing angle with respect to the variation of y_2.

The results of the parametric study reveal that the parameters y_1 and y_2 have a greater influence on the maximum achievable angle than the parameters x_1 and x_2. This suggests that, as intuitively expected, to achieve a greater angle of movement, it is crucial to reduce the "height" of the wire attachment points—specifically, the distance between the attachment points and the joint neutral axis line. This insight leads to a design and assembly tolerance that must account for the significance of parameters y_1 and y_2 in relation to x_1 and x_2.

3.2 Resonant Compliant Joint

The decision to utilize a compliant joint instead of a conventional pin-based rotational joint is driven by several advantages that align with both functional and bio-inspired design principles. Compliant joints offer minimal or near-zero friction, ensuring smoother and more efficient motion. Additionally, they are consistent with a bio-inspired approach, replicating the fluid and natural movements observed in biological systems. The semi-soft structure of the compliant joint complements the flexibility of the SMA actuators, creating a harmonious integration between the actuator and joint.

Stainless steel was selected as the material for the compliant joint due to its durability, resilience, and suitability for precision manufacturing. This choice not only maintains the structural integrity of the system but also facilitates the exploitation of the joint's natural resonant frequency. As will be demonstrated in this subsection, leveraging the resonant frequency of the compliant joint significantly enhances the system's performance, providing a natural "boost" to the efficiency of the flapping motion while reducing energy consumption.

3.2.1 Design

The compliant joint is designed as a simple yet effective component: a thin metallic strip, with a thickness ranging from 0.05 mm to 0.1 mm, that connects the flapping wing to the drone body. This straightforward design eliminates the need for complex mechanical parts, reducing friction and enhancing reliability while keeping the structure lightweight.

As detailed in the following modeling section, the geometric properties of the strip - particularly its thickness, width, and length - play a crucial role in determining the joint's natural oscillation frequency. This frequency is influenced by the material properties of the joint and the dynamic characteristics of the attached wing, such as its inertia and weight.

By carefully selecting the strip's dimensions and using precise calculations, the joint can be tuned to oscillate naturally at the desired frequency, achieving resonance when paired with the wing. This approach not only maximizes the efficiency of the flapping motion but also aligns with the bio-inspired design principles of flexibility and simplicity, enhancing overall system performance.

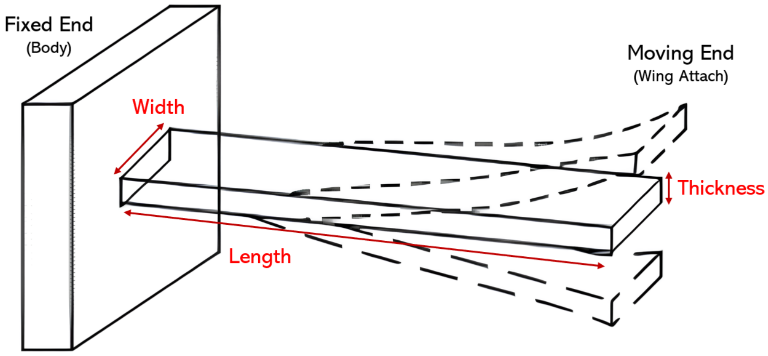

Figure 3.7: Illustration of the compliant joint made by a beam of stainless-steel

3.2.2 Modeling - Wing Dynamics

Torsional Stiffness of the Compliant Joint

The compliant joint is modeled as a cantilever beam, simplified into a rigid-body torsional spring with stiffness K. This approach allows us to analytically represent the compliant behavior of the joint, where the rotational stiffness is derived from the geometric and material properties of the beam. Using Bernoulli beam theory, we can relate the beam's deformation under a load to its stiffness.

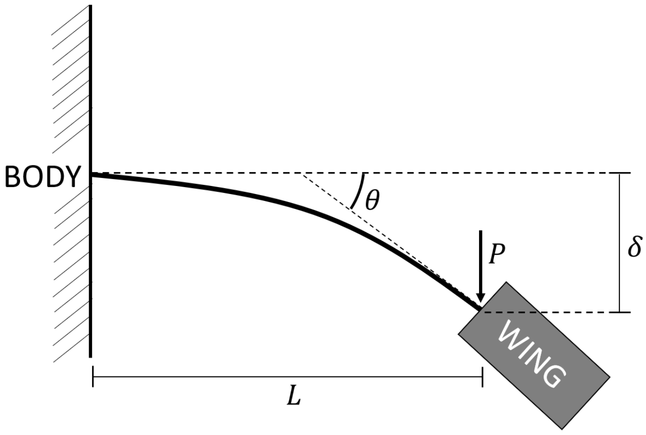

Figure 3.8: Cantilever beam representation of the shoulder joint

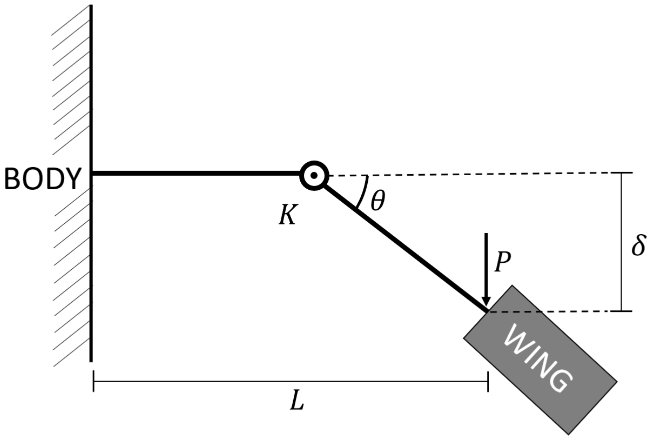

Figure 3.9: Rigid body equivalent representation of the shoulder joint

When a load P is applied at the free end of a cantilever beam of length L, the linear deflection δ and the angular rotation θ at the free end are given by the following equations:

$$\delta = \frac{P \cdot L^3}{3 \cdot E \cdot I} \tag{3.2}$$

$$\theta = \frac{P \cdot L^2}{2 \cdot E \cdot I} \tag{3.3}$$

Here:

- P is the applied load,
- E is the Young's modulus of the beam material,
- I is the second moment of area of the cross-section, defined as:

$$I = \frac{W \cdot T^3}{12} \tag{3.4}$$

- L, W, and T are the length, width, and thickness of the beam, respectively.

Using these equations, we can derive the rotational stiffness K of the beam. By definition, the torsional stiffness is the ratio of the applied moment M to the angular displacement θ:

$$K = \frac{M}{\theta} \tag{3.5}$$

For a cantilever beam under a concentrated load P, the moment at the fixed end is $M = P \cdot L$. Substituting M and θ into the equation for K, we get:

$$K = \frac{P \cdot L}{\frac{P \cdot L^2}{2 \cdot E \cdot I}} = \frac{2 \cdot E \cdot I}{L} \tag{3.6}$$

Finally, substituting the expression for I into the above equation, the rotational stiffness becomes:

$$K = \frac{2 \cdot E \cdot W \cdot T^3}{12 \cdot L} = \frac{E \cdot W \cdot T^3}{6 \cdot L} \tag{3.7}$$

This relationship highlights how the joint's rotational stiffness is directly influenced by its geometric parameters and material properties.

Natural Frequency of the Joint-Wing System

To investigate the resonant behavior of the joint-wing system, we consider the interaction between the wing's rotational inertia (J) and the compliant joint's stiffness (K). The damping term (b) is included for completeness but is not the focus of this analysis. The system is modeled as a second-order rotational dynamic system:

$$J \cdot \ddot{\theta} + b \cdot \dot{\theta} + K \cdot \theta = 0 \tag{3.8}$$

Here:

- J is the rotational inertia of the wing, determined from its mass and geometry,
- θ is the angular displacement of the wing,
- $\dot{\theta}$ and $\ddot{\theta}$ are the angular velocity and angular acceleration, respectively.

The natural angular frequency ω_n of the system, assuming no damping, is given by:

$$\omega_n = \sqrt{\frac{K}{J}} \tag{3.9}$$

The natural frequency in hertz is then:

$$f_n = \frac{\omega_n}{2\pi} = \frac{1}{2\pi}\sqrt{\frac{K}{J}} \tag{3.10}$$

By substituting the expression for K, we can relate the natural frequency to the geometric and material properties of the joint and the wing's inertia. This enables precise tuning of the joint to achieve the desired resonance.

Implementation in Simulink

The torsional spring model was implemented in Simulink using the Simscape Multibody library. CAD files of the wing components were imported, enabling automatic computation of the wing's mass and rotational inertia (J). The joint was modeled as a revolute joint with stiffness K derived from the previous equations. To simulate the wing's motion, fictitious cable elements were incorporated, mimicking the actuation of Shape Memory Alloys (SMA). These cables dynamically adjusts their lengths based on the SMA model described in Chapter 2, driving the rotation of the joint. This approach allowed for accurate simulation of the joint-wing system dynamics, ensuring that the theoretical resonant frequency aligned with the experimental results.

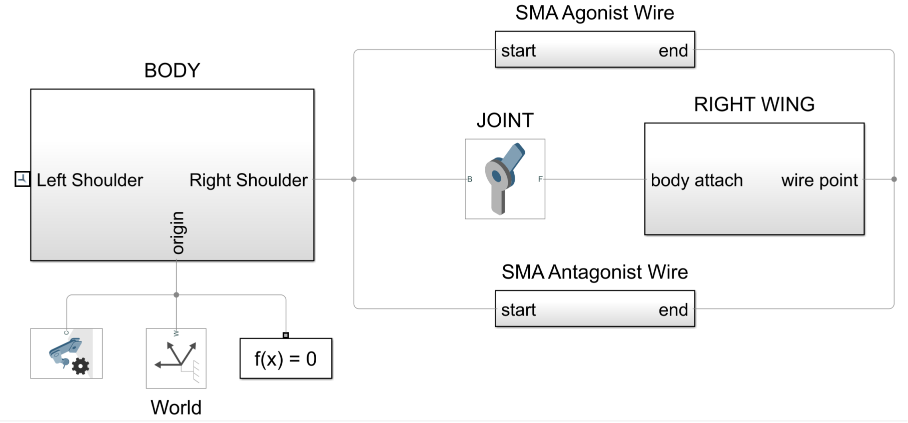

Figure 3.10: Rigid body equivalent representation of the shoulder joint

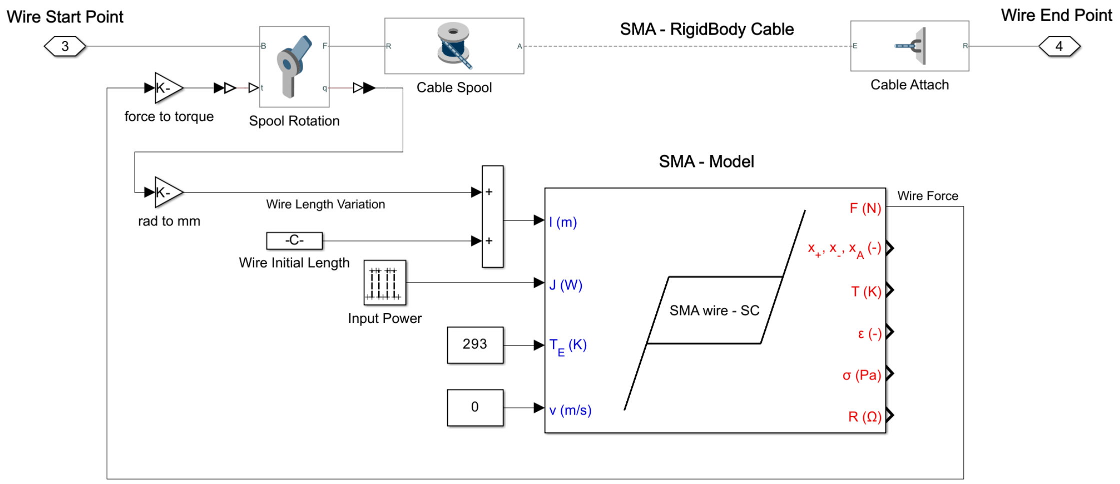

Figure 3.11: Rigid body equivalent representation of the shoulder joint

Simulation Results

To evaluate the effectiveness of the resonant compliant joint, simulations were conducted using the model developed in the previous section. Two cases were analyzed: (1) a low-stiffness joint, which mimics a traditional pin-based revolute joint with minimal rotational stiffness, and (2) a resonant compliant joint tuned to a natural frequency of 5 Hz. The performance of the joint-wing system was assessed at driving frequencies of 1 Hz and 5 Hz.

Low-Stiffness Joint The first simulation evaluates a joint with low rotational stiffness K, resembling a standard revolute joint. Figure 3.12a shows the input signal applied at 1 Hz, while Figure 3.12b illustrates the corresponding output. At this low frequency, the wing achieves a satisfactory angular displacement, with the total swept angle exceeding 40 degrees.
At 5 Hz, the low-stiffness joint fails to deliver adequate performance. As shown in Figure 3.13a, the applied input signal amplitude remains consistent, but the output response (Figure 3.13b) is significantly diminished. The total angular displacement does not exceed 40 degrees, confirming that the system is incapable of effectively oscillating at higher frequencies.

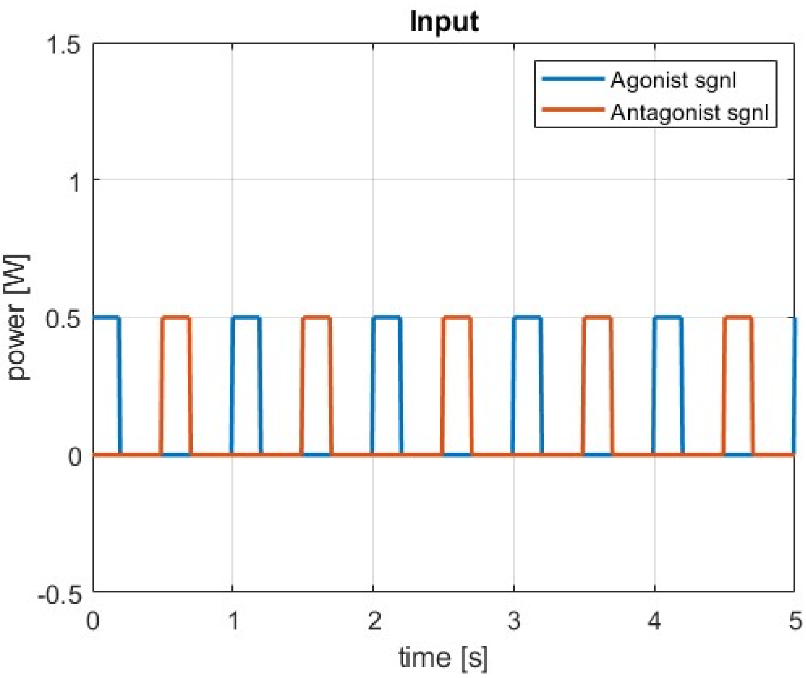

(a) Input signal at 1 Hz.

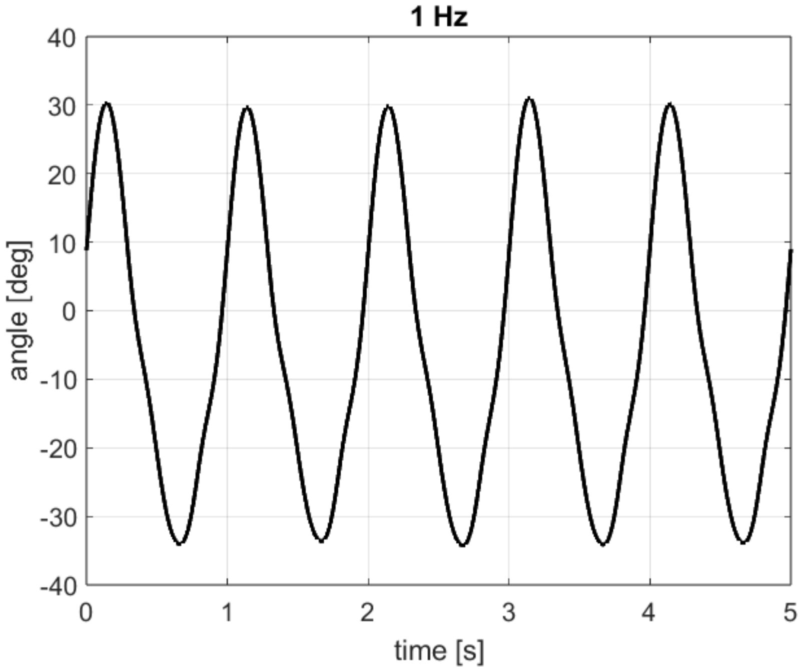

(b) Simulated flapping angle.

Figure 3.12: Simulation results for low-stiffness joint at 1 Hz.

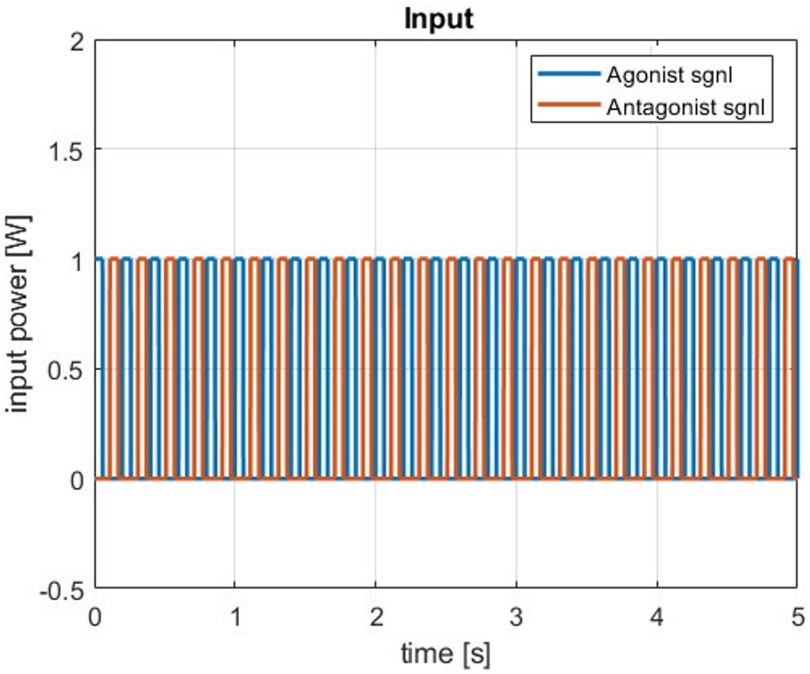

(a) Input signal at 5 Hz.

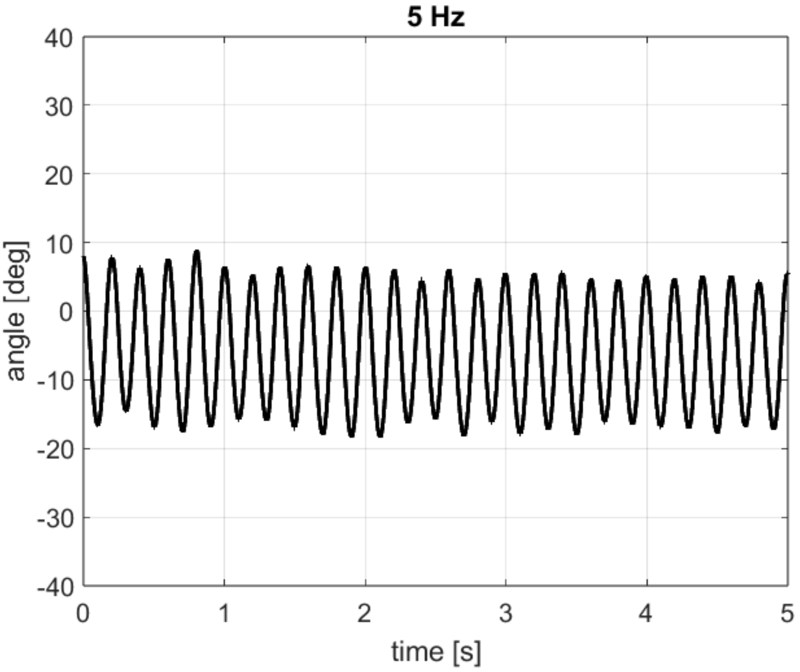

(b) Simulated flapping angle.

Figure 3.13: Simulation results for low-stiffness joint at 5 Hz.

Resonant Compliant Joint Performance To evaluate the resonant compliant joint, the joint stiffness K was tuned to achieve a natural frequency of 5 Hz. Using the inertial properties of the wing ($J = 1.3 \times 10^{-5}\,\mathrm{kg} \cdot \mathrm{m}^2$) derived from its CAD model, and following the relationships introduced in the modeling subsection, K was calculated as:

$$K = \omega_n^2 \cdot J$$

where $\omega_n = 2\pi f_n = 31.42\,\mathrm{rad/s}$ corresponds to $f_n = 5\,\mathrm{Hz}$. Substituting the values yields:

$$K = (31.42)^2 \cdot (1.3 \times 10^{-5}) = 12.84\,\mathrm{N} \cdot \mathrm{m/rad}$$

This stiffness was implemented in the Simulink model to simulate the resonant behavior.

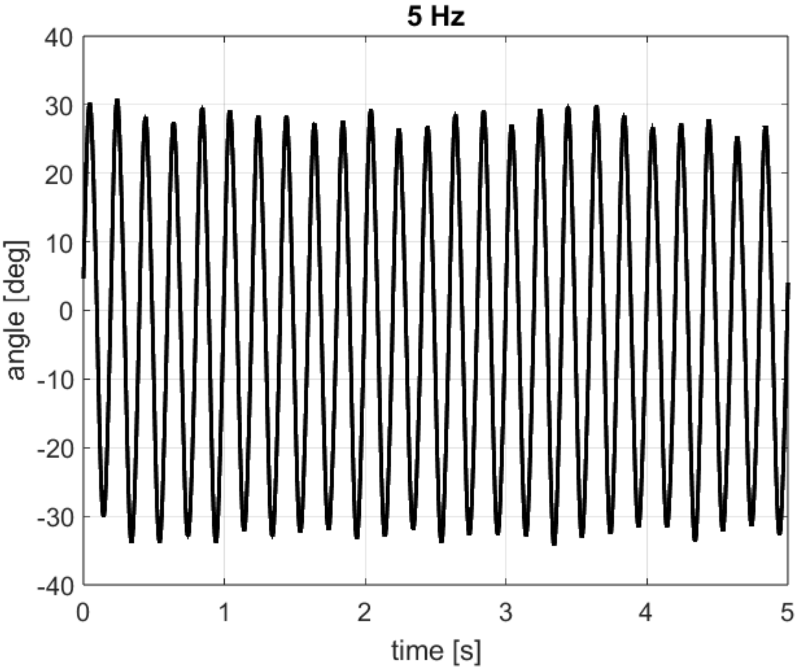

Figure 3.14: Simulation results for low-stiffness joint at 5 Hz.

The input signal applied is identical to that used in the low-stiffness case (Figure 3.13a, but the output response (Figure 3.14) shows significant improvement. The wing achieves a total swept angle of approximately 80 degrees, confirming that resonance enables efficient oscillation at 5 Hz without increasing energy input.

The simulations demonstrate that the low-stiffness joint is incapable of achieving effective oscillation at higher frequencies, while the resonant compliant joint achieves significant performance improvements at 5 Hz without additional energy input. The results validate the concept of a resonant compliant joint, which, as shown in the next chapter, is further corroborated by experimental results.

3.3 Wing Membrane

3.3.1 Design

The design of the wing membrane is a critical aspect in ensuring the aerodynamic and structural performance of flapping-wing micro-aerial vehicles (MAVs). Drawing inspiration from natural flyers such as birds and bats, the wing membrane must balance flexibility and stiffness to achieve efficient force generation during flapping cycles. Its design not only influences lift and thrust production but also contributes to energy storage and damping, which are essential for reducing power consumption. The geometry of the wing membrane typically follows a semi-elliptical planform, as this shape has been shown to provide favorable aerodynamic characteristics by minimizing induced drag while maximizing lift distribution along the span. The chord length of the wing membrane often varies linearly from root to tip, which allows for natural pitching during the flapping motion and ensures that the aerodynamic load is evenly distributed.

Material selection is another crucial factor in the design of the membrane. Lightweight, elastic polymers such as polyurethane films or latex are commonly chosen for their ability to deform under aerodynamic loads while maintaining structural integrity. These materials provide the flexibility needed for passive deformation, which enhances thrust generation during the downstroke and minimizes resistance during the upstroke. To provide the necessary structural support, carbon fiber or composite spars are used along the leading edge and other critical regions of the wing. These spars act as load-bearing members that guide the flapping motion and transmit forces effectively to the main structure.

An additional consideration in the design of the wing membrane is its interaction with unsteady aerodynamic phenomena. The membrane's ability to deform passively under fluctuating aerodynamic loads is essential for maximizing force generation and stability. This property mimics the behavior of biological wings, where the compliant nature of the membrane aids in adapting to varying flow conditions and prevents sudden losses in lift or thrust.

To summarize, several key parameters govern the design of the wing membrane:

- **Aspect Ratio (AR)**: Defined as $AR = B^2/S$, where B is the wingspan and S is the wing area. A moderate aspect ratio balances aerodynamic efficiency and structural stability, reducing induced drag without introducing excessive structural complexity.

- **Elasticity**: The flexibility of the membrane material enables energy storage and release during flapping, improving the overall efficiency of the ornithopter and reducing actuator energy demands.

- **Wing Loading**: Minimizing wing loading, defined as the total mass per unit wing area, ensures sufficient lift generation while maintaining structural strength and stability.

- **Material Choice**: Lightweight, elastic polymers such as polyurethane or latex are combined with carbon fiber spars to create a wing that balances flexibility and stiffness.

The integration of these parameters ensures that the wing membrane achieves a balance between aerodynamic performance and mechanical efficiency. These considerations provide the foundation for the aerodynamic modeling and simulation of the membrane's performance in subsequent sections.

3.3.2 Modeling

The aerodynamic modeling of the wing membrane is based on blade-element theory combined with unsteady aerodynamic corrections. This model enables the computation of the aerodynamic forces, particularly lift (F_{lift}) and thrust (F_{thrust}), generated during flapping-wing motion. The approach incorporates the Kutta-Joukowski condition for determining circulation-based lift and applies the Theodorsen lift deficiency factor to account for unsteady effects at low Reynolds numbers.

The wing's motion is parameterized by flapping (β) and pitching (θ) angles, expressed as:

$$\beta(t) = \beta_{max}\sin(\omega t), \quad \theta(t) = \theta_0\cos(\omega t + \phi),$$

where β_{max} is the maximum flapping amplitude, θ_0 is the maximum pitching angle, $\omega = 2\pi f$ is the flapping frequency, and ϕ is the phase lag between flapping and pitching. These kinematics result in both translational and rotational motion of the wing.

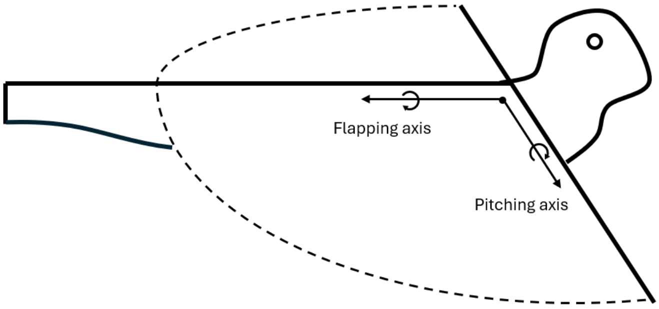

Figure 3.15: Schematic representation of wing's movement main axes.

The relative velocity V of air over the wing is derived from the horizontal and vertical components:

$$u = U + r\dot{\theta}\cos\beta, \quad v = r\dot{\beta} - r\dot{\theta}\sin\beta,$$

where U is the forward flight velocity, r is the spanwise position from the root, and $\dot{\beta}, \dot{\theta}$ are the time derivatives of the flapping and pitching angles, respectively. The magnitude of the relative velocity is:

$$V = \sqrt{u^2 + v^2}.$$

The angle of attack α is given by:

$$\alpha = \arctan\left(\frac{v}{u}\right) - \theta.$$

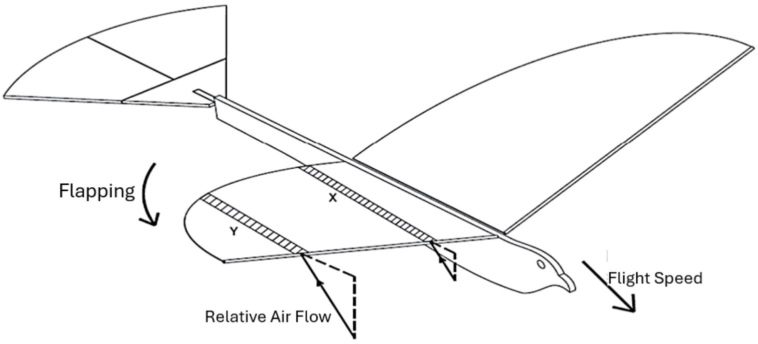

Figure 3.16: Representation of air-flow components on the wing.

The aerodynamic forces are calculated using the Kutta-Joukowski condition:

$$L' = \rho V \Gamma,$$

where L' is the lift per unit span, ρ is the air density, V is the relative velocity, and Γ is the circulation. The circulation is related to the airfoil geometry and angle of attack through:

$$\Gamma = 2\pi \alpha c,$$

where c is the local chord length.
The drag per unit span (D') is determined from:

$$D' = \frac{1}{2}\rho V^2 C_d c,$$

where C_d is the drag coefficient, incorporating profile drag (C_{dp}) and induced drag corrections:

$$C_d = C_{dp} + \frac{C_l^2}{\pi e AR}.$$

The lift (dL) and drag (dD) forces on a small blade element are resolved into thrust (dF_{thrust}) and lift (dF_{lift}) components:

$$dF_{lift} = dL\cos\alpha - dD\sin\alpha, \quad dF_{thrust} = dL\sin\alpha + dD\cos\alpha.$$

The total aerodynamic forces over the span are obtained by integrating across the wing:

$$F_{lift} = \int_0^B dF_{lift}\,dr, \quad F_{thrust} = \int_0^B dF_{thrust}\,dr.$$

At low Reynolds numbers, unsteady aerodynamic effects play a significant role in determining the lift. These effects are captured using the Theodorsen lift deficiency factor ($C(k)$), which modifies the quasi-steady lift to account for vortex shedding and delayed stall. The lift per unit span becomes:

$$L' = \rho V c C_l C(k),$$

where $k = \frac{\omega c}{2V}$ is the reduced frequency, a dimensionless parameter quantifying the unsteadiness of the flow. The Theodorsen function $C(k)$ is complex and incorporates circulatory and non-circulatory effects, given by:

$$C(k) = \frac{H_1^{(2)}(k)}{H_1^{(2)}(k) + iH_0^{(2)}(k)},$$

where $H_0^{(2)}(k)$ and $H_1^{(2)}(k)$ are Hankel functions of the second kind.
To compute the time-averaged aerodynamic forces over a complete flapping cycle, the instantaneous forces are integrated over time:

$$F_{lift} = \frac{1}{T} \int_0^T \int_0^B dF_{lift}\, dr\, dt, \quad F_{thrust} = \frac{1}{T} \int_0^T \int_0^B dF_{thrust}\, dr\, dt,$$

where $T = \frac{1}{f}$ is the flapping period.
This model, combining quasi-steady and unsteady aerodynamic principles, provides the theoretical foundation for evaluating lift and thrust in the next subsection on Simulation Results. MATLAB simulations will be used to validate these predictions and optimize the wing membrane's performance.

3.3.3 Simulation Results

To evaluate the aerodynamic performance of the wing membrane, numerical simulations were conducted using a MATLAB-based script. The aerodynamic model described earlier was implemented with the following input parameters:

- Half-wingspan (b): 16 mm
- Wing chord length (c): 7 mm, resulting in an aspect ratio (AR) of approximately 4.5
- Relative airspeed (U): 5 m/s, corresponding to the horizontal velocity of the drone in flight
- Flapping frequency (f): 5 Hz
- Flapping angle amplitude (β_{max}): 60 degrees
- Pitch angle amplitude (θ_0): 30 degrees
- Phase lag between flapping and pitching (ϕ): 90 degrees
- Dihedral angle: 5 degrees
- Incidence angle at the shoulder joint: 10 degrees

These parameters were selected to emulate realistic flight conditions for the ornithopter, with symmetrical motion applied to both the left and right wings. The simulation computes the aerodynamic forces of lift and thrust over time, based on the input flapping and pitching angles.

The flapping and pitching motions used as input for the model are shown in Figure 3.17a. The resulting aerodynamic lift and thrust forces are shown in Figures 3.17b and 3.18, respectively. Each force plot includes the time-averaged value, providing an indication of the overall aerodynamic force generated. The average

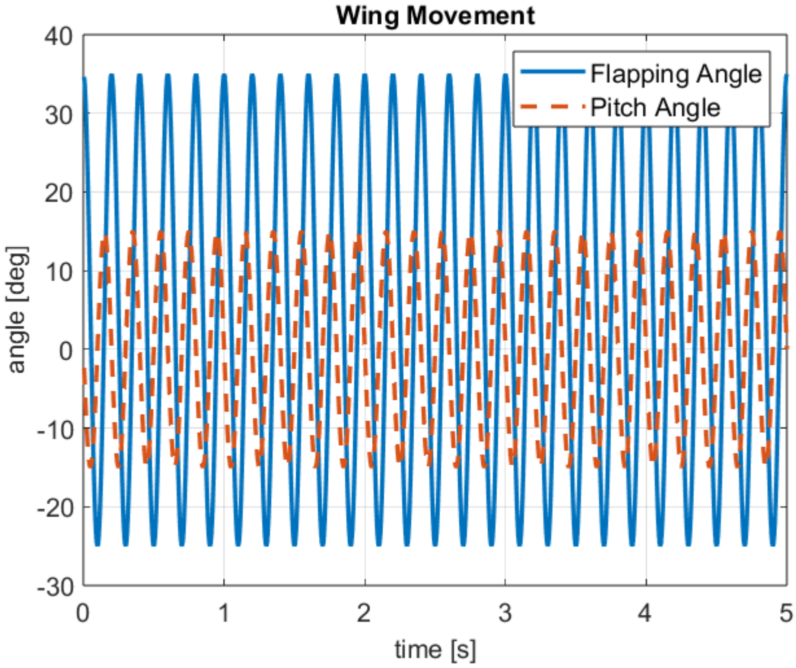

(a) Flapping and pitching angles (input).

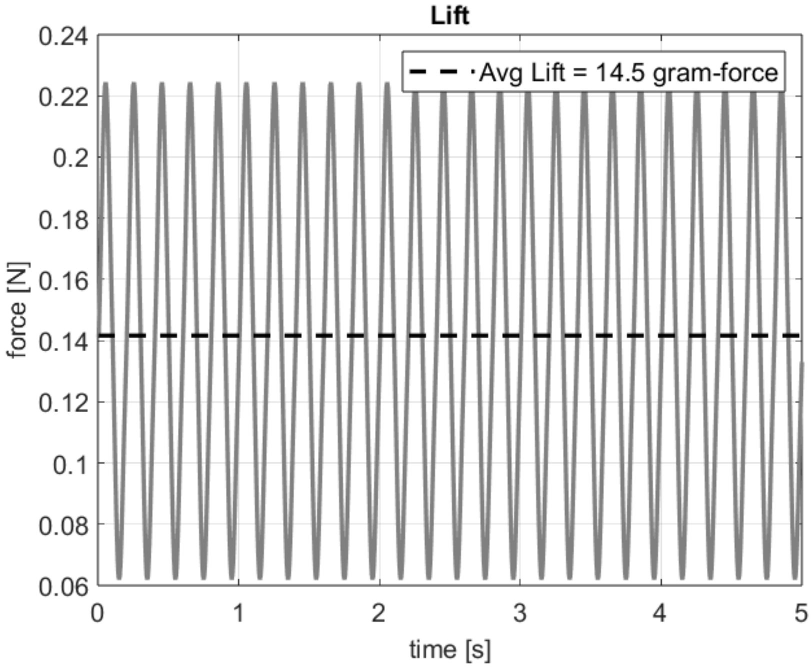

(b) Aerodynamic lift force (output).

Figure 3.17: Wing angles and simulated lift.

aerodynamic lift obtained from the simulation was approximately 14.5 gram-force

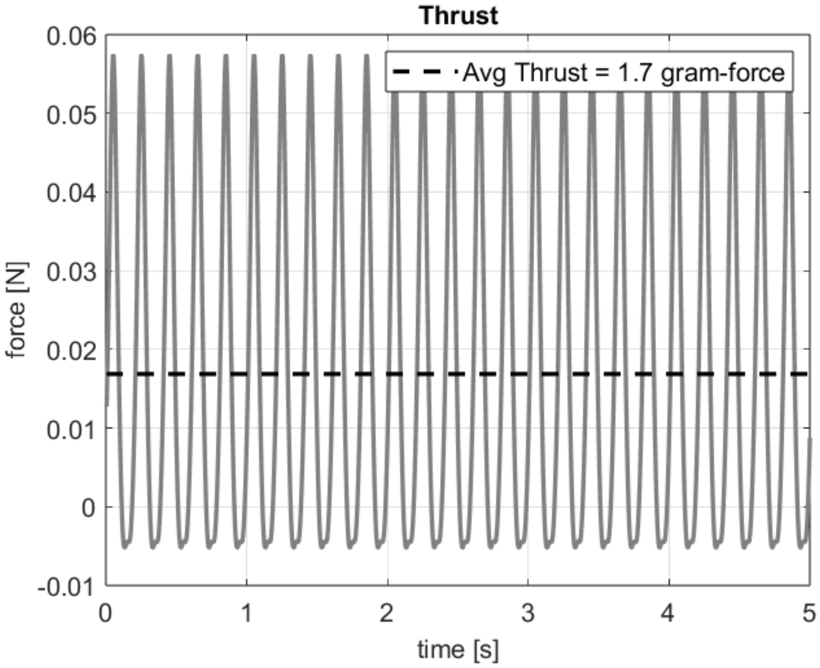

Figure 3.18: Simulated aerodynamic thrust force (output)

(0.142 N), while the thrust averaged around 1.7 gram-force (0.017 N). These values demonstrate the wing membrane's ability to generate sufficient aerodynamic forces to support flight under the specified conditions.

Aspect Ratio (AR). The aspect ratio was varied from 4 to 8, while keeping all other parameters constant. As shown in Figure 3.19, both lift and thrust increase with higher AR. This is because increasing AR reduces induced drag and improves aerodynamic efficiency. However, practical constraints such as the limited dimensions of the prototype and the mechanical strength of the SMA actuators restrict AR to moderate values. For this specific prototype, an aspect ratio of approximately 4.5 was chosen as optimal to balance aerodynamic performance and structural feasibility.

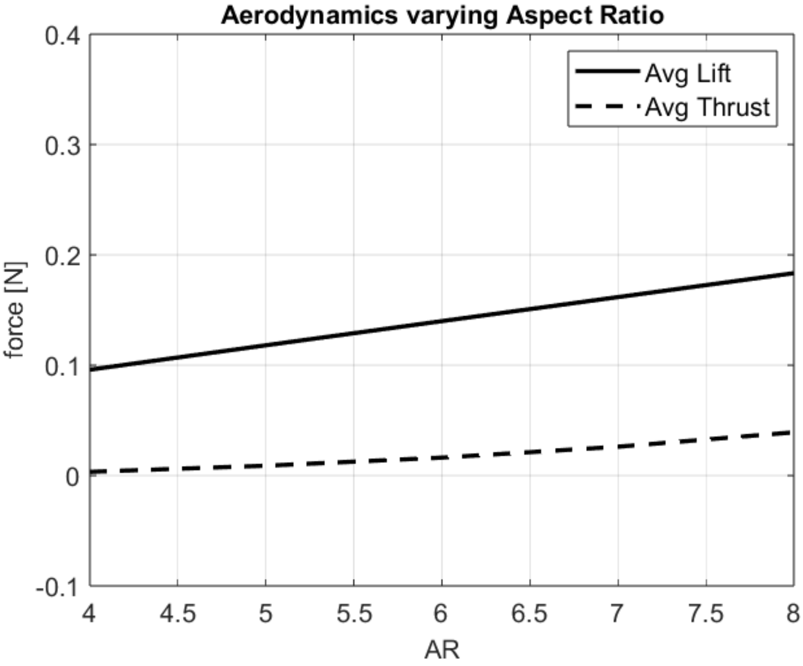

Figure 3.19: Aerodynamic lift and thrust forces as a function of the aspect ratio (AR).

Flapping Frequency. The flapping frequency was varied from 2 Hz to 8 Hz. The results, shown in Figure 3.20, indicate that thrust increases slightly with higher frequency, while lift remains relatively constant or slightly decreases. This behavior reflects the diminishing returns of aerodynamic force generation at higher frequencies. For the prototype, the optimal flapping frequency was selected as 5 Hz, aligning with the resonant frequency of the compliant joint and within the capabilities of the SMA actuators.

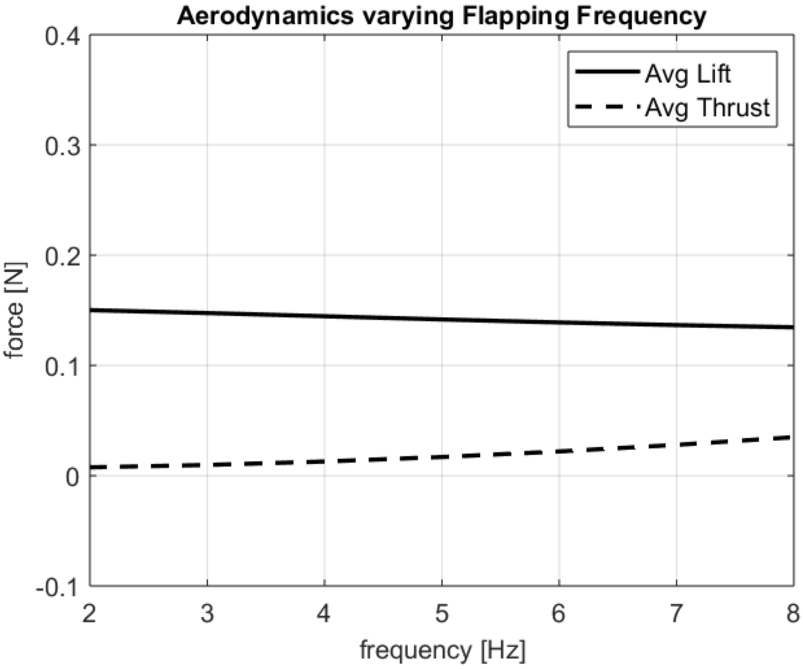

Figure 3.20: Aerodynamic lift and thrust forces as a function of flapping frequency.

Incidence Angle. The incidence angle at the shoulder joint was varied between 0 and 45 degrees, as shown in Figure 3.21. Both lift and thrust increase with the incidence angle up to approximately 25–30 degrees, beyond which aerodynamic stall leads to a reduction in force generation. For this prototype, an incidence angle of 25 degrees was selected to achieve the best balance between lift and thrust while avoiding structural overstress on the SMA wires.

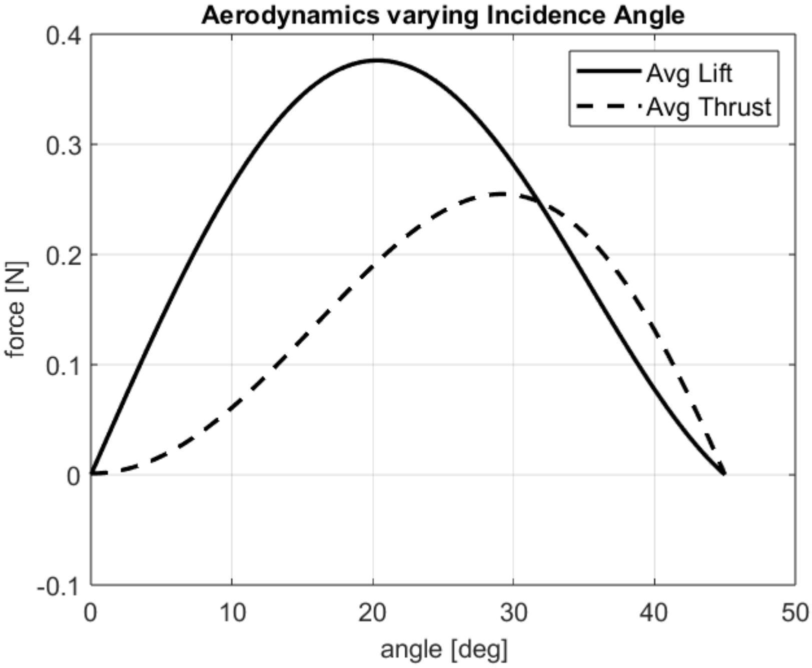

Figure 3.21: Aerodynamic lift and thrust forces as a function of incidence angle.

Relative Airspeed. The relative airspeed was varied from 1 m/s to 6 m/s, representing typical flight velocities of the ornithopter. As shown in Figure 3.22, both lift and thrust increase with higher airspeed, consistent with aerodynamic principles. However, excessive speeds impose greater structural loads, requiring the wing membrane to remain lightweight yet robust. For practical purposes, airspeeds around 5 m/s were considered optimal for this prototype.

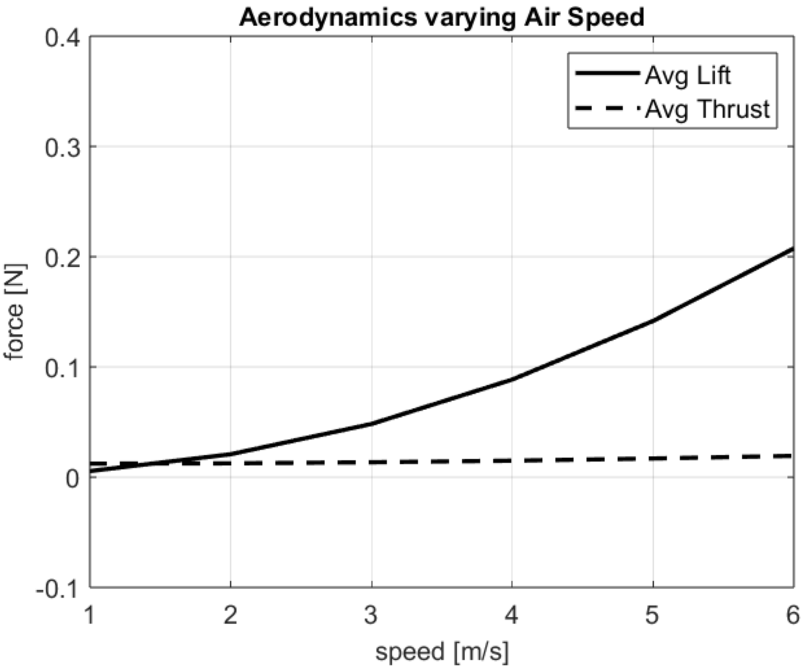

Figure 3.22: Aerodynamic lift and thrust forces as a function of airspeed.

Chapter 4

Embedded Prototype

The successful design and modeling of the SMA-driven flapping wing, as described in the previous chapter, form the basis for developing a fully functional embedded prototype. This chapter presents the practical realization of the ornithopter, focusing on the integration of on-board electronics, control software, and the physical construction of the prototype.
The embedded prototype must address the following key objectives:

- Efficient actuation and control of the SMA-based flapping mechanism.
- Lightweight and compact design to ensure flight feasibility.
- Robust structural integrity to sustain aerodynamic and mechanical loads.
- Seamless integration of electronics and mechanics to achieve coordinated flapping and pitching motion.

The chapter begins with a detailed description of the on-board electronics used for power management, signal processing, and SMA actuation. It then explores the control software architecture developed to execute precise flapping motion and control the ornithopter's trajectory. Finally, the manufacturing process of the prototype is outlined, emphasizing the construction of key components such as SMA bundles, compliant joints, and wing membranes.

4.1 Manufacturing

The manufacturing process of the ornithopter prototype involved precise design and assembly of its key components to ensure mechanical robustness, operational efficiency, and ease of integration. The main areas of focus included the fabrication of the SMA bundles, the rigid body and wing structures, the compliant joints, and the wing membranes. This section details the specific processes and techniques adopted for each of these components, starting with the SMA bundles.

4.1.1 SMA Bundles

The manufacturing of SMA bundles for the ornithopter prototype involved a careful balance between mechanical robustness, electrical conductivity, and practical feasibility. SMA wires are thin and delicate, making their attachment both a technical and mechanical challenge. The adopted solution leveraged a resistive welding process, which proved to be highly effective for this application. The SMA wires were designed to loop around a hook mounted on the wing, at a distance from the compliant joint determined by kinematic calculations (referenced in Section 3.1). This configuration simplifies the assembly and enables quick replacement of SMA wires if needed. Additionally, the design effectively doubles the actuation force, as the ”outgoing” and ”returning” segments of the wire function as two parallel actuators pulling simultaneously. This dual-force mechanism significantly enhances the overall thrust generated by the wires.
Mechanical and electrical attachment of SMA wires presents notable difficulties due to their small diameter (50–100 μm) and the specific material properties of NiTi alloys. Traditional bonding techniques such as adhesive epoxies and soldering were found to be insufficient. High-performance epoxies, while offering excellent mechanical adhesion, are electrically insulating and therefore unsuitable. Similarly, soldering with tin, despite ensuring good electrical contact, failed to provide the required mechanical robustness. Thin SMA wires frequently detached from solder joints during actuation due to slipping under dynamic loads. Based on findings from the literature, particularly the work by Scholtes et al., resistive micro-welding was identified as the optimal technique for bonding NiTi SMA wires to stainless steel substrates. This method involves passing a high current through the wire and substrate for a short period, generating localized heat sufficient to fuse the materials. The welding process not only creates a secure mechanical bond but also maintains excellent electrical conductivity, overcoming the limitations of adhesives and soldering.

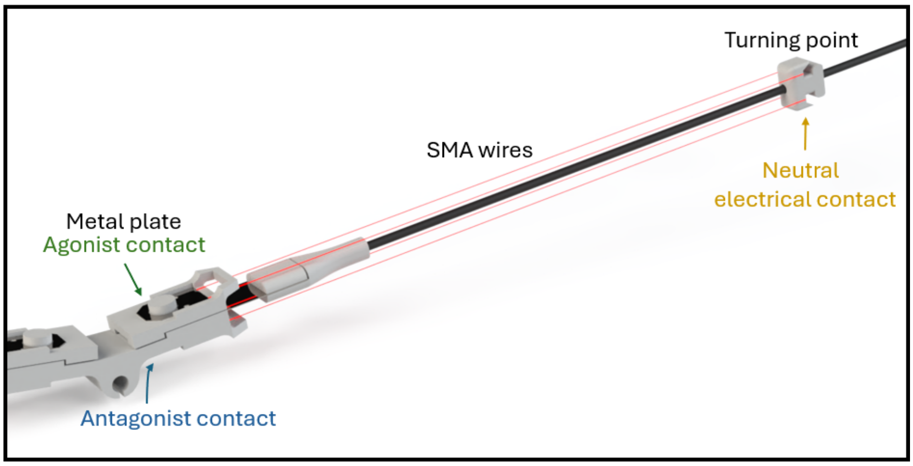

Figure 4.1: Representation of SMA bundle implemented on the ornithopter

The resistive welding process was performed using a Unitek Thin-Line weld head in combination with a MacGregor DC1000 power supply, as described in Scholtes et al. A double-pulse current waveform was employed, with amplitudes of 220 A and

240 A, pulse durations of 15 ms, and a 10 ms delay between pulses. The welding electrodes, made from CuCrZr, applied a force of 38 N during the process. The welding parameters were optimized to ensure sufficient joint strength while minimizing the heat-affected zone (HAZ), which can alter the thermo-mechanical properties of the NiTi wires. A typical weld spot exhibited a joint breaking strength of approximately 90% of the base material's maximum tensile strength.

The welded SMA bundles were integrated into the ornithopter by first attaching one end of the wire to a stainless steel mounting plate, looping the other end around the wing hook, and tensioning the wire in its martensitic phase. The second end was then welded to the same mounting plate, forming a robust and reliable actuator assembly. The plate itself was designed to facilitate mechanical attachment to the drone body and simplify electrical connections.

To minimize wiring complexity, a common electrical potential was assigned to the wing hooks for both agonist and antagonist SMA wires. This design reduced the total number of required electrical connections to five: four for the input signals to the SMA bundles and one for the common potential. The common potential was directly connected to the high-voltage output of the step-up converter, while the input signals were routed through MOSFETs controlled by the microcontroller. This configuration ensured precise and reliable activation of the SMA wires, enabling effective flapping wing actuation.

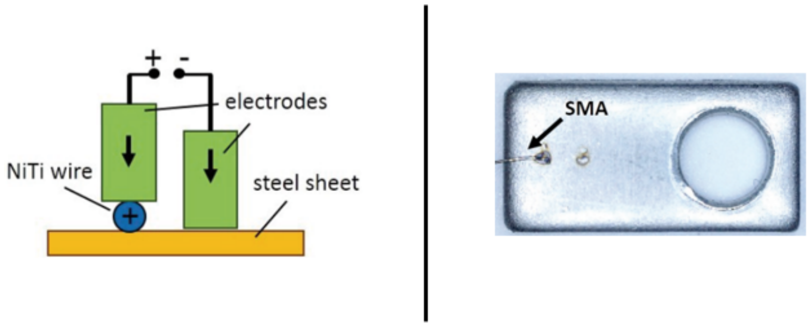

Figure 4.2: Schematic of the resistive welding machine and result photo.

The adoption of resistive welding not only enhanced the mechanical reliability of the SMA bundles but also provided a scalable solution for future designs, as the process can be automated for industrial production. This technique was particularly advantageous for the small-scale dimensions of the ornithopter, where traditional bonding methods proved inadequate.

4.1.2 Rigid-Body Parts

The fabrication of the rigid body and wing components required careful selection of both manufacturing techniques and materials to achieve a balance between mechanical robustness, weight reduction, and thermal resilience. The Selective Laser Sintering (SLS) technique was chosen for 3D printing the main body components due to its superior precision and accuracy compared to Fused Deposition Modeling

(FDM), making it more suitable for the small-scale dimensions and intricate geometries of the ornithopter prototype. As for the material, High-Temperature Resin was selected. This choice was driven by two main factors: its low density, which helps minimize the overall weight of the prototype, and its excellent thermal resistance. During operation, the SMA wires reach temperatures of approximately 90°C when activated, and although their low thermal capacity (due to a micron-scale diameter) limits the heat transfer, continuous actuation could still degrade materials with inadequate thermal resistance. High-Temperature Resin mitigates this risk while ensuring lightweight and durable components.

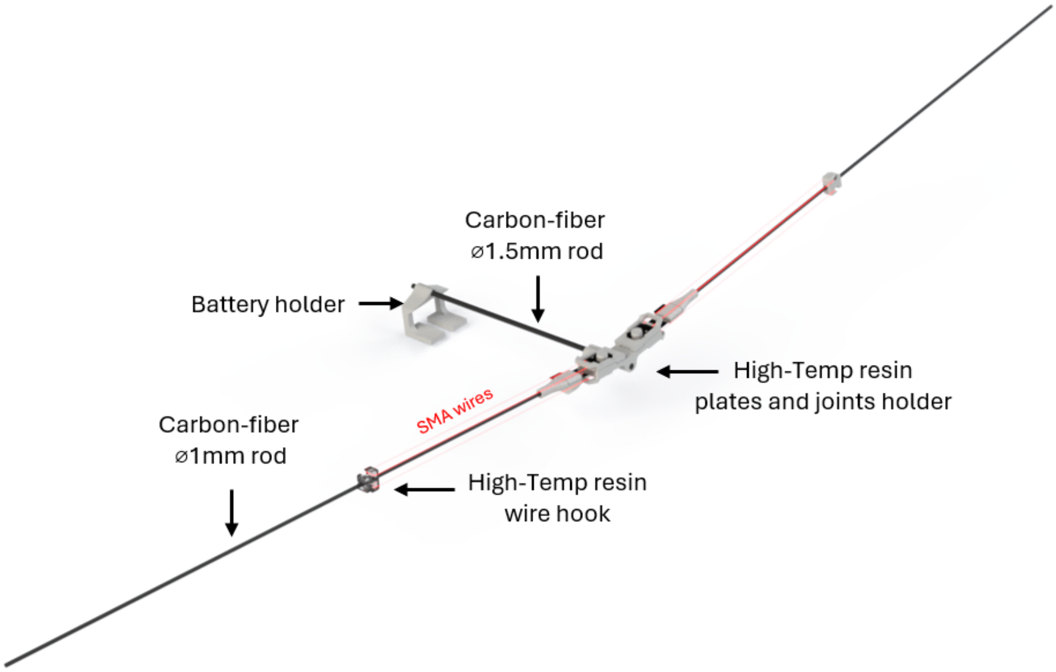

Figure 4.3: Final rigid body and wing structure combining SLS-printed resin and carbon fiber rods.

For the wing joints, a compliant joint configuration was adopted instead of traditional pinned joints. Pinned joints, while mechanically simple, introduce significant frictional losses that are exacerbated when fabricated using 3D-printed materials. The compliant joint, on the other hand, eliminates friction altogether by leveraging the flexibility of a thin stainless steel strip, laser-cut to precise dimensions, and fixed between the rigid body and the root of the wing arm. This choice aligns with the bio-inspired design philosophy of the ornithopter while enhancing mechanical efficiency. The compliant joint not only mimics the flexibility observed in biological wing structures but also improves aerodynamic performance by leveraging resonance effects, as described in Chapter 3.
To further optimize the structural framework and reduce weight, the leading edges of the wings were constructed using thin carbon fiber rods with a diameter of 1 mm. Carbon fiber was chosen for its high strength-to-weight ratio, a property that makes it widely used in aerospace applications. These rods ensure the leading edge can endure mechanical stresses during sustained flapping without adding significant mass.

A similar approach was applied to the central spine of the body, where a carbon fiber rod was used to maintain structural integrity while minimizing weight. The final structure thus consists of a hybrid design: 3D-printed resin components serve as connectors and support integration of parts, while carbon fiber rods provide the necessary stiffness and strength.

This combination of SLS-printed resin and carbon fiber components results in a lightweight, mechanically robust, and thermally resilient framework that effectively meets the operational requirements of the ornithopter prototype. The use of hybrid materials reduces overall weight while ensuring the structural elements can endure the mechanical stresses induced by the SMA-driven wing actuation. The final assembly is illustrated in Figure 4.3.

4.1.3 Wing Membrane

The manufacturing of the wing membrane was inspired by practical techniques commonly employed by hobbyists in the field of ornithopters. The wing membrane was constructed using a thin polyethylene film, a material similar to that used in lightweight plastic bags. This material was chosen for its advantageous combination of low weight, flexibility, and ease of processing, which makes it highly suitable for applications requiring both aerodynamic efficiency and minimal structural mass. Its lightweight properties ensure a negligible contribution to the total inertia of the wings, while its flexibility allows the membrane to deform naturally under aerodynamic loads, enhancing the overall performance of the wing during flapping motion.

The manufacturing process began with cutting the polyethylene film into the precise aerodynamic shape of the wing, based on the design specifications discussed in Chapter 3. This step was performed manually using a fine blade or precision scissors, ensuring accuracy while preventing any unintentional damage to the thin membrane. The simplicity of the material and cutting process facilitated rapid prototyping while maintaining the required dimensional precision.

Once shaped, the membrane was attached to the rigid components of the wing structure. Specifically, the leading edge of the membrane was bonded to the thin carbon fiber rod that forms the front edge of the wing. A lightweight and flexible adhesive was carefully applied in a thin, uniform layer to ensure both durability and minimal weight addition. This attachment is particularly critical, as the leading edge experiences the highest aerodynamic loads during flapping. The root of the membrane was similarly bonded to the central spine of the drone, creating a secure anchor point where the membrane meets the rigid body of the ornithopter. This connection ensures the effective transmission of flapping motion to the flexible membrane without compromising the structural integrity of the assembly.

The use of polyethylene film aligns well with bio-inspired principles, as it mimics the lightweight, flexible nature of biological wings found in birds and insects. In these natural flyers, the wings adapt passively to aerodynamic forces, deforming in a way that improves lift generation and minimizes energy consumption. Similarly, the polyethylene membrane exhibits a degree of passive flexibility, allowing it to respond naturally to the aerodynamic loads imposed during flapping without requiring additional actuators or control mechanisms.

From a manufacturing perspective, the choice of polyethylene film provided several advantages. It is a cost-effective material that is readily available in various thicknesses and sizes, making it ideal for prototyping applications. Additionally, its ease of processing allows it to be shaped and bonded using simple tools and adhesives, which reduces manufacturing complexity and time. The resulting membrane structure is both lightweight and durable, ensuring it can withstand the dynamic stresses associated with repeated wing flapping.

4.2 On board Electronics

The electronic system for the ornithopter was designed with simplicity, efficiency, and compactness in mind. The control signal used to actuate the SMA wires consists of a train of pulses applied alternately to the agonist and antagonist wires, producing the oscillatory wing motion. A pulsed signal with a duty cycle not exceeding 20% of the period was chosen for its simplicity and its optimization of the SMA wires' dynamic behavior. A short pulse of relatively high amplitude allows the internal temperature of the wire to rise rapidly, ensuring that the internal transformation is almost purely adiabatic. This reduces energy loss to the surrounding environment and maximizes the conversion of electrical energy into mechanical work. Furthermore, the reduced duty cycle provides the SMA wires with sufficient time to cool during the inactive portion of the cycle, enabling reliable actuation at sustained frequencies.

To generate these precise control pulses, the ESP32-C3 microcontroller mounted on a XIAO board was selected. This microcontroller offers dual-core processing, allowing the simultaneous execution of independent tasks such as signal generation and wireless communication. Additionally, its integrated Bluetooth antenna provides a convenient means for transmitting manual control signals via a paired device, enabling real-time adjustments to the ornithopter's operation. The XIAO board, with its dimensions of 21 x 17.5 mm and weight of only 3 grams, is among the smallest and lightest microcontroller boards available, making it ideal for this weight-sensitive application. Despite its compactness, the XIAO board provides sufficient computational capability to manage the control logic and communication requirements.

The SMA wires, however, require a significant power input—between 1 W and 2 W per pulse—to achieve the desired actuation. This is far beyond the power output capacity of the ESP32 microcontroller. To bridge this gap, an array of MOSFETs was introduced between the microcontroller and the SMA wires, acting as high-frequency switches. For this purpose, the ULN2003A component from Texas Instruments was chosen. The ULN2003A is a compact, integrated MOSFET array capable of handling up to 500 mA per channel, providing an efficient and lightweight solution for controlling the SMA wires. Its compact form factor minimizes the additional weight and space required, maintaining the overall compactness of the system.

The system is powered by a 3.7 V lithium-polymer (LiPo) battery, chosen for its high energy density and lightweight design. Specifically, the battery used is the Turnigy nano-tech 3.7 V 160 mAh LiPo pack, weighing only 4 grams. This battery provides a practical balance between capacity and size, ensuring sufficient energy for the SMA actuation without adding unnecessary weight. While the battery volt-

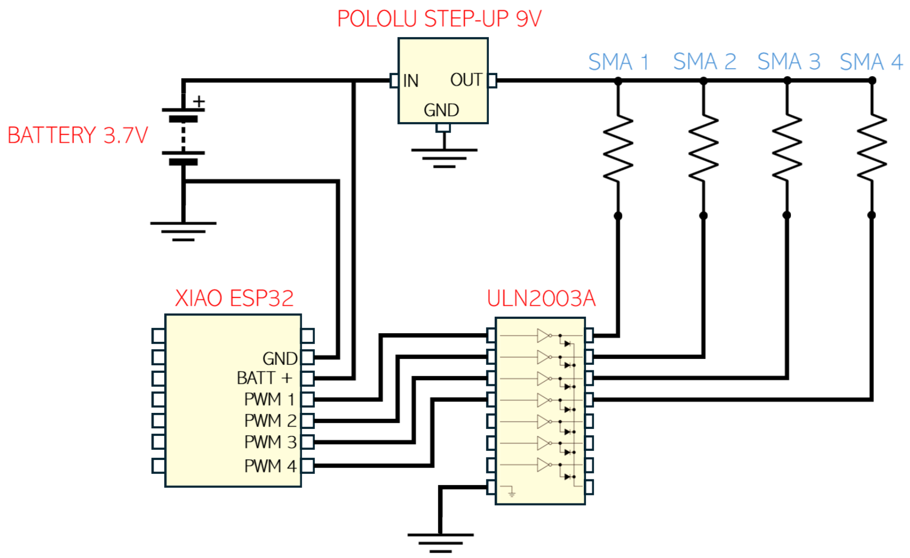

Figure 4.4: Electrical circuit schematic of the embedded system, including all components.

age is compatible with the XIAO board, the SMA wires require a higher activation voltage of approximately 9 V. To address this, a Pololu U1V10F9 step-up converter was used to efficiently boost the battery voltage to the required level. The Pololu converter offers an efficiency of up to 90% and is compact and lightweight, making it ideal for this application. With the step-up converter in place, the system can deliver the necessary voltage and current to the SMA wires without compromising the microcontroller's safety or the battery's capacity.

The required activation voltage for the SMA wires was determined using the following equations. First, the resistance R of the SMA wire is calculated as:

$$R = \rho \frac{L}{A}, \tag{4.1}$$

where L is the length of the wire, A is its cross-sectional area, and ρ is the resistivity of the SMA material. With a length of 160 mm and a diameter of 50 microns, the wire's resistance was calculated to be approximately 8 Ω. Using this resistance and a desired input power P, the activation voltage V is given by:

$$V = \sqrt{P \cdot R}. \tag{4.2}$$

For an input power of 1.5 W, the activation voltage was calculated to be approximately 9 V.

The integration of these components results in a system that efficiently manages power delivery and control logic. The XIAO microcontroller generates precise pulse signals, which are amplified by the ULN2003A MOSFET array and delivered to the SMA wires. The Pololu step-up converter ensures that the SMA wires receive the appropriate voltage, while the lightweight LiPo battery provides the necessary energy to power the entire system. This setup ensures reliable and efficient operation of the ornithopter within the stringent weight and size constraints of the prototype.

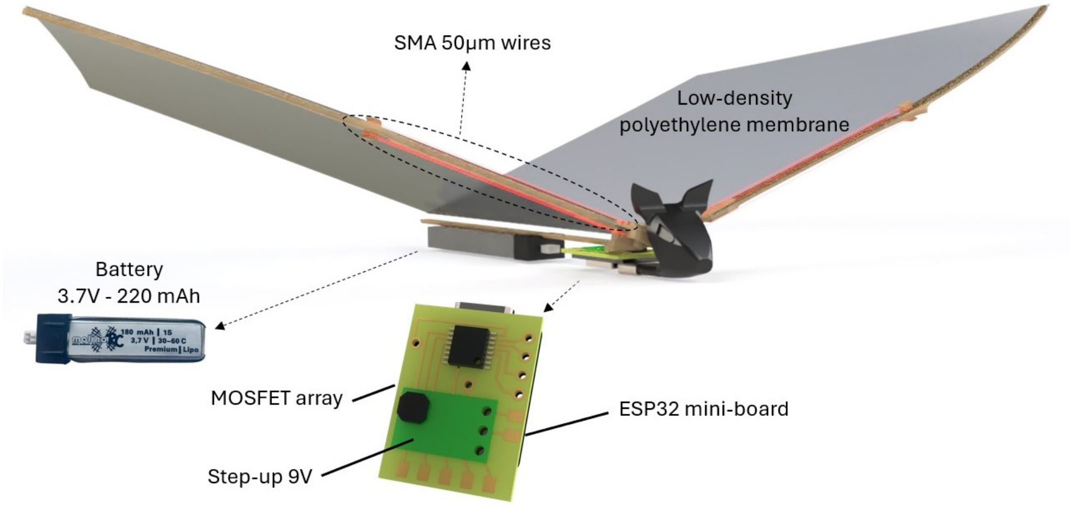

Figure 4.5: Electronic components: XIAO microcontroller, MOSFET array (ULN2003A), step-up converter (Pololu), and Turnigy nano-tech LiPo battery.

Component	Feature	Specification
XIAO (ESP32-C3)	Dimensions Weight Bluetooth Range	21 x 17.5 mm 3 grams 10 m
ULN2003A	Max Switching Voltage Switching Current Channels	50 V Up to 500 mA per channel 7
Pololu Step-Up Converter	Input Voltage Range Output Voltage Efficiency	2.5 V to 9.5 V Adjustable to 9 V Up to 90%
Turnigy LiPo Battery	Nominal Voltage Capacity Weight	3.7 V 160 mAh 4 grams

Table 4.1: Specifications of main electronic components.

4.3 Control Software

The control logic programmed into the microcontroller plays a critical role in ensuring precise and reliable operation of the ornithopter. One of the fundamental tasks of the microcontroller is to generate pulses with accurate timing to drive the flapping motion of the wings. The consistent cadence of these pulses is crucial, not only for maintaining a precise wingbeat frequency but also for fully leveraging the oscillatory resonance of the compliant joint described in previous sections.

The microcontroller activates the MOSFET switches via its GPIO (General Purpose Input/Output) pins. To ensure independent motion control for the two wings, four separate output pins are used—two for each wing, corresponding to the upstroke and downstroke directions. To guarantee the correct timing of these pulses at a specified frequency, several approaches can be utilized in embedded C programming. In this case, internal timers of the microcontroller were employed. These timers, once configured to a precise interval, generate an interrupt that triggers a specific routine associated with the timer. Specifically, two timers were set up in the control software. The first timer manages the activation of the SMA wires at a specified frequency, while the second timer deactivates the input signals according to the desired duty cycle. This dual-timer setup ensures both precise frequency control and accurate duty cycle modulation, which is essential for maintaining the thermal and mechanical performance of the SMA wires.

Beyond the basic activation and deactivation logic for the four input signals, the code incorporates Pulse Width Modulation (PWM) modulation to vary the average power delivered to the SMA wires. Although the voltage supplied to the SMA wires is fixed at 9 V by the step-up converter, PWM enables adjustment of the effective power applied to each actuator. This allows for independent mechanical behavior of the wires, as variations in input power correspond to differences in wing motion. Such control is essential for introducing asymmetry between the two wings, which can be exploited for directional control.

The PWM values, as well as commands to initiate wing flapping or manually control wing movements, are received from an external controller via Bluetooth Low Energy (BLE) communication. This external controller can be a smartphone or a PC equipped with a Bluetooth antenna. During testing and demonstrations, the ornithopter was controlled using both a MATLAB-based application on a PC and a custom Android app. The BLE communication protocol was implemented using a simple and interpretable switch-case logic to process the incoming commands from the external device.

The main control loop processes commands received via the BLE connection. When a connection is established, the system continuously monitors the ‘cmdID‘ and ‘cmdVALUE‘ characteristics to execute specific actions. These actions include starting or stopping the wing flapping, adjusting the frequency and duty cycle of the pulses, and modifying the amplitude of the SMA activation signals.

One particularly noteworthy feature of the control software is the ”manual” functionality for controlling the wings. When a specific command is issued by the user, the wings move in an opposing pair configuration (e.g., right agonist and left antagonist) to simulate the gliding turns observed in birds. Additionally, during the wing flapping motion, manual control allows the user to introduce a power differential between the two wings. By varying the power delivered to the SMA wires on the left and right sides, the resulting motion asymmetry generates a difference in aerodynamic thrust between the two wings. This differential thrust, as demonstrated in the experimental results, induces a directional change in the flight path of the drone. This combination of timer-based pulse generation, PWM modulation for power control, and BLE communication provides a versatile and efficient control framework for the ornithopter. The software design ensures that the ornithopter can operate autonomously with pre-programmed wingbeat patterns or be controlled manually via an external device, offering flexibility in operation and enhancing the overall functionality of the system.

Chapter 5

Experimental Results

5.1 Kinematics Performance

5.1.1 Test Setup: Camera Tracking

To evaluate the kinematic performance of the prototype, a high-frame-rate camera was employed to capture the flapping wing motion during operation. The setup was designed to record the angular displacement of the shoulder joint actuated by the SMA wires under varying input frequencies and power levels. This measurement is critical to assess the amplitude of movement generated by the actuators and evaluate the overall efficiency of the system.

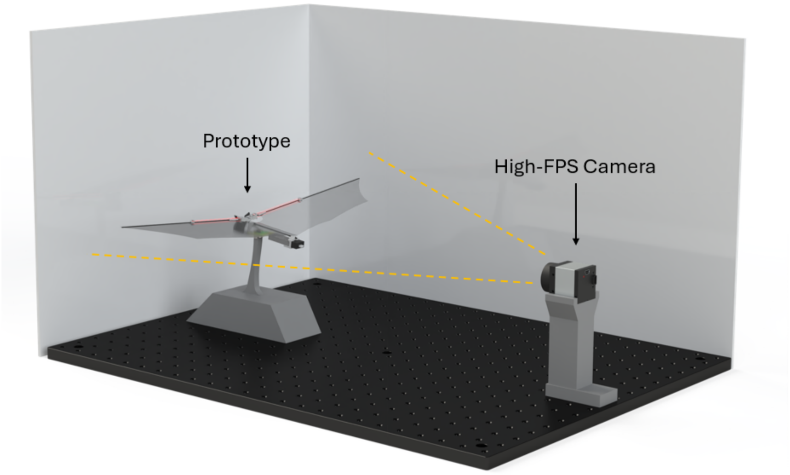

Figure 5.1: Schematic representation of the camera tracking setup.

The experimental setup included a high-speed camera capable of recording at 240 frames per second, mounted on a stable tripod directly facing the ornithopter prototype. A USB serial connection linked the camera to a computer for real-time video acquisition and analysis. A custom MATLAB script was developed to process the recorded video, track designated markers on the moving wing, and calculate the angular displacement of the shoulder joint.

During the experiment, the camera was carefully aligned with the prototype to ensure optimal visualization of the wing motion. The prototype was fixed in a controlled environment to eliminate external disturbances, allowing for accurate data collection. Once the video was recorded, the MATLAB script was executed to analyze the footage. The script used a point-tracking algorithm to identify specific points on the wing surface and calculate their positions over time. The angular displacement was derived by measuring the relative motion of the tracked points with respect to the fixed shoulder joint.

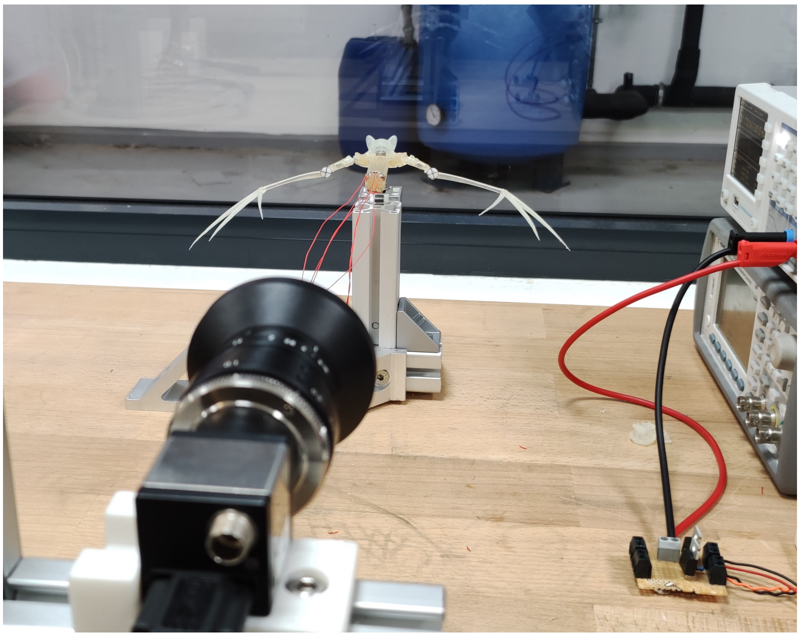

Figure 5.2: Photograph of the actual experimental setup for camera tracking.

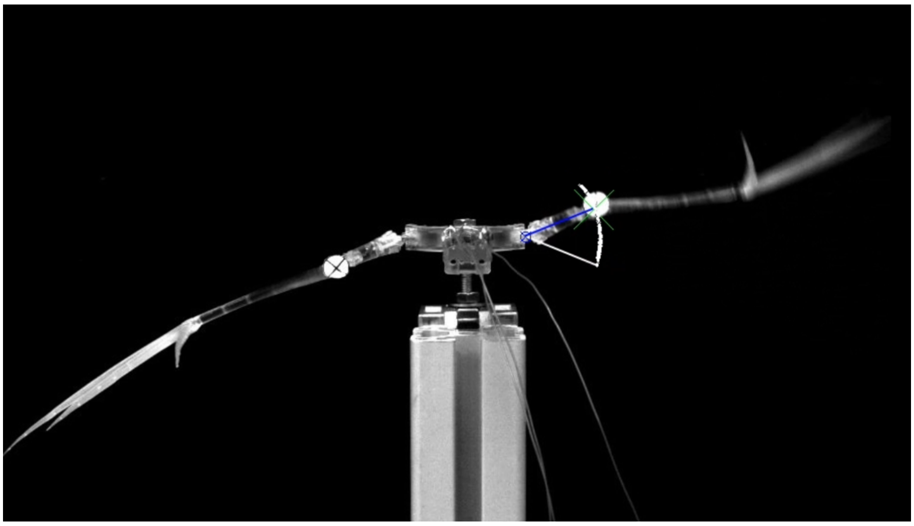

Figure 5.3: A frame of the resultant tracked video.

This setup allowed for precise measurement of the wing's angular range of motion, providing valuable insights into the kinematic performance of the SMA actuators. The data collected will be presented and discussed in the subsequent section (5.2 Flapping Movement) to evaluate the relationship between input parameters and the amplitude of wing motion.

To analyze the recorded video, a MATLAB script (presented in Appendix B) was implemented to track points on the wing surface and compute the angular displacement of the shoulder joint. The script is organized into distinct sections for selecting the video file, identifying tracking points, setting up the video analysis, and processing each frame to compute the angular displacement. The use of MATLAB's Computer Vision Toolbox ensures robust tracking and accurate computation of the kinematic data.

5.1.2 Results

Single SMA actuator

The first experimental results were produced by a prototype equipped with a simple compliant joint, characterized by low stiffness. This initial choice aimed to minimize the force required by the SMA wires to actuate the wings. The joint was constructed using a stainless-steel beam with dimensions of 0.05 mm in thickness, 3 mm in width, and 4 mm in length.

In the first test, only a single SMA wire bundle, the "upper bundle," was activated to raise the wing. The downward motion is then achieved simply thanks to gravity, acting as the antagonist force to the SMA wires. As shown in Figure 5.4, at 1 Hz of actuation frequency, the results were satisfactory, with the wing sweeping an angle of approximately 50 degrees. However, as the input frequency increased, the performance of the single SMA bundle significantly decreased, with the total swept angle reducing to just 20 degrees at 3 Hz. This performance decline was expected, as discussed in the SMA material chapter, due to the intrinsic limitations of SMA wires, such as hysteresis and temperature-dependent actuation cycles, which hinder reliable operation beyond 1 Hz without design optimizations.

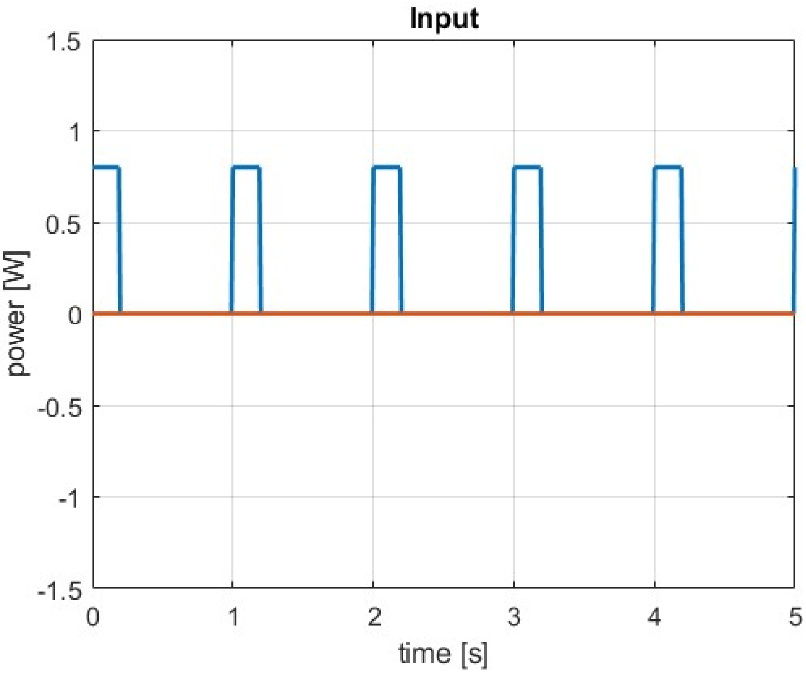

(a) Power input for the SMA bundle.

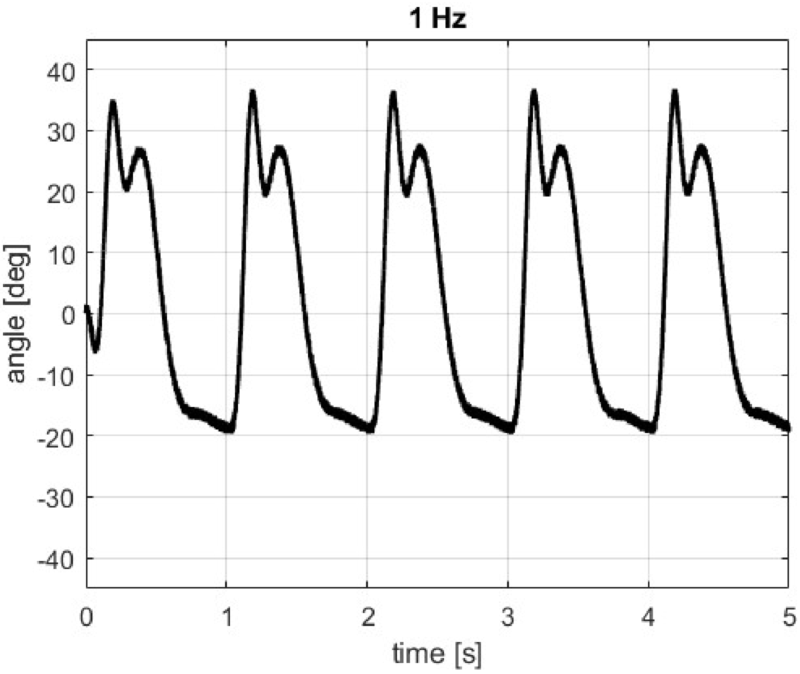

(b) Angle spanned by the wing joint

Figure 5.4: Experimental results at 1 Hz for a single SMA-bundle prototype

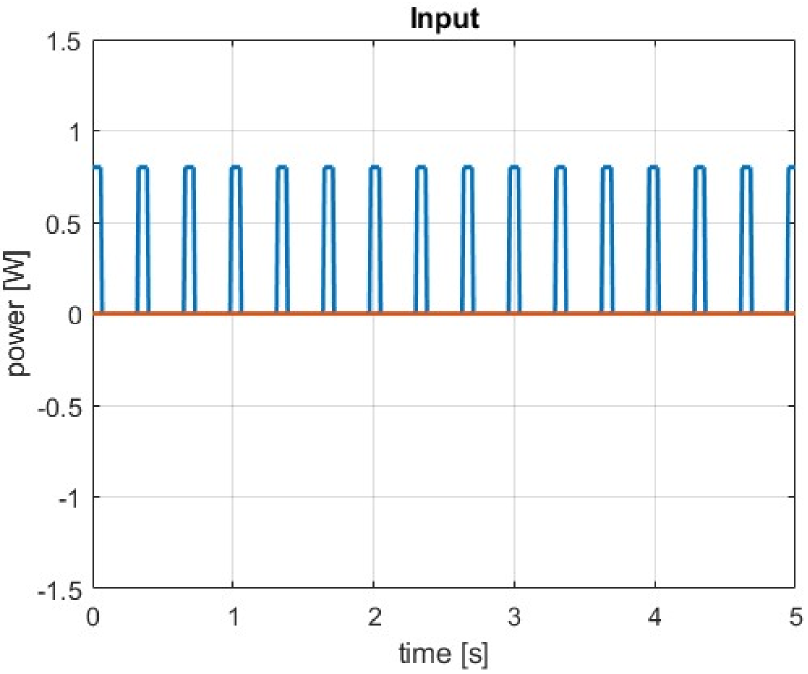

(a) Power input for the SMA bundle.

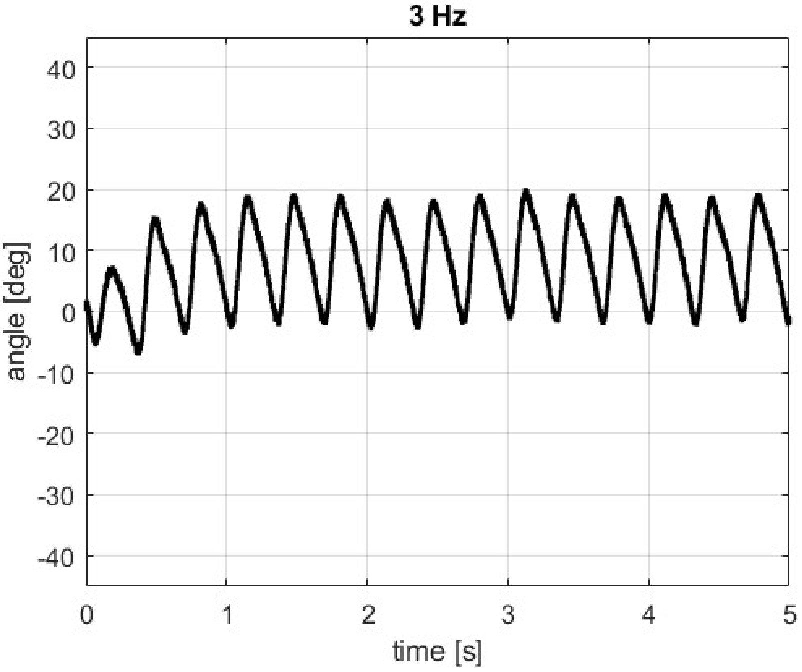

(b) Angle spanned by the wing joint

Figure 5.5: Experimental results at 3 Hz for a single SMA-bundle prototype

Agonist-Antagonist SMA actuator

To address this limitation, the first solution implemented was the agonist-antagonist configuration, as introduced in Chapter 3. In this design, both upper and lower SMA bundles were activated to alternately raise and lower the wing. The results, shown in Figure 5.6, demonstrated an improvement in the wing's swept angle to approximately 40 degrees at 3 Hz, at the expense of nearly doubling the energy consumption. However, further increasing the actuation frequency to 5 Hz led once again to a steep decline in flapping movement performance, even with an additional increase of input power to the agonist-antagonist SMAs. That is why a further design optimization was needed.

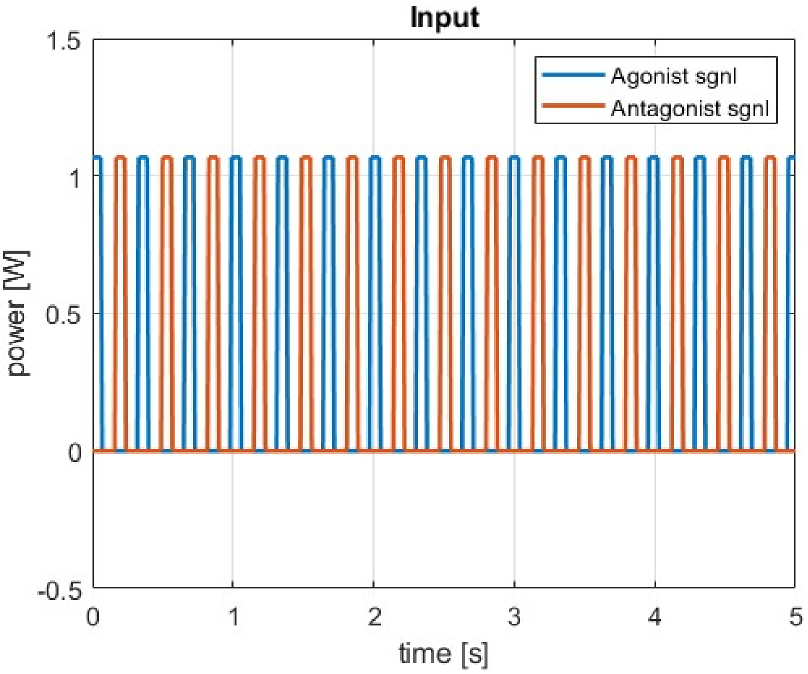

(a) Power input for the SMA bundle.

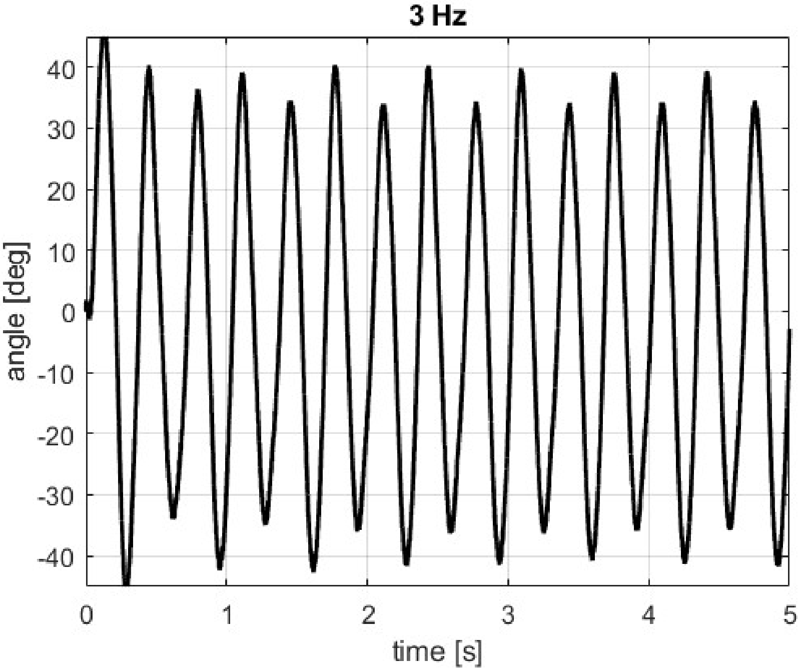

(b) Angle spanned by the wing joint

Figure 5.6: Experimental results at 3 Hz with two agonist-antagonist SMA-bundles

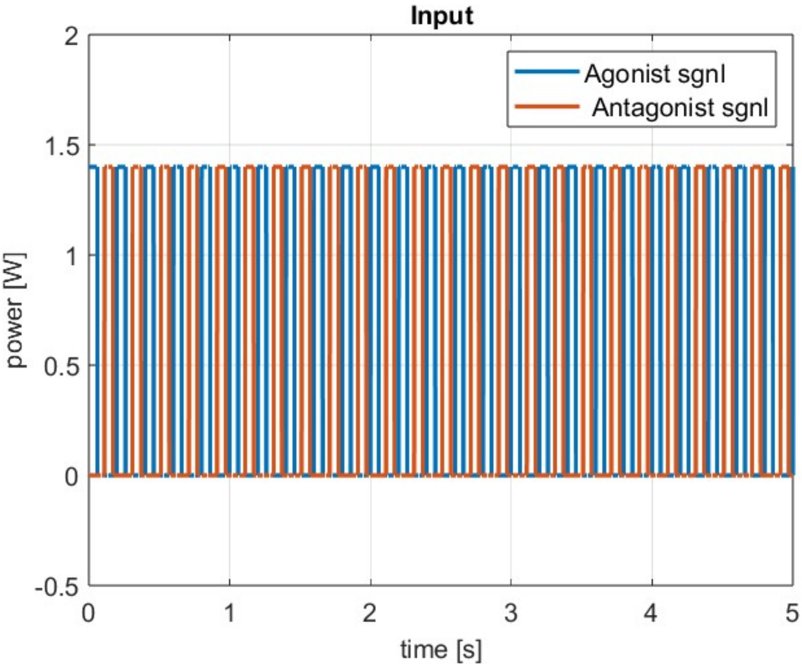

(a) Power input for the SMA bundle.

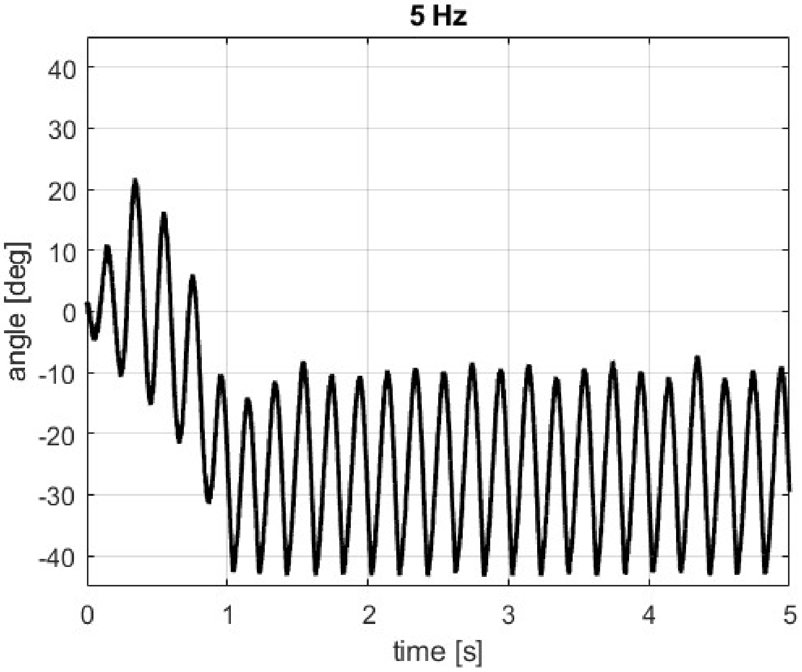

(b) Angle spanned by the wing joint

Figure 5.7: Experimental results at 5 Hz with two agonist-antagonist SMA-bundles

Agonist-Antagonist SMA actuator + Resonant Compliant Joint

Instead of increasing the number of SMA wires in each bundle—which would have drastically increased the amount of input power required and also the complexity of manufacturing—an alternative solution was implemented: leveraging the natural resonance of the compliant joint. As detailed in Chapter 3, the stainless-steel beam geometry were optimized using the provided mathematical models to achieve a natural frequency of 5 Hz, accounting for the wing's mass and inertia. The results of this experiment, shown in Figure 5.9, illustrate the effectiveness of this approach. With the same input energy as the previous test, the resonant joint design enabled the wing to sweep a total angle of approximately 60 degrees after an initial transient phase. This result highlights the importance of efficient mechanical design in achieving improved kinematic performance without increasing energy consumption. Building upon this success, further tests were conducted by increasing the stiffness of the stainless-steel beam to reach an actuation frequency of 7 Hz. This modification required only a slight increase in input power, while keeping the number and diameter of SMA wires constant. As shown in Figure **??**, the swept angle remained consistent at approximately 60 degrees, even at this higher frequency.

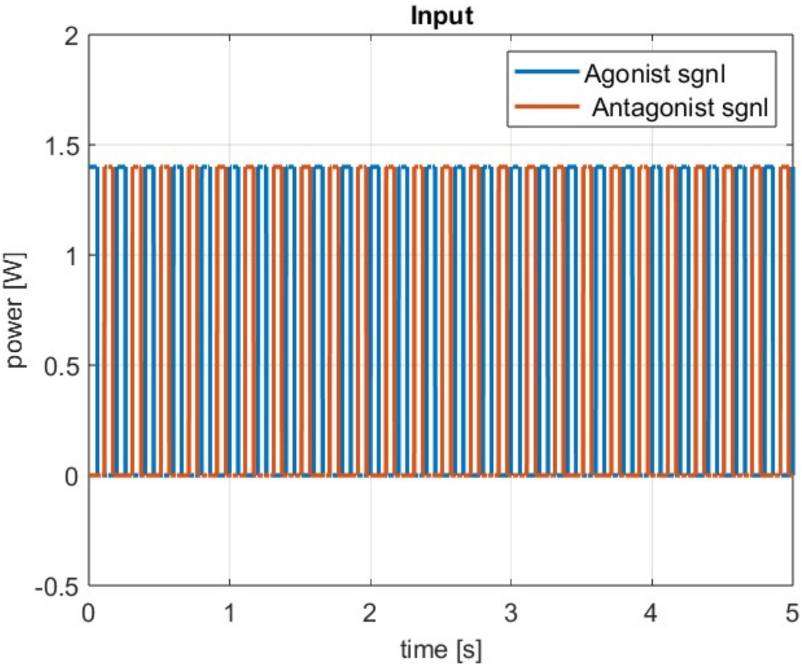

(a) Power input for the SMA bundle.

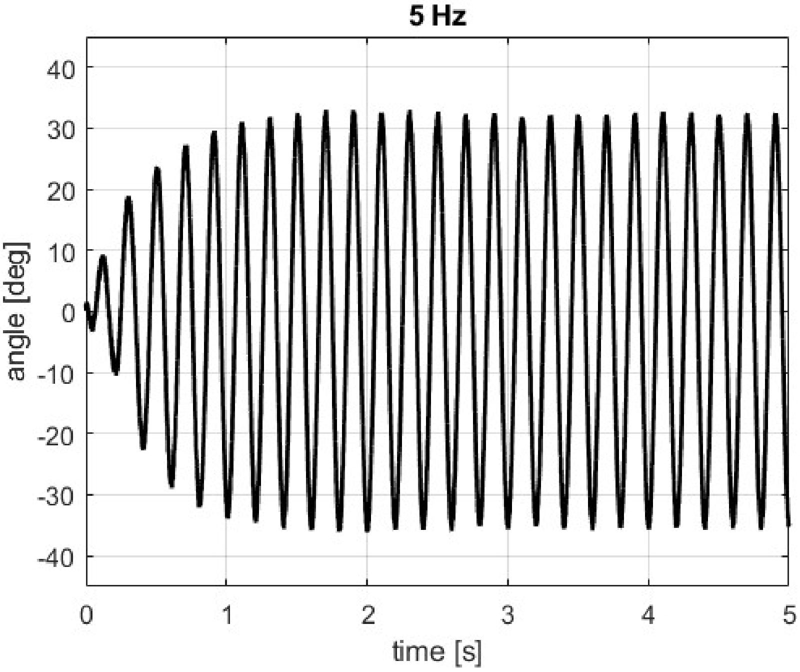

(b) Angle spanned by the wing joint

Figure 5.8: Experimental results at 5 Hz with agonist-antagonist SMA-bundles and resonant compliant joint

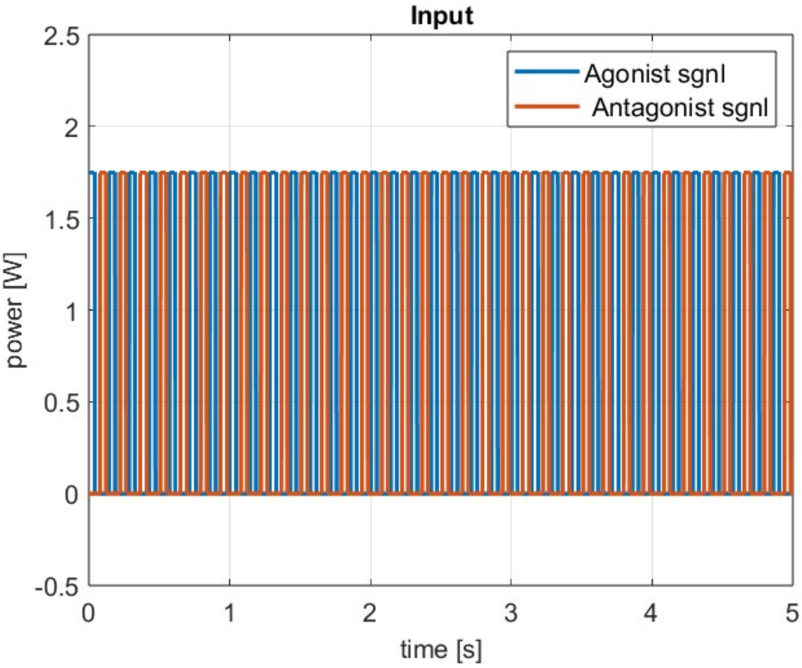

(a) Power input for the SMA bundle.

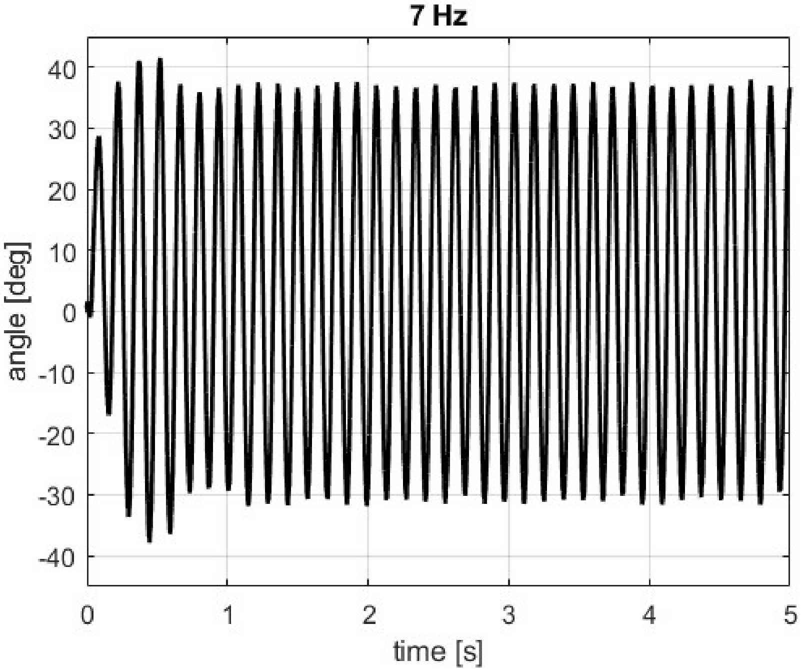

(b) Angle spanned by the wing joint

Figure 5.9: Experimental results at 7 Hz with agonist-antagonist SMA-bundles and resonant compliant joint

This kinematic achievement was satisfactory enough for the purpose of this research, especially considering the initial limitations of SMAs wire actuators. Increasing the beam stiffness beyond this point resulted in the SMA wires breaking after only a few cycles, indicating that the current bundle configuration (two wires, each 50 microns of diameter) could not withstand the increased stress, and increasing the wires diameter and/or number would have meant increase the input power. Nevertheless, 7 Hz lies within the operational frequency range of flapping-wing micro-air vehicles and their natural counterparts. That is why this frequency was deemed sufficient to proceed to the next testing phase, focused on aerodynamic performance, after mounting a thin and light membrane to the wings.

5.2 Aerodynamics Performance

5.2.1 Test Setup: Wind Tunnel Setup

The wind tunnel setup (Figure 5.10a and Figure 5.10b) was designed to experimentally measure the aerodynamic forces generated by the flapping wing mechanism of the prototype, which now features a flexible wing membrane. The primary objective was to evaluate the vertical force (lift) and horizontal force (thrust) produced by the wing motion under various operational conditions. These measurements are essential for understanding the aerodynamic performance and validating the theoretical models developed in earlier chapters.

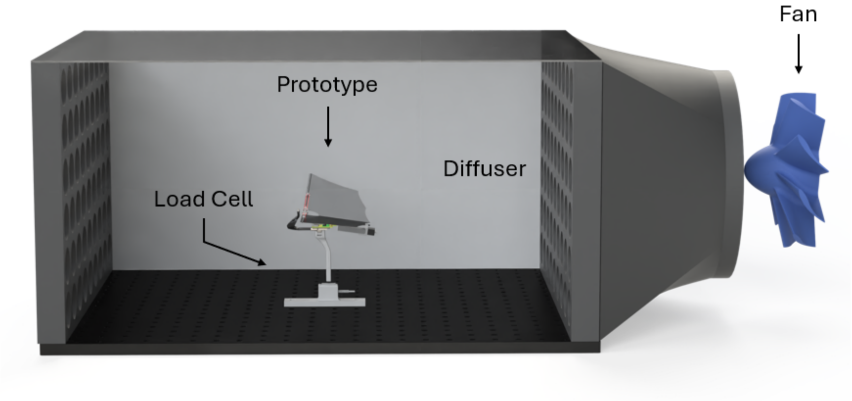

(a) Schematic representation of the wind tunnel setup.

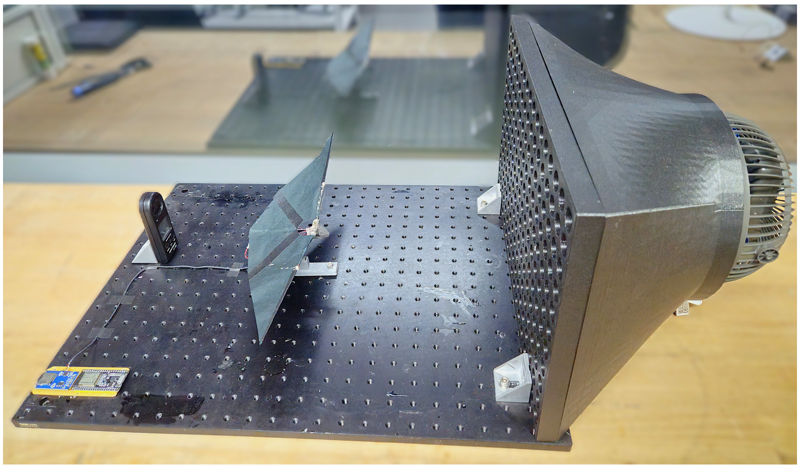

(b) Photograph of the actual wind tunnel setup.

Figure 5.10: Representation and effective photo of the wind tunnel test setup.

The prototype was actuated using a simple train of current pulses applied to the SMA wires, inducing a flapping motion of the wings. This motion generated aerodynamic forces that were measured using a Futek LSB200 load cell with a capacity of 100 grams. For lift measurement, the load cell was oriented vertically, aligned beneath the prototype's center of mass, which was precisely determined using CAD software. This configuration ensured that the vertical forces generated by the wings were captured accurately. For thrust measurement, the load cell was placed horizontally (Figure 5.11) to record the forward aerodynamic forces resulting from the flapping motion.

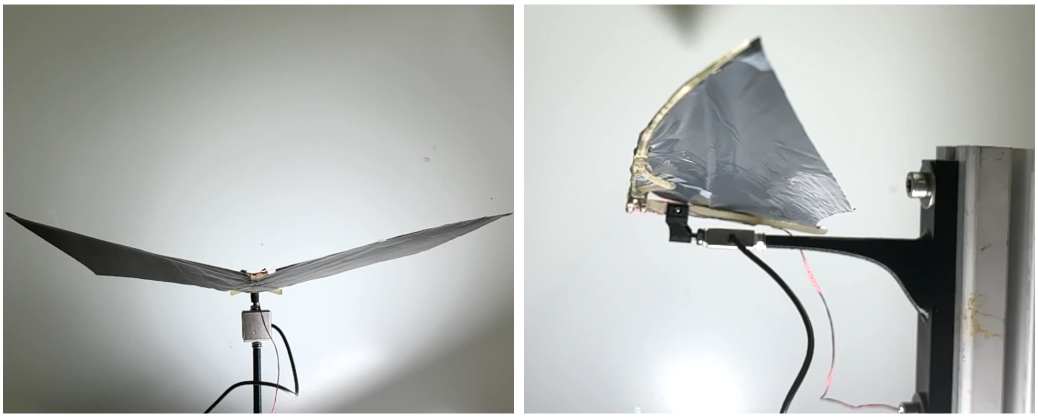

Figure 5.11: Configuration of the load cell for force measurement: (left) vertical setup for lift and (right) horizontal setup for thrust.

To simulate the relative motion of air during flight, a fan equipped with a diffuser was employed to create a uniform airflow across the prototype. The diffuser was carefully designed to minimize turbulence and ensure a steady laminar flow, thereby replicating real-world flight conditions. The airflow velocity was measured using a digital anemometer positioned close to the prototype. This setup allowed for controlled variation of the airflow speed to study its effect on the aerodynamic forces generated by the flapping wings.

The test rig was designed with stability and precision in mind. The prototype was securely mounted on a lightweight but rigid support structure to prevent unwanted vibrations or displacement during testing. The load cell was integrated seamlessly into the rig, and its orientation could be easily adjusted for lift or thrust measurements. The fan and diffuser assembly was positioned at a calibrated distance from the prototype to ensure uniform flow conditions, and the entire setup was enclosed in a testing area to prevent external environmental disturbances.

The experimental procedure involved actuating the SMA wires with specific input parameters, such as frequency and duty cycle, while recording the forces generated by the wings. The data obtained from the load cell were processed and analyzed to quantify the lift and thrust forces. These results provide critical insights into the aerodynamic efficiency of the flapping mechanism and its potential for bio-inspired aerial vehicles.

5.2.2 Results

The aerodynamic performance of the SMA-actuated ornithopter prototype was evaluated through experimental measurements of lift and thrust forces under three airflow conditions: no airflow, airflow at 2 m/s, and airflow at 5 m/s. Each aerodynamic force measurement is presented alongside the corresponding input power signal applied to the SMA bundles, highlighting the relationship between the actuation strategy and the resulting aerodynamic output.

Lift Force - No Airflow The lift force results provide critical insight into the ability of the ornithopter to generate vertical forces for potential sustained flight. In the absence of airflow (Figure 5.12), the lift force oscillates around zero, with no net average lift being produced. This behavior arises because the upstroke and downstroke motions of the wings generate nearly equal and opposite aerodynamic forces, which cancel each other out. This outcome aligns with the fundamental principle that, in the absence of forward motion or airflow, the lift generated by flapping wings cannot sustain vertical force unless additional design features, such as wing pitch variation, are introduced.

Lift Force - Airflow 2 m/s When airflow at 2 m/s is introduced, the lift behavior changes significantly (Figure 5.13). The slightly inclined attachment of the wing roots to the drone body allows the wings to generate positive lift during both the upstroke and downstroke, much like fixed-wing aircraft. This inclination causes the wing roots to interact with the oncoming airflow, producing a net positive lift force. The lift oscillates dynamically with the wing motion, but its average value increases to approximately 4 grams. This result demonstrates that even modest airflow can greatly enhance the aerodynamic performance of the prototype, simulating conditions akin to forward flight.

Lift Force - Airflow 5 m/s At a higher airflow velocity of 5 m/s (Figure 5.14), the lift force further improves, with an average value of approximately 15 grams. This value represents a critical milestone, as it is sufficient to potentially sustain the drone's weight in flight. However, achieving this required an increase in the input power to maintain a wingbeat amplitude above 40 degrees. The higher airflow increases the heat dissipation rate of the SMA wires, which theoretically could allow for faster actuation cycles. However, in practice, it necessitated slightly more input power to ensure the wires reached the transformation temperature for effective actuation. These results highlight the trade-off between aerodynamic performance and power efficiency, emphasizing the importance of optimizing the actuation strategy.

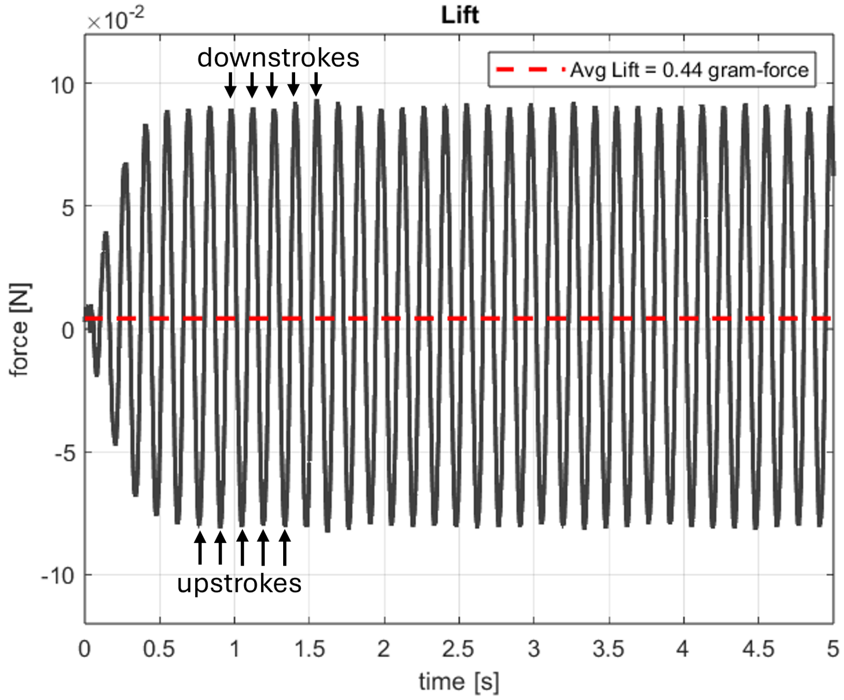

Figure 5.12: Measured lift force (no airflow).

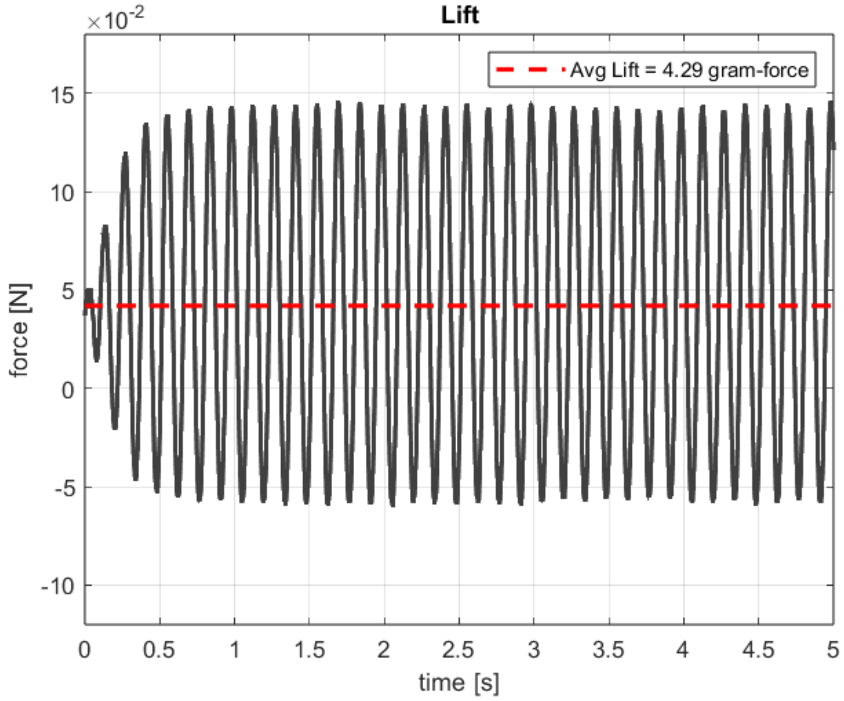

Figure 5.13: Measured lift force (airflow at 2 m/s).

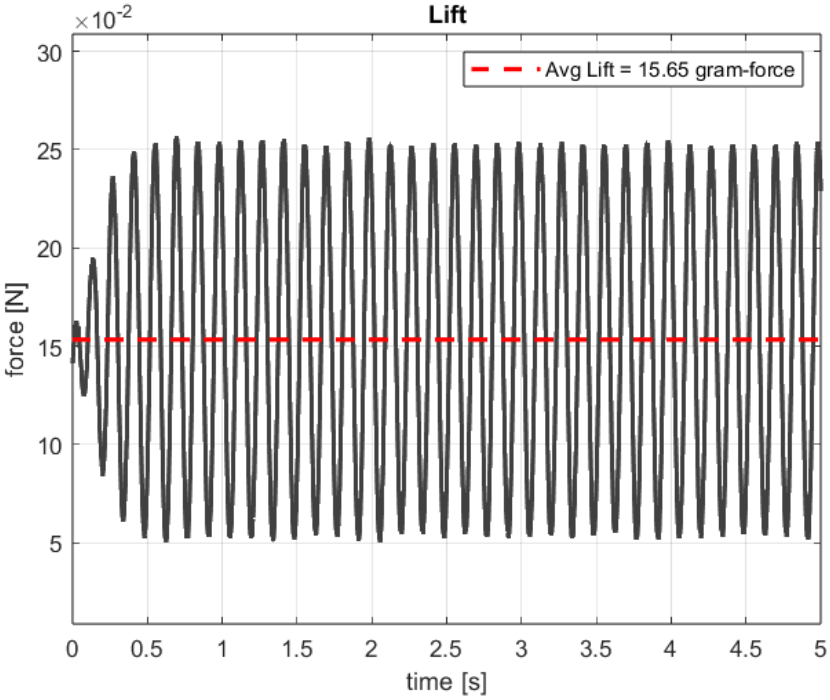

Figure 5.14: Measured lift force (airflow at 5 m/s).

Thrust Force - No Airflow The thrust force results highlight the ability of the prototype to generate forward propulsion. In the absence of airflow (Figure 5.15), the thrust force exhibits positive peaks during both the upstroke and downstroke of the wing motion. This behavior can be attributed to the aeroelastic properties of the wing membrane, as discussed in Chapter 3.3. The elastic trailing edge lags behind the rigid leading edge during each wingbeat cycle, resulting in a passive variation in the wing's pitch angle. This dynamic motion generates additional thrust during each wingbeat, producing a net positive thrust force even in the absence of airflow.

Thrust Force - Airflow 2 m/s When airflow is introduced at 2 m/s (Figure 5.16), the thrust force exhibits a decrease in the peaks generated during the upstroke, leading to a slight reduction in the average thrust.

Thrust Force - Airflow 5 m/s This reduction becomes more pronounced at 5 m/s airflow (Figure 5.17), where the thrust force profile begins to resemble the lift force, with significant peaks generated only during the downstroke. This shift occurs due to the increased aerodynamic resistance encountered during the upstroke at higher airflow velocities, which dampens the thrust contribution from the aeroelastic effects of the membrane. As with the lift experiments, the increased airflow necessitated a little increase in input power to sustain effective wingbeat amplitudes. These results underscore the importance of considering the interaction between aeroelasticity, aerodynamic forces, and input power when optimizing the propulsion performance of flapping-wing systems.

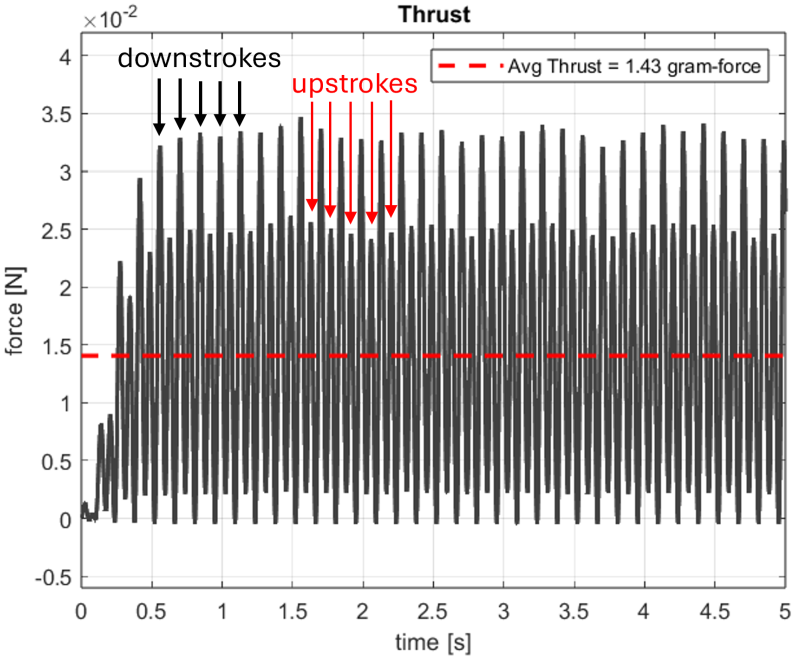

Figure 5.15: Measured thrust force (no airflow).

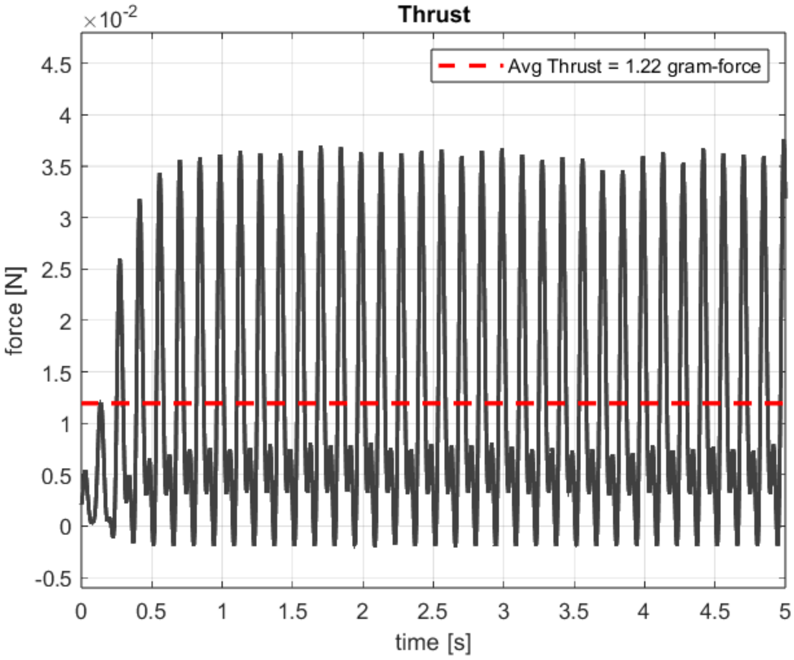

Figure 5.16: Measured thrust force (airflow at 2 m/s).

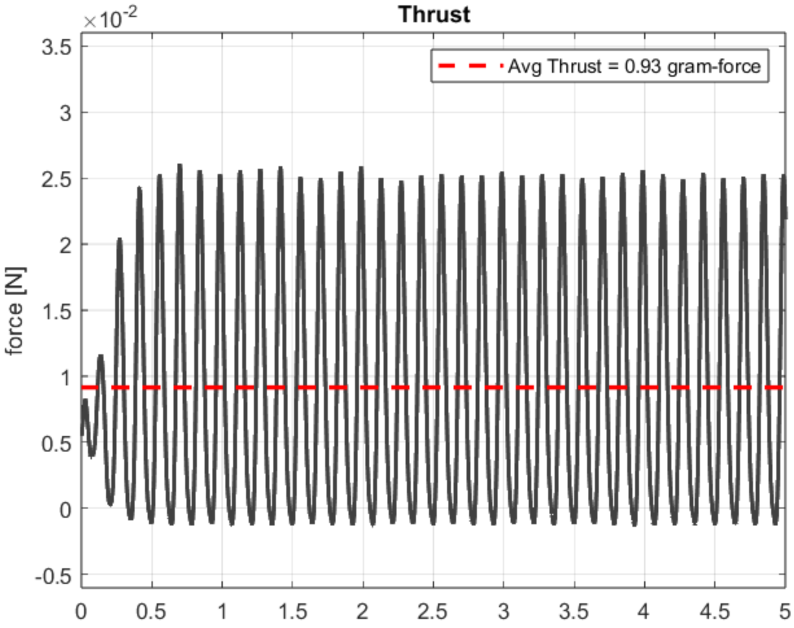

Figure 5.17: Measured thrust force (airflow at 5 m/s).

5.3 Flapping-Induced Motion

5.3.1 Test Setup: Rotating Support

To demonstrate the ability of the Shape Memory Alloy (SMA)-actuated flapping wings to generate sufficient aerodynamic thrust to propel the system, a dedicated experimental setup was developed. This setup, the final iteration of the project, was designed to allow the drone to move freely as a direct consequence of its wingbeat motion. By enabling such motion, the setup provided crucial evidence that the power delivered by the SMA actuators to the wings was capable of producing enough aerodynamic force to induce motion in the entire system.

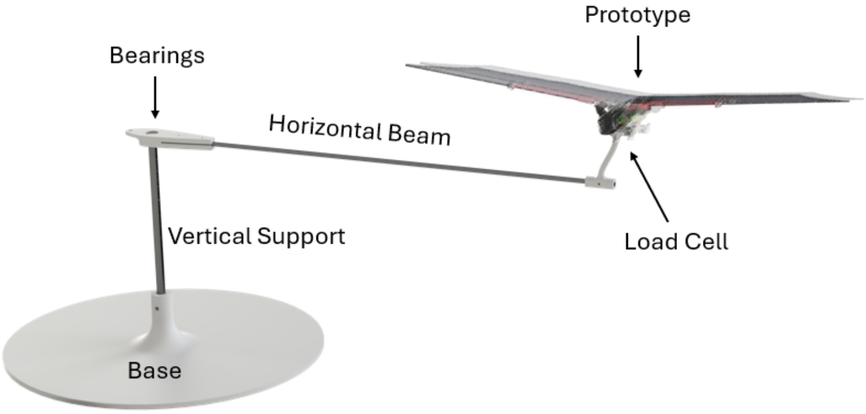

(a) Schematic representation of the rotating support setup.

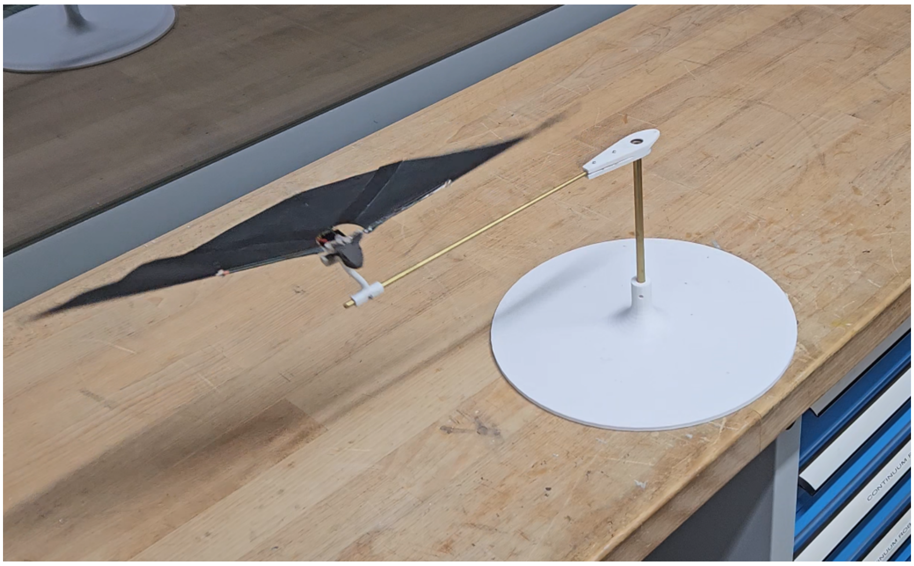

(b) Photograph of the physical rotating support setup.

Figure 5.18: Representation and effective photo of the rotating support test setup.

The setup comprised two main components designed for simplicity and functionality: a vertical support and a horizontal beam. The *vertical support* was securely fixed to the test bench, providing the necessary height to elevate the drone above the surface. This ensured the wings operated without obstruction, while the motion of the drone remained clear and measurable.

Attached to the top of the vertical support was a *horizontal beam*, which rested on a ball-bearing rotary joint at its distal end. This rotary joint enabled free rotational motion, ensuring that the drone could rotate solely due to the aerodynamic thrust produced by the flapping wings. A magnet-based mounting system was employed to securely attach the drone to the horizontal beam. This setup allowed for quick attachment and detachment, facilitating efficient testing and reconfiguration.

The rotating support was utilized both as a demonstrative platform for the project and as a means to collect aerodynamic data. Specifically, a *load cell* was integrated between the drone and the horizontal beam to measure the lift force generated during wing flapping. This configuration enabled the dynamic lift profile to be recorded, providing critical insights into the aerodynamic performance of the system.

In addition to the load cell, the drone's onboard *Inertial Measurement Unit (IMU)*, featuring an accelerometer and gyroscope, was employed to capture the instantaneous velocity of the drone during operation. These sensors, combined with the simplicity of the setup, allowed for a robust and effective experimental platform for validating the SMA-actuated flapping mechanism.

Figure 5.18a shows a schematic representation of the experimental setup, highlighting the key components, while Figure 5.18b provides an image of the physical system.

Results

The ability of the SMA-actuated ornithopter prototype to generate forward motion through flapping wings was demonstrated using the setup described in the previous subsection. Mounted at the distal end of the horizontal beam, the prototype begins to move forward as the wings flap, causing the beam to rotate due to the thrust generated by the wings. While this setup was primarily designed as a demonstration platform, it also allowed for the collection of quantitative data, thanks to the onboard Inertial Measurement Unit (IMU).

The first result is shown in Figure 5.19, which represents the horizontal velocity of the prototype, expressed in meters per second. This velocity corresponds to the tangential velocity of the outermost point of the horizontal beam, where the prototype is mounted. Starting from rest, the velocity increases during a transient phase until it stabilizes at approximately 2.8 m/s. At this steady-state velocity, the thrust generated by the wings is balanced by the aerodynamic drag acting on the drone.

As anticipated from the aerodynamic performance results, small peaks in the velocity profile are observed at a frequency twice that of the wingbeat cycle. This confirms that forward thrust is generated during both the upstroke and downstroke motions of the wings, highlighting the continuous contribution of the flapping motion to forward propulsion.

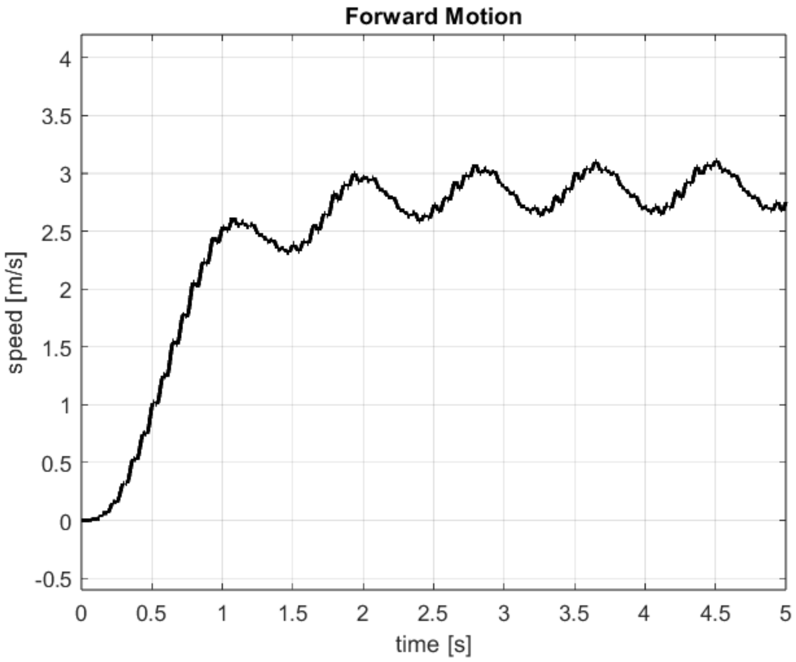

Figure 5.19: Measured horizontal velocity of the prototype during flapping-induced motion.

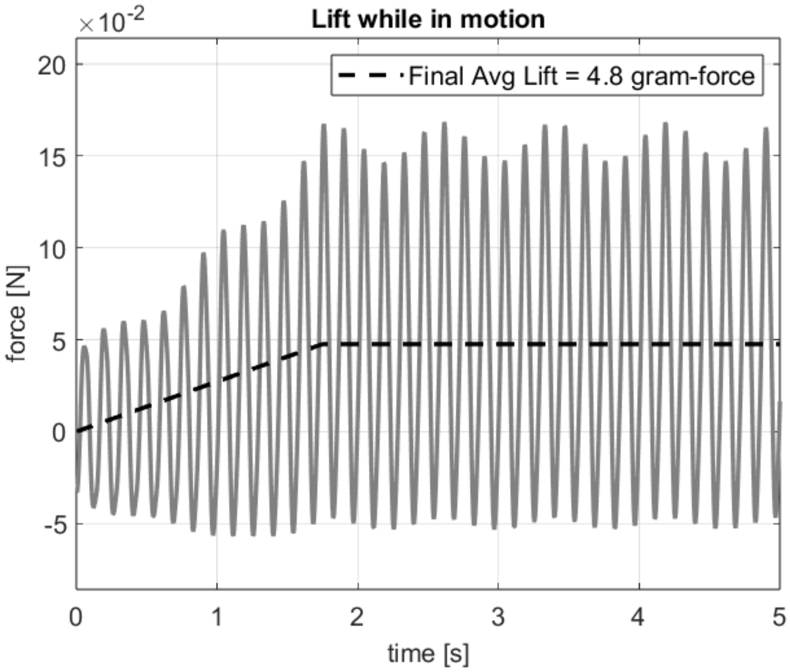

Figure 5.20: Measured lift force during flapping-induced motion of the prototype.

The second result focuses on the lift force measured during flapping-induced motion, shown in Figure 5.20. This force was recorded using the load cell positioned between the rotating support and the prototype. Initially, the lift oscillates around a zero mean value, consistent with the aerodynamic results obtained in static conditions without airflow. However, as the drone's velocity increases, the lift force exhibits a positive average value. This behavior reflects the increasing relative airflow over the wings, which enhances their ability to generate lift, much like the behavior observed in fixed-wing aircraft.

Another noteworthy capability demonstrated by the prototype is its ability to change direction when mounted parallel to the horizontal rotating beam. By varying the input power between the left and right SMA bundles, the drone can generate asymmetric thrust, resulting in directional control. For instance, applying a higher input power (in terms of peak current or duty cycle) to the SMA bundle of the right wing causes the drone to generate greater thrust on the left side, resulting in a leftward rotation of the beam. This capability highlights the potential for implementing basic directional control in future ornithopter designs.

Chapter 6

Conclusion and Outlook

This thesis has explored the development, implementation, and experimental validation of a bio-inspired Micro Air Vehicle (MAV) actuated exclusively by Shape Memory Alloy (SMA) artificial muscles. The primary objective was to investigate the feasibility of utilizing SMA-based actuation for flapping-wing flight, with an emphasis on efficiency, mechanical optimization, and aerodynamic performance.

The final prototype successfully demonstrated that, through wing flapping actuated solely by 50-micron diameter SMA wires, it is possible to generate sufficient aerodynamic thrust to move the total mass of the drone (approximately 13 grams). This accomplishment is particularly significant given the challenges associated with SMA actuation, such as low efficiency, limited response time, and material fatigue.

Thanks to the inherently high power density of SMA, the aerodynamic forces generated were over 100 times the weight of a single SMA actuator wire. To achieve this, several design and optimization techniques were implemented, combining theoretical modeling, mechanical enhancements, and resonance tuning (as detailed extensively in Chapter 3).

One of the key innovations was the integration of a compliant joint designed to match the system's flapping frequency with its resonance frequency. As evidenced by experimental results, this not only improved the amplitude-to-frequency ratio of wing motion but also significantly reduced energy consumption. By leveraging the inertial oscillation of the wing-joint system, the required SMA force was minimized, allowing successful actuation with only two SMA wires—one for each direction of motion. This approach enabled operation at frequencies typically achievable only by SMA bundles composed of multiple 25-micron diameter wires.

One of the primary concerns with SMA-based actuation has traditionally been its energy inefficiency, particularly when compared to conventional electric motors. However, the results obtained in this study suggest that, contrary to common assumptions, SMA actuation can be competitive in terms of power consumption, particularly when implemented with an optimized compliant structure. The input power signals for each actuation method, depicted in Figure 6.1a, further validate the advantage of resonance-based SMA actuation. The reduction in peak power demand contributes to a more efficient utilization of available energy, addressing one of the main drawbacks of SMA technology in aerial applications.

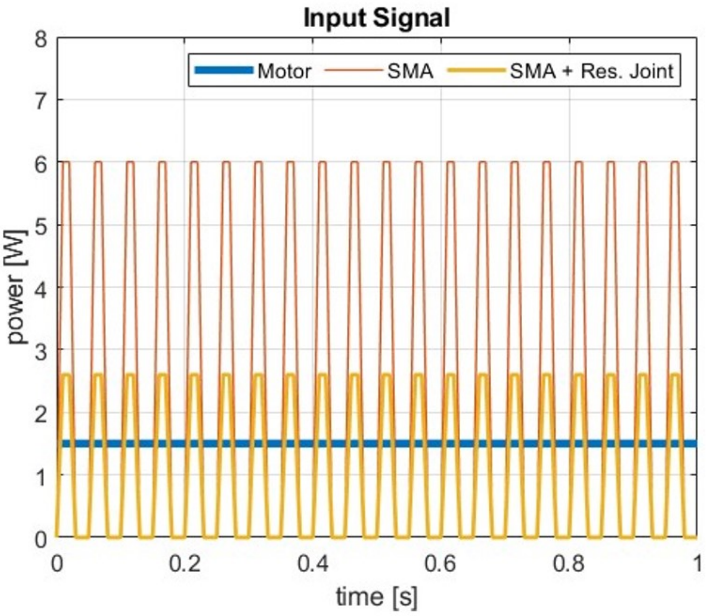

(a) Comparison of input signals.

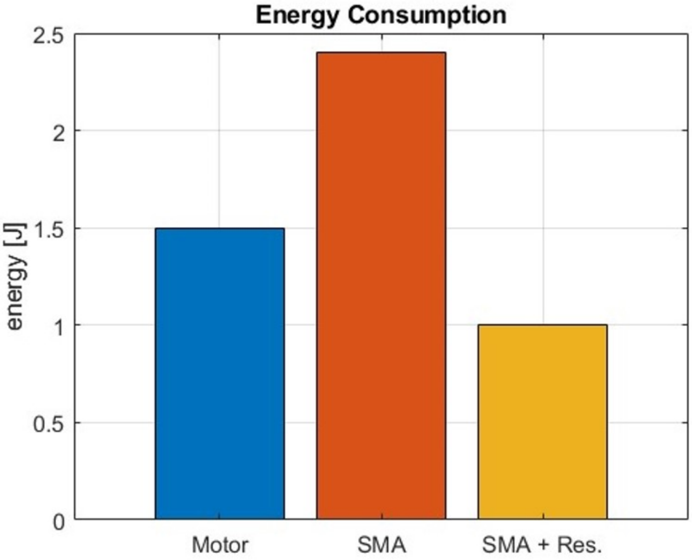

(b) Comparison of energy consumption.

Figure 6.1: Comparison of input signals and resulting energy consumption among flapping-wing drones actuated by electric motors, SMA wires, and SMA wires with resonant joint

Consequently, Figure 6.1b presents a comparison of energy consumption between different actuation strategies, including conventional electric motors, standard SMA actuation, and SMA actuation with a compliant joint. It is evident that while direct SMA actuation without resonance tuning exhibits the highest energy demand, the inclusion of a compliant joint significantly reduces energy consumption, bringing it closer to that of conventional motor-driven systems. While full autonomous flight was not achieved in this iteration of the prototype, the aerodynamic tests conducted in the wind tunnel indicate that, given a sufficient horizontal velocity, the current design is capable of sustaining flight. This suggests that, with further refinements in structural design, actuation control, and material selection, a fully SMA-actuated bio-inspired MAV with self-sustained flight is achievable. This study has demonstrated that SMA-based artificial muscles, when appropriately integrated with bio-inspired mechanical designs, can offer a viable alternative to traditional actuation methods for MAVs. The findings not only contribute to the growing field of bio-inspired robotics but also pave the way for new generations of lightweight, energy-efficient, and highly adaptive micro aerial systems. By leveraging the unique properties of SMA, future MAVs may achieve unparalleled levels of miniaturization and mechanical simplicity, making them ideal for applications in environmental monitoring, search and rescue, and even extraterrestrial exploration. With continued advancements in materials science, control methodologies, and mechanical design, the vision of a fully SMA-actuated flying micro-robot is well within reach.

Appendices

Appendix A: Control Software Code

```
#include "ArduinoBLE.h"
#include "Arduino.h"

#define pinR_up D0
#define pinR_down D1
#define pinL_up D2
#define pinL_down D3

//BLE CONNECTION VARIABLES
//--------------------------------------------------------------------
BLEService mainService("4fafc201-1fb5-459e-8fcc-c5c9c331914b");
BLEByteCharacteristic
 ↪  cmdIDcharacteristic("beb5483e-36e1-4688-b7f5-ea07361b26a8",
 ↪  BLERead | BLEWrite | BLENotify);
BLEByteCharacteristic
 ↪  cmdVALUEcharacteristic("6e1e74e1-435d-4c95-8dff-9e9651b77bfe",
 ↪  BLERead | BLEWrite);
BLEByteCharacteristic
 ↪  cmdMANUALcharacteristic("a16512fd-ce94-4245-8a6f-c97fa5c6fdeb",
 ↪  BLERead | BLEWrite);

int BTcmd_ID = 0;
int BTcmd_VALUE = 0;

//FLAPPING INPUT SIGNAL VARIABLES
//--------------------------------------------------------------------
bool isFlapping = false;
float frequency = 1;

int amplitude_R_up = 100;
int amplitude_R_down = 100;
int amplitude_L_up = 100;
int amplitude_L_down = 100;

int applied_R_up, applied_R_down, applied_L_up, applied_L_down;
```

```

int dutyCycle_up = 20;
int dutyCycle_down = 20;

int L_R_offset = 0;

//MANUAL INPUT SIGNAL VARIABLES
//--------------------------------------------------------------------
int manual_R, manual_L;
int manual_power_limit = 100;

//TIMERs VARIABLES
//--------------------------------------------------------------------
hw_timer_t *timer0 = NULL;
hw_timer_t *timer1 = NULL;
volatile bool upstroke = false;

unsigned long micros_up = round(1000 * 1000 * dutyCycle_up/ (200 *
↪  frequency));
unsigned long micros_down = round(1000 * 1000 * dutyCycle_down/ (200
↪  * frequency));

//TIMERs SETUP
//--------------------------------------------------------------------
void IRAM_ATTR onTimer0()
{
  if(isFlapping)
  {
      analogWrite(pinR_up, 0);
      analogWrite(pinR_down, 0);
      analogWrite(pinL_up, 0);
      analogWrite(pinL_down, 0);
  }
}

void IRAM_ATTR onTimer1()
{
  if(isFlapping)
  {
    if(upstroke)
    {
      timerAlarm(timer0, micros_up, true, 2);
      analogWrite(pinR_up, applied_R_up);
      analogWrite(pinL_up, applied_L_up);
      upstroke = false;
    }
```

```
    else
    {
      timerAlarm(timer0, micros_down, true, 2);
      analogWrite(pinR_down, applied_R_down);
      analogWrite(pinL_down, applied_L_down);
      upstroke = true;
    }
  }
}

//START UP SEQUENCE
//-------------------------------------------------------------------
void setup()
{
  Serial.begin(115200);
  pinMode(pinR_up, OUTPUT);
  pinMode(pinR_down, OUTPUT);
  pinMode(pinL_up, OUTPUT);
  pinMode(pinL_down, OUTPUT);

  analogWrite(pinR_up, 0);
  analogWrite(pinR_down, 0);
  analogWrite(pinL_up, 0);
  analogWrite(pinL_down, 0);
  delay(200);

  BLE.begin();
  delay(200);

  mainService.addCharacteristic(cmdIDcharacteristic);
  mainService.addCharacteristic(cmdVALUEcharacteristic);
  mainService.addCharacteristic(cmdMANUALcharacteristic);
  BLE.setLocalName("BATmav");
  BLE.addService(mainService);
  BLE.setAdvertisedService(mainService);
  BLE.advertise();
  delay(200);

  timer0 = timerBegin(1000000);
  timerAttachInterrupt(timer0, &onTimer0);
  timer1 = timerBegin(1000000);
  timerAttachInterrupt(timer1, &onTimer1);
  delay(200);

  applied_R_up = amplitude_R_up;
  applied_R_down = amplitude_R_down;
```

```
  applied_L_up = amplitude_L_up;
  applied_L_down = amplitude_L_down;

}

//EXECUTE LOOP
//---------------------------------------------------------------------
void loop()
{
  BLEDevice central = BLE.central();

  if (central)
  {
    Serial.println("CONNECTED!");
    while (central.connected())
    {
      applied_R_up = constrain(amplitude_R_up - L_R_offset, 0, 255);
      applied_R_down = constrain(amplitude_R_down - L_R_offset, 0,
       ↪  255);
      applied_L_up = constrain(amplitude_L_up + L_R_offset, 0, 255);
      applied_L_down = constrain(amplitude_L_down + L_R_offset, 0,
       ↪  255);

      if (cmdIDcharacteristic.written())
        BTcmd_ID = cmdIDcharacteristic.value();

      if (cmdVALUEcharacteristic.written())
      {
        BTcmd_VALUE = cmdVALUEcharacteristic.value();
        Serial.println("RECEIVED VALUE");
        switch (BTcmd_ID)
        {
          case 1:
            if(BTcmd_VALUE == 0)
            {
              isFlapping = false;
              analogWrite(pinR_up, 0);
              analogWrite(pinR_down, 0);
              analogWrite(pinL_up, 0);
              analogWrite(pinL_down, 0);
            }
            else
            {
              isFlapping = true;
              frequency = BTcmd_VALUE;
```

```
              micros_up = round(1000 * 1000 * dutyCycle_up / (200 * frequency));
              micros_down = round(1000 * 1000 * dutyCycle_down / (200 * frequency));
              upstroke = true;
              timerAlarm(timer1, 1000 * 1000/(2*frequency), true, 0);
            }
          break;

          case 2:
            dutyCycle_up = constrain(BTcmd_VALUE, 1, 49);
            micros_up = round(1000 * 1000 * dutyCycle_up / (200 * frequency));
            break;

          case 3:
            dutyCycle_down = constrain(BTcmd_VALUE, 1, 49);
            micros_down = round(1000 * 1000 * dutyCycle_down / (200 * frequency));
            break;

          case 4:
            amplitude_R_up = BTcmd_VALUE;
          break;

          case 5:
            amplitude_R_down = BTcmd_VALUE;
          break;

          case 6:
            amplitude_L_up = BTcmd_VALUE;
          break;

          case 7:
            amplitude_L_down = BTcmd_VALUE;
          break;

        }
      }

      if (cmdMANUALcharacteristic.written())
      {
        L_R_offset = round(2.5*(cmdMANUALcharacteristic.value() - 100));
        if(isFlapping == false)
        {
```

```
     manual_R = constrain(L_R_offset, 0, manual_power_limit);
     manual_L = constrain(-L_R_offset, 0, manual_power_limit);
     analogWrite(pinR_up, manual_L);
     analogWrite(pinR_down, manual_R);
     analogWrite(pinL_up, manual_R);
     analogWrite(pinL_down, manual_L);
    }
   }
  }

  isFlapping = false;
  analogWrite(pinR_up, 0);
  analogWrite(pinR_down, 0);
  analogWrite(pinL_up, 0);
  analogWrite(pinL_down, 0);
  Serial.println("DISCONNECTED");
 }
}
```

Appendix B: Flapping Video Tracking Code

```
%% SELECT VIDEO FILE
filename = "video_name.mp4";
start_time = 0;
duration = 5;
angle_limits = 50;

%% TRACKING PARAMETERS
minpoints_quality = 0.1;
maxbidirect_error = 100;
video_to_track = VideoReader(filename);
videoPlayer = vision.VideoPlayer('Position',[100,100,680,520]);
objectFrame =
 ↪  read(video_to_track,round(start_time*video_to_track.FrameRate));

%% SELECT TRACKING POINTS
figure; imshow(objectFrame);
origin=round(getPosition(impoint));
objectRegion=round(getPosition(imrect));
objectImage =
 ↪  insertShape(objectFrame,'Rectangle',objectRegion,'Color','red');
figure;
imshow(objectImage);

%% VIDEO SETUP
title('Red box shows object region');
points = detectMinEigenFeatures(rgb2gray(objectFrame), ...
                                 'ROI',objectRegion, ...
                                 'MinQuality', minpoints_quality);
pointImage =
 ↪  insertMarker(objectFrame,points.Location,'+','Color','white');
figure;
imshow(pointImage);
title('Detected interest points');
tracker =
 ↪  vision.PointTracker('MaxBidirectionalError',maxbidirect_error);
initialize(tracker,points.Location,objectFrame);
v = VideoWriter(cd + "\Experimental\Camera Tracking\videos_out\" +
 ↪  ...
                extractBefore(filename,".") + " - TRACK ",'MPEG-4');
open(v);
close all;

%% TRACK THE VIDEO
i=1;
```

```
while (hasFrame(video_to_track) &&
 ↪  i<duration*video_to_track.FrameRate)

      %Track the points for each frame
      frame = readFrame(video_to_track);
      [points,validity] = tracker(frame);

      %Save points and angle history
      points_buffer(i,:)= [mean(points(:,1)) mean(points(:,2))];
      angle_buffer(i,:) = ComputeAngle([origin(1)+400
       ↪  origin(2)],origin,points_buffer(i,:));
      dist_buffer(i,:) = ComputeDist(origin,points_buffer(i,:));

      %Print on screen
      framebw = rgb2gray(frame);
      out = insertMarker(framebw,points_buffer(i,:),'x','color',...
                                          'green','size',20);
      out =
       ↪  insertMarker(out,points_buffer,'o','color','white','size',1);
      out = insertShape(out,'line',[origin points_buffer(1,:); origin
       ↪  points_buffer(i,:)], ...
                        'LineWidth',2,'Color', {'white','blue'});
      out = insertMarker(out,origin,'x','color','blue','size',5);
      out = insertMarker(out,origin,'o','color','blue','size',5);
      out = insertShape(out,'line',[origin
       ↪  points_buffer(i,:)],'LineWidth',2,'Color', 'white');

      %Save video file
      writeVideo(v,out);

      i=i+1;

end
close(v);
release(videoPlayer);
```

Publications

[*] Kirsch, Susanne-Marie and Welsch, Felix and Bevilacqua, Domenico and Naso, David and Seelecke, Stefan and Rizzello, Gianluca and Motzki, Paul. **"SMA Antagonistic-Micro-Wire Bundle: First Measurement Results"** in *ASME 2020 Conference on Smart Materials, Adaptive Structures and Intelligent Systems*, 2020. DOI:10.1115/SMASIS2020-2261

[*] Bevilacqua, Domenico and Soleti, Giovanni and Naso, David and Rizzello, Gianluca and Motzki, Paul. **"Bio-Inspired Flapping Wing Antagonist Actuation with SMA Wires"** in *Actuator 2022*, 2022.

[*] Bevilacqua, Domenico and Gorges, Tom and Nalbach, Sophie and Seelecke, Stefan and Rizzello, Gianluca and Motzki, Paul. **"Performance analysis of agonist-antagonist SMA micro-wires and resonant compliant joint in bio-inspired bat-like flapping wings"** in *Electroactive Polymer Actuators and Devices (EAPAD) XXVI*, 2024. DOI:10.1117/12.3010473.

[*] Bevilacqua, Domenico and Rizzello, Gianluca and Seelecke, Stefan and Gorges, Tom and Nalbach, Sophie and Motzki, Paul. **"Aerodynamics Experimental Results of a Bio-Inspired Flapping Wing With SMA Micro-Wire Muscles and Resonant Compliant Joints"** in *ASME 2024 Conference on Smart Materials, Adaptive Structures and Intelligent Systems.*,2024 DOI:10.1115/SMASIS2024-140296.

Bibliography

[1] *BionicFlyingFox — Festo USA*. URL: `https://www.festo.com/us/en/e/about-festo/research-and-development/bionic-learning-network/highlights-from-2015-to-2017/bionicflyingfox-id%5C_32755/?utm%5C_source=chatgpt.com`.

[2] Diana D. Chin and David Lentink. "Flapping Wing Aerodynamics: From Insects to Vertebrates". In: *Journal of Experimental Biology* 219.7 (Apr. 2016), pp. 920–932. ISSN: 0022-0949. DOI: `10.1242/jeb.042317`.

[3] *Comprehensive Guide to Shape Memory Alloys - MFG Shop*. Dec. 29, 2024. URL: `https://shop.machinemfg.com/comprehensive-guide-to-shape-memory-alloys/`.

[4] Jennifer DeLaOsa. *The DelFly Nimble: An Agile Robot with Flapping Insect-Like Wings*. Sept. 2018. URL: `https://www.eeworldonline.com/the-delfly-nimble-an-agile-robot-with-flapping-insect-like-wings/`.

[5] *DelFly Nimble MAV Is the Closest Thing yet to a Robot Fruit Fly*. Sept. 2018. URL: `https://www.newatlas.com/delfly-nimble-robot-fly-mav/56339/`.

[6] Haoyuan Du et al. "A Review of Shape Memory Alloy Artificial Muscles in Bionic Applications". In: *Smart Materials and Structures* 32.10 (Aug. 2023), p. 103001. ISSN: 0964-1726. DOI: `10.1088/1361-665X/acf1e8`.

[7] *Flapping Flight*. URL: `https://s2.smu.edu/propulsion/Pages/flapping.htm`.

[8] Haitish Gandhi. "Applications of Bio-Inspired UAVs for Enhanced Aerial Capabilities". In: *2024 Regional Student Conferences*. AIAA Regional Student Conferences. American Institute of Aeronautics and Astronautics, Jan. 2024. DOI: `10.2514/6.2024-85665`. URL: `https://arc.aiaa.org/doi/10.2514/6.2024-85665` (visited on 02/23/2025).

[9] Yannik Goergen et al. "Modular Design of an SMA Driven Continuum Robot". In: *ASME 2020 Conference on Smart Materials, Adaptive Structures and Intelligent Systems*. American Society of Mechanical Engineers Digital Collection, Nov. 2020. DOI: `10.1115/SMASIS2020-2213`.

[10] A. E. Gomez-Tamm et al. "SMA Actuated Low-Weight Bio-Inspired Claws for Grasping and Perching Using Flapping Wing Aerial Systems". In: *2020 IEEE/RSJ International Conference on Intelligent Robots and Systems (IROS)*. 2020 IEEE/RSJ International Conference on Intelligent Robots and Systems

(IROS). Oct. 2020, pp. 8807–8814. DOI: `10.1109/IROS45743.2020.9341741`. URL: `https://ieeexplore.ieee.org/document/9341741`.

[11] *How Ornithopters Fly - The Principle of Flight.* URL: `http://www.ornithopter.de/principle.htm`.

[12] Zachary John Jackowski. "Design and Construction of an Autonomous Ornithopter". Thesis. Massachusetts Institute of Technology, 2009.

[13] Bing Ji et al. "Aerodynamic Analysis of a Flapping Wing Aircraft for Short Landing". In: *Applied Sciences* 10.10 (Jan. 2020), p. 3404. ISSN: 2076-3417. DOI: `10.3390/app10103404`.

[14] Xinyu Lang et al. "Effect of Wing Membrane Material on the Aerodynamic Performance of Flexible Flapping Wing". In: *Applied Sciences* 12.9 (Jan. 2022), p. 4501. ISSN: 2076-3417. DOI: `10.3390/app12094501`.

[15] M. Mandolino et al. "A Physics-Based Hybrid Dynamical Model of Hysteresis in Polycrystalline Shape Memory Alloy Wire Transducers". In: *IEEE/ASME Transactions on Mechatronics* 28.5 (Oct. 2023), pp. 2529–2540. ISSN: 1083-4435, 1941-014X. DOI: `10.1109/TMECH.2023.3253250`. arXiv: `2305.13928 [eess]`. URL: `http://arxiv.org/abs/2305.13928`.

[16] Jordi Ortín and Lucas Delaey. "Hysteresis in Shape-Memory Alloys". In: *International Journal of Non-Linear Mechanics* 37.8 (Dec. 1, 2002), pp. 1275–1281. ISSN: 0020-7462. DOI: `10.1016/S0020-7462(02)00027-6`. URL: `https://www.sciencedirect.com/science/article/pii/S0020746202000276`.

[17] Umberto Pesavento and Z. Jane Wang. "Flapping Wing Flight Can Save Aerodynamic Power Compared to Steady Flight". In: *Physical Review Letters* 103.11 (Sept. 2009), p. 118102. DOI: `10.1103/PhysRevLett.103.118102`.

[18] Luca Petricca, Per Ohlckers, and Christopher Grinde. "Micro- and Nano-Air Vehicles: State of the Art". In: *International Journal of Aerospace Engineering* 2011.1 (2011), p. 214549. ISSN: 1687-5974. DOI: `10.1155/2011/214549`.

[19] Alireza Ramezani, Soon-Jo Chung, and Seth Hutchinson. "A Biomimetic Robotic Platform to Study Flight Specializations of Bats". In: *Science Robotics* 2.3 (Feb. 2017), eaal2505. DOI: `10.1126/scirobotics.aal2505`.

[20] Gottfried Sachs. "Comparison of Power Requirements: Flapping vs. Fixed Wing Vehicles". In: *Aerospace* 3.4 (Dec. 2016), p. 31. ISSN: 2226-4310. DOI: `10.3390/aerospace3040031`.

[21] Stefan Seelecke and Ingo Mu¨ller. "Shape Memory Alloy Actuators in Smart Structures: Modeling and Simulation". In: *Applied Mechanics Reviews* 57.1 (Feb. 10, 2004), pp. 23–46. ISSN: 0003-6900. DOI: `10.1115/1.1584064`. URL: `https://doi.org/10.1115/1.1584064`.

[22] *Shape Memory Alloy (SMA) Actuators: The Role of Material, Form, and Scaling Effects - Kim - 2023 - Advanced Materials - Wiley Online Library.* URL: `https://advanced.onlinelibrary.wiley.com/doi/10.1002/adma.202208517?utm_source=chatgpt.com`.

[23] *Shape Memory Alloy (SMA)-Enabled Actuators — T2 Portal.* URL: `https://technology.nasa.gov/patent/LEW-TOPS-153?utm_source=chatgpt.com`.

[24] W. Shyy et al. "Recent Progress in Flapping Wing Aerodynamics and Aeroelasticity". In: *Progress in Aerospace Sciences* 46.7 (Oct. 2010), pp. 284–327. ISSN: 0376-0421. DOI: `10.1016/j.paerosci.2010.01.001`.

[25] Wei Shyy et al. "Aerodynamics, Sensing and Control of Insect-Scale Flapping-Wing Flight". In: *Proceedings of the Royal Society A: Mathematical, Physical and Engineering Sciences* 472.2186 (Feb. 2016), p. 20150712. DOI: `10.1098/rspa.2015.0712`.

[26] M. Simoes et al. *Modelling Fatigue Crack Growth in Shape Memory Alloys.* Dec. 15, 2021. DOI: `10.48550/arXiv.2112.08209`. arXiv: `2112.08209 [cs]`. URL: `http://arxiv.org/abs/2112.08209`. Pre-published.

[27] F Simone, G Rizzello, and S Seelecke. "Metal Muscles and Nerves—a Self-Sensing SMA-actuated Hand Concept". In: *Smart Materials and Structures* 26.9 (Aug. 2017), p. 095007. ISSN: 0964-1726. DOI: `10.1088/1361-665X/aa7ad5`.

[28] Yashwanth Tummala et al. "Design of a Passively Morphing Ornithopter Wing Using a Novel Compliant Spine". In: ASME 2010 Conference on Smart Materials, Adaptive Structures and Intelligent Systems. American Society of Mechanical Engineers Digital Collection, Apr. 4, 2011, pp. 703–713. DOI: `10.1115/SMASIS2010-3637`. URL: `https://dx.doi.org/10.1115/SMASIS2010-3637`.

[29] Fatemeh Yazdandoost. "Mechanics of Phase Transformation in NiTi Shape Memory Alloys at The Atomistic Scale". In: (Feb. 14, 2019). URL: `http://hdl.handle.net/10919/99628`.

[30] Jianjun Zhang and Yuehong Yin. "SMA-based Bionic Integration Design of Self-Sensor–Actuator-Structure for Artificial Skeletal Muscle". In: *Sensors and Actuators A: Physical* 181 (July 2012), pp. 94–102. ISSN: 0924-4247. DOI: `10.1016/j.sna.2012.05.017`.